Contents of Appendices

Contents of Appendices

List of Figures for Appendices

Appendix A

List of Tables for Appendices

Appendices

Appendix A Mineral Chemistry of the Elements of Interest

A.1 Chemical Properties of Reference Materials of the Elements of Interest

Table A1 Chemical properties of eight As reference materials used in this work, including solubility constants (K_{sp}) at 25 ℃.

Formula	Name	Crystal system	E_0 (eV)*	Oxidation State	Coordination	K_{sp}
As	arsenic	na	11866.0	0	NA	na
As_4S_4	realgar	monoclinic [4]	11866.3	+3	T [4]	na
As_2S_3	orpiment	monoclinic [11]	11867.9	+3	TPM [11]	1.4×10^{-28} [22]
$NaAsO_2$	sodium arsenite	na	11869.7	+3	TP	na
As_2O_3	claudetite	cubic [28]	11869.8	+3	TP [28]	7.4×10^{-3} (17 g/100 ml) [16]
$Ca_3(AsO_4)_2$	calcium arsenate	monoclinic [40]	11873.7	+5	T [40]	$1.0\times10^{-5.56}$ [50]
$Zn_2AsO_4(OH)$	adamite	orthorhombic [1]	11873.7	+5	T [1]	$2.8x10^{-28.00}$ [59]
As_2O_5	arsenic (V) oxide	orthorhombic [60]	11873.8	+5	T&O [60]	8.2 (65.8 g/100 ml) [16]

*: E0 is the energy value of the first peak of the first derivative of the experimental As K-edge XAS spectra;
Ksp and molar solubility (with a unit of M or mol/L) are under air pressure and room temperature;
'TPM' represents trigonal pyramidal; 'TP' represents trigonal planar; 'T' refers to tetrahedron; 'O' stands for octahedron;
'Cal' means that the value was calculated using Ksp;
'NA': not available.

Appendix A

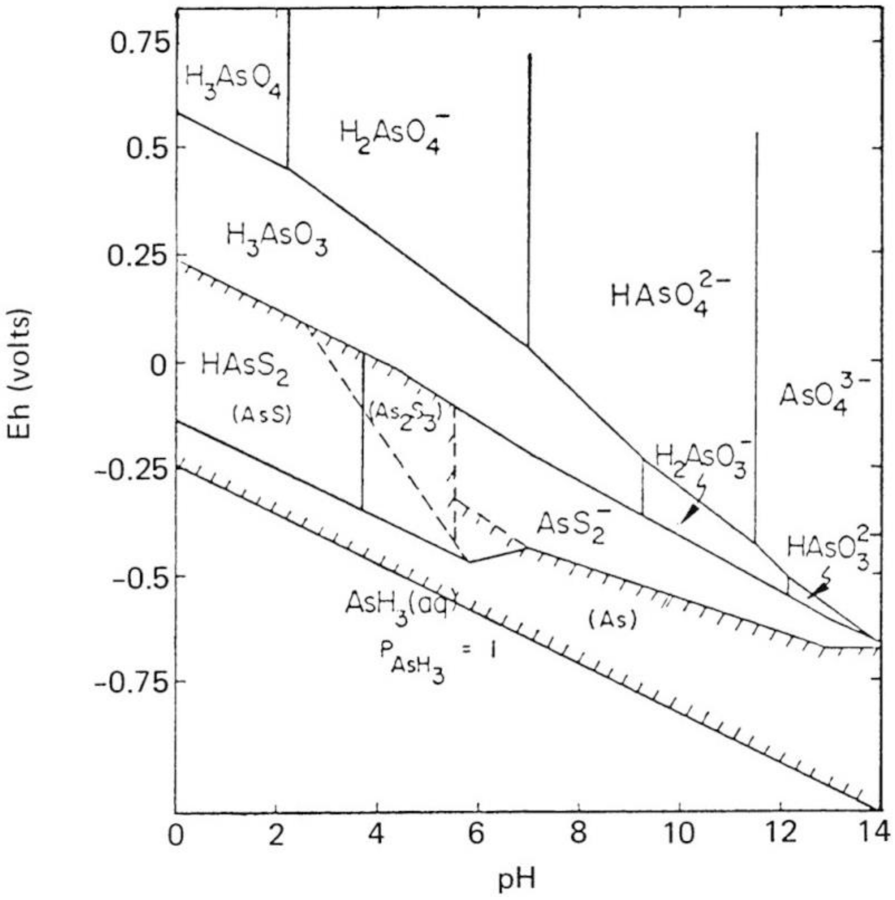

Figure A1 The Eh-pH diagram for arsenic at 25° C and 1 atm [16].

Table A4 Chemical properties of ten Cr reference materials used in this work, including solubility constants (K_{sp}) at 25 ℃.

Formula	Name	Crystal System	E_0 (eV)*	Oxidation State	Coordination type	K_{sp}
Cr	chromium	na	5989.0	0	NA	na
Cr_2S_3	chromium (III) sulfide	rhombohedral [5]	5995.8	3	O [5]	na
$Cr_2(SO_4)_3{\cdot}xH_2O$	chromium (III) sulfate hydrates	rhombohedral [12]	6002.0	3	O [12]	na
$Cr(OH)_3$	chromium (III) hydroxide	na	6002.0	3	O	6.3×10^{-31} [17]
$FeCr_2O_4$	Iron chromite	cubic [29]	6002.0	3	O [29]	na
$Cr_{0.3}Fe_{0.7}$	na	na	6003.0	3	O	na
Cr_2O_3	chromium (III) oxide	trigonal [36]	6003.4	3	O [36]	na
$Cr(NO_3)_3$	chromium (III) nitrate	na	6003.6	3	O	na
Na_2CrO_4	sodium chromate	orthorhombic [49]	6005.5	6	T [49]	$1.0 \times 10^{-3.26}$ [8]
CrO_3	chromium (VI) trioxide	orthorhombic [57]	6005.6	6	T[57]	na

*: E0 is the energy value of the first peak of the first derivative of the experimental Cr K-edge XAS spectra;
Ksp and molar solubility (with a unit of M or mol/L) are under air pressure and room temperature.
'T' refers to tetrahedron; 'O' stands for octahedron;
'Cal' means that the value was calculated using K_{sp};

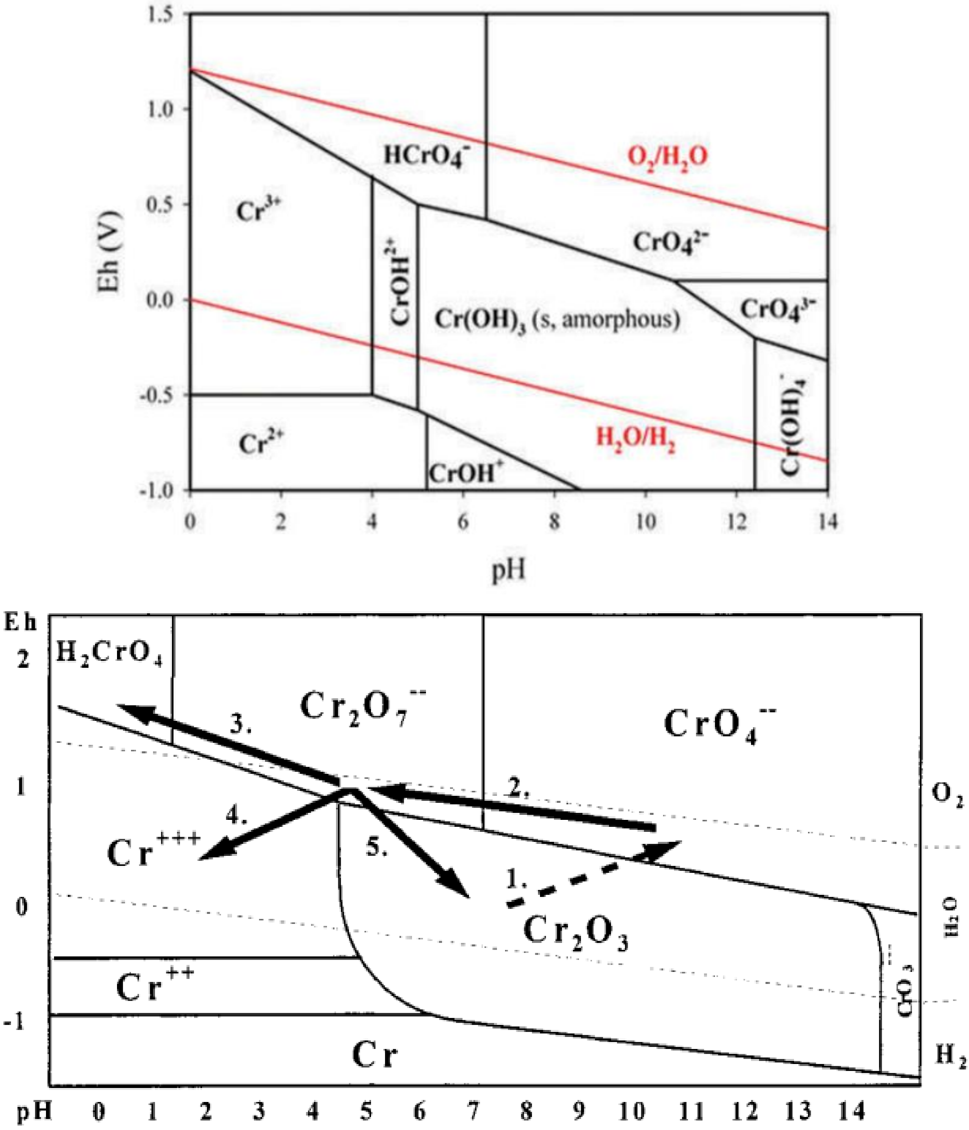

Figure A2 The Eh–pH diagram of chromium at 25° C and 1 atm [17, 18].

Table A5 Chemical properties of thirteen Cu reference materials used in this work, including solubility constants (K_{sp}) at 25 ℃**.**

Formula	Name	Crystal system	E_0 (eV)*	Oxidation State	Coordination type	K_{sp}
Cu	copper	na	8979.0	0	na	na
Cu_2S	chalcocite	monoclinic [6]	8981.1	+1	TP [6]	2.5×10^{-49} [8]
CuS	covellite	hexagonal [15]	8981.6	+1&2	TP&T (1:2) [15]	5.4×10^{-37} [8]
na	Corning glass B	na	8981.6	+1&2	na	na
$CuFeS_2$	chalcopyrite	na	8982.1	+2	na	na
CuO	tenorite	monoclinic [27]	8983.6	+2	SP4 [27]	1.6×10^{-20} [8]
CuO/SiO_2	na	na	8985.0	+2	T	na
$Cu(OH)_2$	spertiniite	orthorhombic [37]	8985.6	+2	SP5 [37]	4.6×10^{-20} [8]
$CuCO_3 \cdot Cu(OH)_2$	malachite	monoclinic [51]	8986.2	+2	SP4&O (1:1) [51]	6.9×10^{-34} [8]
$Cu_3(PO_4)_2$	copper phosphate	triclinic [58]	8986.2	+2	SP4&TB (1:1) [58]	1.4×10^{-37} [8]
$Cu_2Cl(OH)_3$	atacamite	orthorhombic [62]	8986.2	+2	SP4&O (1:1) [62]	2.3×10^{-35} [8]
$Cu_2Al_2H_2Si_2O_5(OH)_4 \cdot nH_2O$	chrysocolla	na	8986.2	+2	SP5	na
$CuSO_4 \cdot 5H_2O$	chalcanthite	triclinic [64]	8987.8	+2	O [64]	2.3×10^{-3} [8]

***:** E_0 is the energy value of the first peak of the first derivative of the experimental Cu K-edge XAS spectra;
K_{sp} and molar solubility (with a unit of M or mol/L) are under air pressure and room temperature;
'TP' represents trigonal planar (3 bonds); 'SP4' stands for 'square planar' (4 bonds); 'T' refers to tetrahedron (4 bonds); 'SP5' refers to square pyramidal (5 bonds); 'TB' refers to trigonal bipyramidal (5 bonds); 'O' stands for octahedron (6 bonds);
'Cal' means that the value was calculated using K_{sp};
'na': not available.

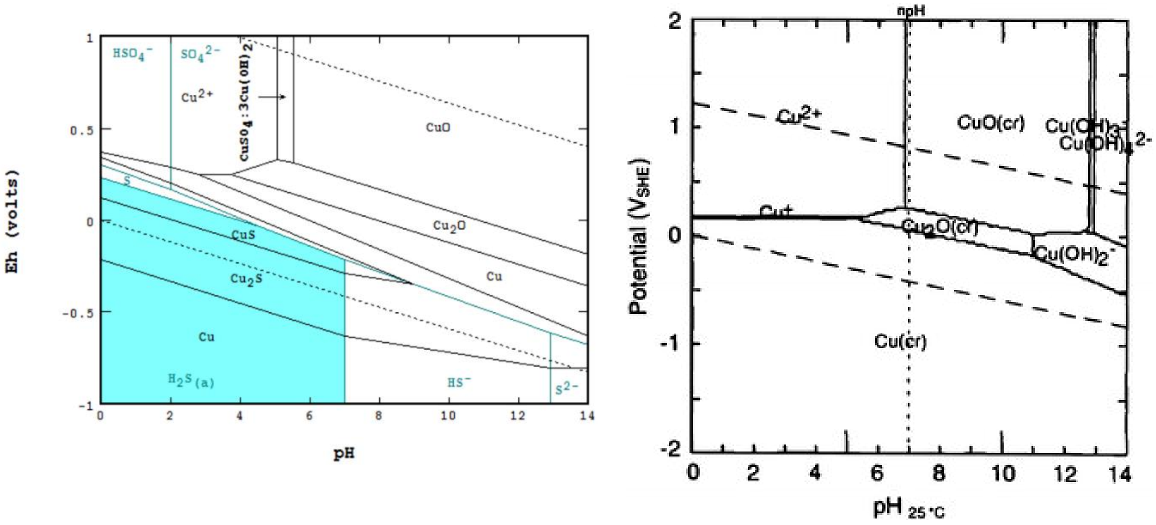

Figure A3 The Eh-PH diagram for Cu(main)–S (ligand) (left) at 25ºC and 1 atm [21]; Cu-H_2O system (right) at 25ºC and 1 atm [25].

Table A6 Chemical properties of nine Ni reference materials used in this work, including solubility constants (K_{sp}) at 25 ℃.

Formula	Name	Crystal system	E_0 (eV)*	K_{sp}
NiS	Millerite	Trigonal [2]	8336.6	9.3×10^{-23} [8]
NiO	Bunsenite	cubic [9]	8345.2	na
$NiCl_2$	Nickel chloride	na	8345.3	na
$Ni_3(PO_4)_2$	Nickel phosphate	monoclinic [20]	8345.7	4.74×10^{-32} [17]
$Ni_3(PO_4)_2\cdot nH_2O$	Nickel phosphate	monoclinic [20]	8345.7	4.74×10^{-32} [17]
$NiCO_3\cdot 3Ni(OH)_2\cdot 4H_2O$	Basic nickel carbonate	na	8345.8	1.6×10^{-46} [39]
$NiSO_4\cdot 6H_2O$	Retgersite	Tetragonal [43]	8346.8	na
$NiSO_4\cdot 7H_2O$	Nickel sulfate heptahydrate	Orthorhombic [45]	8346.9	na
$Ni(OH)_2$	Nickel hydroxides	Hexagonal [52]	8347.3	6.6×10^{-18} [8]

All Ni compounds listed above have a coordination number of six except for NiS with a coordination number of five, and they all have an oxidation state of +2.

***:** E_0 is the energy value of the first peak of the first derivative of the experimental Ni K-edge XAS spectra.

****:** the concentration of Ni for basic nickel carbonate was calculated based on the formula of $NiCO_3\cdot 2Ni(OH)_2\cdot 3H_2O$ rather than $NiCO_3\cdot 3Ni(OH)_2\cdot 4H_2O$;

K_{sp} and molar solubility (with a unit of M or mol/L) are under air pressure and room temperature;

'Cal' means that the value was calculated using K_{sp};

'na': not available;

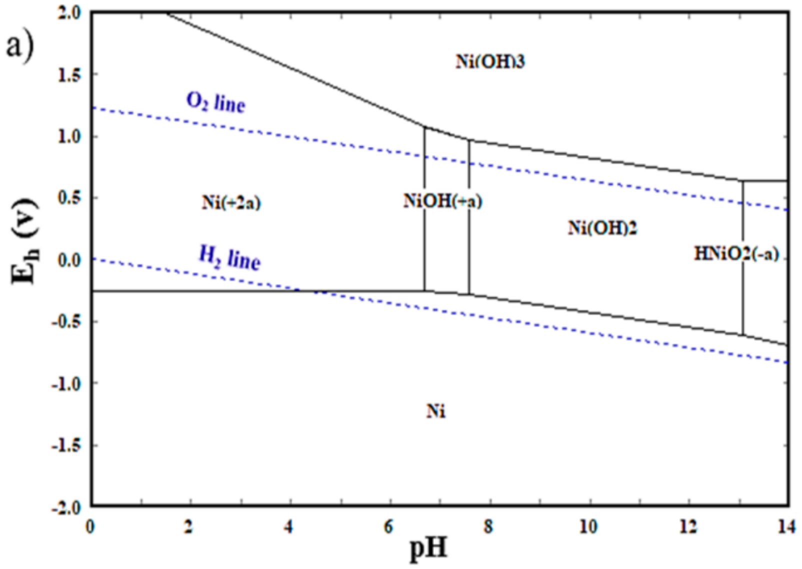

Figure A4 The Eh-PH diagram for Ni at 25ºC and 1 atm [30].

Table A7 Chemical properties of twelve Pb reference materials used in this work, including solubility constants (K_{sp}) at 25 ℃**.**

Formula	Name	Crystal system	E_0 (eV)*	Coordination type	K_{sp}
Pb	lead	na	13035.0	na	na
PbS	galena	na	13036.0	na	na
$PbCl_2$	lead chlorides	na	13036.0	na	na
na	Corning glass B	na	13036.0	na	na
na	Corning glass C	na	13036.0	na	na
PbO	litharge	tetragonal [7]	13036.9	Square pyramid [7]	na
PbO/SiO_2	Pb adsorbed on SiO_2	na	13036.9	4	na
$Pb_5(AsO_4)_3Cl$	mimetite	hexagonal [14]	13036.9	8&9 [14]	4.3×10^{-84} [23]
$Pb_5(PO_4)_3Cl$	pyromorphite	hexagonal	13036.9	8&9	2.5×10^{-84} [23]
$Pb_5(PO_4)_3OH$	hydroxypyromorphite	hexagonal	NA	8&9	1.0×10^{-73}-1.0×10^{-70} [23]
$PbCO_3$	cerussite	orthorhombic [33]	13037.8	9 [33]	7.4×10^{-14} [8]
$PbSO_4$	anglesite	orthorhombic [46]	13037.8	12 [46]	1.6×10^{-8} [8]
$PbCO_3 \cdot Pb(OH)_2$	lead basic carbonate	trigonal [55]	13037.9	3&7 (1:2) [55]	na

All Ni compounds listed above have an oxidation state of +2 except for metallic lead (0);
'NA': not available;
***:** E_0 is the energy value of the first peak of the first derivative of the experimental Pb K-edge XAS spectra;
NA refers to not available.

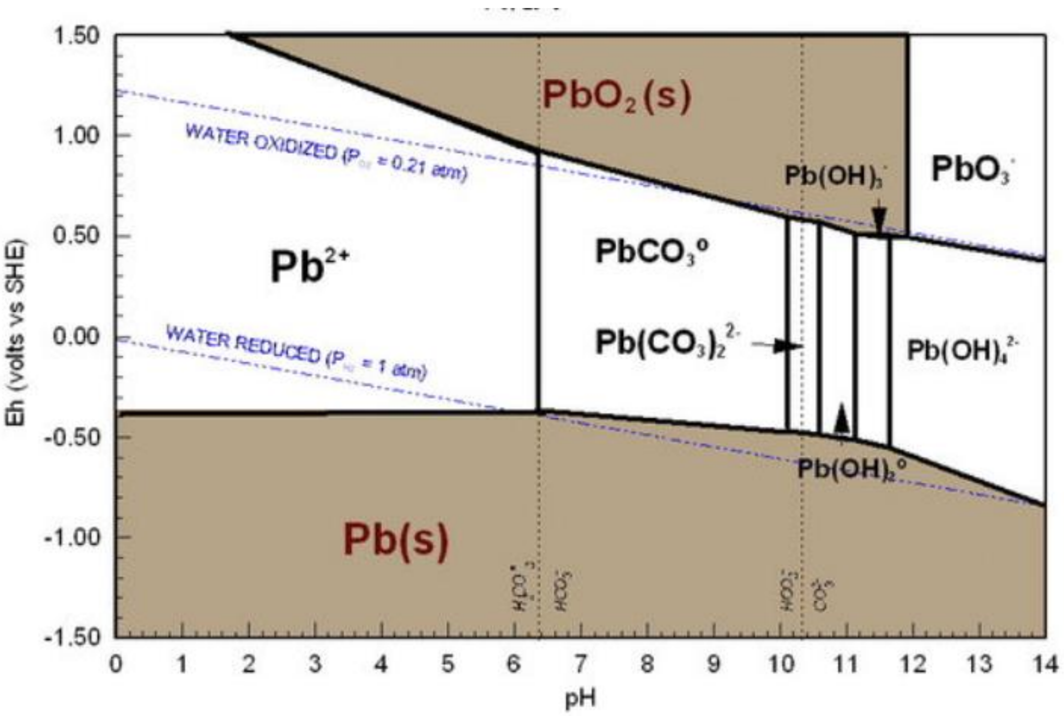

Figure A5 The Eh-pH diagram for Pb species activities of 0.015 mg/L and DIC = 10 mg/L as C, at 25° C and 1 atm lead [34].

Table A8 Chemical properties of twenty-three Zn reference materials used in this work, including solubility constants (Ksp) at 25 ℃

Formula	Name	Crystal system	E_0 (eV)*	Coordination type	K_{sp}
Zn	zinc	fcc	9659.00	NA	NA
ZnO/SiO_2	NA	NA	9661.31	NA	NA
ZnS	sphalerite	cubic[3]	9661.63	T [3]	1.0×10^{-23}
ZnO	zincite	hexagonal[13]	9661.96	T [13]	$1.0\times10^{-16.4}$ [24]
ε-$Zn(OH)_2$	wulfingite	NA	9662.29	T	$1.0\times10^{-16.9}$ [26, 32]
$ZnAl_2O_4$	gahnite	cubic[35]	9662.94	T [35]	NA
$Zn_4Si_2O_7(OH)_2{\cdot}H_2O$	hemimorphite	orthorhombic[47]	9662.94	T[47]	$1.0\times10^{-30.6}$ [53]
NA	IR-Xglass	NA	9662.94	NA	NA
NA	Glass 2.6	NA	9662.94	T	NA
α-Zn_2SiO_4	willemite	trigonal	9662.95	T	NA
$ZnCl_2$	NA	NA	9662.94	NA	NA
$Zn_2AsO_4OH{\cdot}H_2O$	legrandite	orthorhombic[1]	9663.23	TB&O [1]	NA
$2ZnCO_3{\cdot}3Zn(OH)_2$	hydrozincite	monoclinic[61]	9663.27	T&O (2:3) [61]	$1.0\times10^{-14.9}$ [26]
$ZnFe_2O_4$	franklinite	cubic[63]	9663.31	T [63]	NA
Nano $ZnFe_2O_4$	nano franklinite	cubic[65]	9663.44 [65]	T&O [65]	NA
α-$Zn_3(PO_4)_2$	α-Zinc orthophosphate	monoclinic[67]	9663.60	T [67]	NA

Continued to previous page

Zn_2AsO_4OH	adamite	orthorhombic[1]	9663.60	TB&O [1]	NA
$Ca_2ZnSi_2O_7$	hardystonite	tetragonal[10]	9663.70[19]	T [10]	NA
$ZnSO_4{\cdot}7H_2O$	goslarite	orthorhombic	9664.26	O	$1.0\times10^{2.3}$ [26]
$ZnSO_4{\cdot}H_2O$	gunningite	monoclinic[31]	9664.59	O [31]	$1.0\times10^{2.3}$
$ZnCO_3$	smithsonite	trigonal	9665.26	O	$1.5\times10^{-10.0}$ [41]
β-$Zn_3(PO_4)_2$	β-Zinc orthophosphate	monoclinic[42]	NA	T&TB (1:2) [42]	NA
γ-$Zn_3(PO_4)_2$	γ-Zinc orthophosphate	monoclinic[48]	NA	T&O (2:1) [48]	$1.0\times10^{-34.0}$ [54]

All Zn compounds listed above have an oxidation state of +2 except for metallic Zn (0);
***:** E_0 is the energy value of the first peak of the first derivative of the experimental Zn K-edge XAS spectra;
K_{sp} and molar solubility (with a unit of M or mol/L) are under air pressure and room temperature;
'T' refers to tetrahedron; 'O' stands for octahedron; 'TB' means trigonal bipyramid;
'Cal' means that the value was calculated using Ksp;
9662.94
'NA': not available.

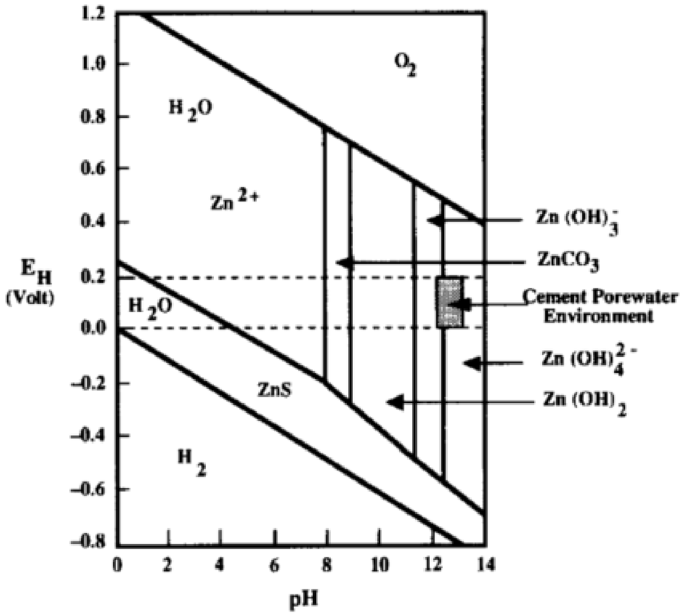

Figure A6 The Eh-pH diagram for the Zn-O-H-S-C system at 25ºC and 1 atm [38].

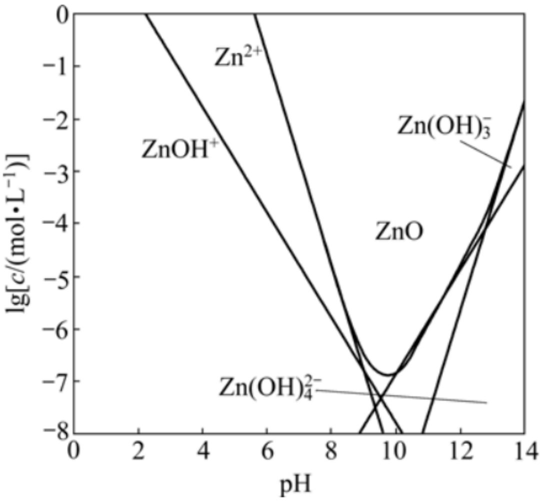

Figure A7 Solubility of ZnO as function of pH at 25 ºC and 1 atm [44].

A.2 Structure and Formation of Minerals of Elements of Interest

A.2.1 Arsenic Minerals

Realgar (As_4S_4) and orpiment (As_2S_3) are arsenic sulfides and commonly found in the same deposit, e.g., ore. Both minerals belong to the monoclinic crystal system, in which arsenic is tetrahedrally bonded with sulfur atoms as AsS_4 in As_4S_4 [4] and arsenic is trigonal pyramidal coordinated with sulfur atoms as AsS_3 in As_2S_3 [11].

The claudetite (As_2O_3) is an arsenic trioxide, which typically forms as an oxidation product of arsenic sulfide, at high temperatures above 900 °C. As shown in Eq.(A1), arsenic sulfide can react with oxygen to form gas arsenic, and the gas arsenic transfers into slag phase in form of As_2O_3 (s) by oxidation reaction [56]. Wang [56] reported that the reactions can remain spontaneous when temperature is at 1200 °C. It has a cubic crystal system, and each arsenic atom is surrounded by three oxygen atoms, and each oxygen has two close arsenic neighbors [28].

Arsenic oxyanion, e.g., $As(III)O_2^-$ and $As(V)O_4^{3-}$, can form by the reaction of arsenic oxide and hydroxide (Eq.(A2)). These oxyanions can precipitate with metals to form metal arsenic oxyanions, such as $NaAsO_2$, $Ca_3(AsO_4)_2$ and $Zn_2AsO_4(OH)$ (Eq.(A3)). The sodium polymetaarsenite ($NaAsO_2$) has each arsenic atom at the center and three oxygen atoms at the corners of an equilateral triangle. Similar as $Ca_3(PO_4)_2$ [40], $Ca_3(AsO_4)_2$ has a monoclinic crystal system, and each arsenic atom is tetrahedrally surrounded by four oxygen atoms. The adamite, $Zn_2AsO_4(OH)$, has a orthorhombic structure, and the tetrahedral AsO_4 groups connect with the two Zn polyhedron types, i.e., $ZnO_4(OH)_2$ octahedra and $ZnO_4(OH)$ trigonal bipyramids [1].

Equations for formation

$$As(III)_2S_3 + O_{2\,(g)} \rightarrow 2AsS\,(_g) + SO_{2\,(g)}, \qquad (A1)$$

$$2AsS\,(_g) + 2O_{2\,(g)} \rightarrow As_2\,(_g) + 2SO_{2\,(g)},$$

$$As_2\,(_g) + O_{2\,(g)} \rightarrow 2AsO\,(_g),$$

$$4AsO\,(_g) + O_{2\,(g)} \rightarrow 2As(III)_2O_3\,(_s)$$

$$As(III)_2O_3 + 2OH^- \rightarrow 2As(III)O_2^- + H_2O \tag{A2}$$

$$As(III)_2O_5 + 3OH^- \rightarrow 2As(V)O_4^{3-} + 3H_2O$$

$$As(III)O_2^- + Na^+ \rightarrow NaAs(III)O_2 \tag{A3}$$

$$As(V)O_4^3 + 3Ca^{2+} \rightarrow Ca_3(As(V)O_4)_2$$

$$As(V)O_4^3 + 3Zn^{2+} \rightarrow Zn_3(As(V)O_4)_2$$

A.2.2 Chromium Minerals

Chromium(III) sulfides are usually nonstoichiometric compounds, with formulas ranging from CrS to $CrS_{1.5}$ (corresponding to Cr_2S_3). Cr_2S_3 has trigonal and rhombohedral crystal systems [5], in which Cr has a octahedral coordination.

Chromium forms strong complexes with hydroxides. $Cr(OH)_3$ dominates the system when pH is 6.3 to 11.5, while $CrOH^{2+}$ dominates at pH 3.8-6.3 and $Cr(OH)_4^-$ dominates at pH over 11.5 (Eq.(A4)) [66]. This is close to the observation from the Eh-pH diagram reported in Huang [17], Barnhart [18]. With the presence of Fe^{3+}, co-precipitated Cr_xFe_{1-x}-(oxy)hydroxide intermediate compositions tend to form before the Cr-(oxy)hydroxide end member composition since it has a lower solubility [68].

At strong alkaline environment, Cr_2O_3 is likely oxidised to form CrO_4^{2-} (Eq.(A5)). Sodium chromate, Na_2CrO_4, has an orthorhombic crystal system, in which each chromium atom is bonded with four oxygen atoms, and each sodium atom is surrounded by six oxygen atoms [49].

Iron chromite, $FeCr_2O_4$, belongs to spinel group, with general formula AB_2X_4, in which the divalent A cation can be Cd, Cu, Co, Cr, Fe, Mg, Mn, Ni, Sn, and Zn and trivalent B can be Al, Cr, Co, Fe, In, Mn, Ni, Ti, and V, while X can be O, S, Se, etc. [69, 70]. $FeCr_2O_4$ can form at a annealing temperature of over 500°C from their metal oxides (Eq.(A6)). $FeCr_2O_4$ has a cubic crystal system, in which each chromium atom is octahedrally coordinated with six oxygen atoms [29].

Equations for formation

$$Cr(OH)_3 + OH^- \rightarrow Cr(OH)_4^- \tag{A4}$$

$$Cr_2O_3(s) + 3O_2(g) + 8OH- \rightarrow 4CrO_4^{2-} + 4H_2O \tag{A5}$$

$$Cr_2O_3 + FeO \xrightarrow{>500℃} FeCr_2O_4 \tag{A6}$$

A.2.3 Copper Minerals

Copper sulfides, e.g., chalcocite, Cu_2S and covellite, CuS, can naturally occur in the deposit, e.g., ore. Cu_2S is monoclinic, and the copper atom is present as trigonal planar with three sulfur atoms [6]. CuS contains tetrahedral Cu and triangular Cu with a ratio of 2:1 [15].

Copper ion and hydroxide can precipitate as spertiniite, $Cu(OH)_2$ (Eq.(A7)). $Cu(OH)_2$ is orthorhombic and the coordination of copper atom is square pyramidal with five hydroxyl (OH^-) [51]. $Cu(OH)_2$ can absorb CO_2 from the air to generate $CuCO_3$ (Eq.(A8)). With the increase of alkalinity, $CuCO_3$ reacts with OH^- to form malachite, $CuCO_3{\cdot}Cu(OH)_2$ (Eq.(A9)).

Copper ion and phosphate can precipitate as $Cu_3(PO_4)_2$. $Cu_3(PO_4)_2$ is triclinic, and half of the Cu atoms are in distorted square planar coordination, and half of Cu atoms are in irregular trigonal bipyramidal coordination [58].

Copper ion and hydroxide can precipitate as atacamite, $Cu_2Cl(OH)_3$, with the presence of chloride (Eq.(A10)). $Cu_2Cl(OH)_3$ is rapidly dissolved or replaced by other copper minerals when it is exposed to low-salinity waters [71]. $Cu_2Cl(OH)_3$ is orthorhombic, and the half of Cu atoms are in distorted octahedral with five hydroxyl groups and one Cl atom and half of Cu atoms are in square planar with four oxygen atoms [62].

Chalcanthite, $CuSO_4{\cdot}5H_2O$ is triclinic, in which the Cu atom is octahedral coordination [64]. Tenorite, CuO is monoclinic, and the copper atom is coordinated by four coplanar oxygen atoms [27].

Equations for formation

$$Cu^{2+} + 2OH^- \rightarrow Cu(OH)_2 \tag{A7}$$

$$Cu(OH)_2 + CO_2 \rightarrow CuCO_3 + H_2O \tag{A8}$$

$$CuCO_3 + Cu(OH)_2 \rightarrow CuCO_3{\cdot}Cu(OH)_2 \tag{A9}$$

$$Cu^{2+} + 3OH^- + Cl^- \rightarrow Cu_2Cl(OH)_3 \tag{A10}$$

A.2.4 Nickel Minerals

Nickel ions can precipitate with hydroxyl, phosphate, sulfate ions to form $Ni(OH)_2$ (Eq.(A11)), $Ni_3(PO_4)_2$ (Eq.(A12)), and $NiSO_4$ (Eq.(A13)). $Ni(OH)_2$ can absorb CO_2 from the air to generate $NiCO_3{\cdot}Ni(OH)_2$ (Eq.(A14)) and then $NiCO_3$ (Eq.(A15)). Ni in those compounds is octahedrally coordinated with six oxygen atoms.

Equations for formation

$$Ni^{2+} + 2OH^- \rightarrow Ni(OH)_2 \tag{A11}$$

$$3Ni^{2+} + 2PO_4^{3-} \rightarrow Ni_3(PO_4)_2 \tag{A12}$$

$$Ni^{2+} + SO_4^{2-} \rightarrow NiSO_4 \tag{A13}$$

$$NiCO_3 + CO_2 \rightarrow NiCO_3{\cdot}\ Ni(OH)_2 \tag{A14}$$

$$Ni(OH)_2 + CO_2 \rightarrow NiCO_3 + H_2O \tag{A15}$$

A.2.5 Lead Minerals

Galena, PbS, can naturally form in the deposit. It has a cubic crystal structure, in which Pb atoms are octahedrally bonded with six oxygen atoms [72]. Litharge, PbO, is tetragonal, and each Pb atom is bound to four oxygen atoms forming a square pyramid with a lead atom at the apex [7].

Mimetite ($Pb_5(AsO_4)_3Cl$), pyromorphite ($Pb_5(PO_4)_3Cl$) and hydroxypyromorphite ($Pb_5(PO_4)_3OH$) are apatite group minerals with general formula $A_5(XO_4)_3Z$, where A=Ba, Ca, Ce, K, Na, Pb, Sr, Y; X=As, P, Si, V and Z=F, Cl, O, OH, H_2O [23]. Solid-solution between end-members is extensive. All three apatite minerals are hexagonal, and contain two types of Pb. One Pb has nine-fold coordination to six oxygen atoms and three oxygen atoms of neighbouring AsO_4 or PO_4 groups;

another Pb forms seven-fold coordination with six oxygen atoms and one chloride atom or hydroxyl ions.

Lead ions and hydroxyl ions can precipitate as lead hydroxide ($Pb(OH)_2$) (Eq.(A16)). At ambient temperature and open to the atmosphere, $Pb(OH)_2$ can absorb CO_2 from the air to generate cerussite, $PbCO_3$ (Eq.(A17)). $PbCO_3$ is orthorhombic, and each Pb atom is coordinated with six oxygen atoms with neighbouring PbO_9 polyhedra, and three oxygen atoms with CO_3 groups [33].

With the increase of alkalinity, $PbCO_3$ reacts with OH^- to form lead basic carbonate, $PbCO_3{\cdot}Pb(OH)_2$ (Eq.(A18)). Precipitation of $PbCO_3{\cdot}Pb(OH)_2$ dominates over $PbCO_3$ or $Pb(OH)_2$ between pH 10.0 and 10.6 while precipitation of $PbCO_3$ and $Pb(OH)_2$ predominates below pH 10.0 and over pH 10.6, respectively [34]. When the pH continues to increase (pH=11.2-14.0), $PbCO_3{\cdot}Pb(OH)_2$ or $Pb(OH)_2$ will react with OH^- to form more soluble $Pb(OH)_3^-$ and then $Pb(OH)_4^{2-}$ at pH>11.8 (Eq.(A19)) [73, 74]. As a trigonal crystal, $PbCO_3{\cdot}Pb(OH)_2$ has a $Pb(OH)_2$ sheet sandwiched between two $PbCO_3$ sheets [55]. For $PbCO_3$ sheet, each Pb atom is bound with six oxygen atoms, belonging to three CO_3^{2-} groups, and one single oxygen atom. For $Pb(OH)_2$ sheet, each Pb atom is connected with three OH^- ions [55].

Anglesite ($PbSO_4$) is orthorhombic crystal system, and each Pb atom is bonded with ten oxygen atoms with neighbouring PbO_{12} polyhedra, and two oxygen atoms with neighbouring SO_4 groups [46].

Equations for formation

$$Pb^{2+} + 2OH^- \rightarrow Pb(OH)_{2(s)} \qquad (A16)$$

$$Pb(OH)_{2(aq)} + CO_2 \rightarrow PbCO_{3(s)} + H_2O \qquad (A17)$$

$$PbCO_3 + Pb(OH)_2 \rightarrow PbCO_3{\cdot}Pb(OH)_{2(s)} \qquad (A18)$$

$$Pb(OH)_2 + OH^- \rightarrow Pb(OH)_3^- \qquad (A19)$$

$$Pb(OH)_2 + 2OH^- \rightarrow Pb(OH)_4^{2-}$$

A.2.6 Zinc Minerals

Zinc ions and hydroxy can precipitate as $Zn(OH)_2$ (Eq.(A20)). At ambient temperature and open to the atmosphere, $Zn(OH)_2$ can absorb CO_2 from the air to generate $ZnCO_3$ (Eq.(A21)). With the increase of alkalinity, $ZnCO_3$ reacts with OH^- to form hydrozincite, $2ZnCO_3{\cdot}3Zn(OH)_2$ (Eq.(A22)). Precipitation of $2ZnCO_3{\cdot}3Zn(OH)_2$ dominates over $ZnCO_3$ or $Zn(OH)_2$ between pH 6.8 and 10 while precipitation of $ZnCO_3$ and $Zn(OH)_2$ predominate below pH 6.8 and over pH10, respectively [75, 76]. When the pH continues to increase (pH=11.5-12.5), $2ZnCO_3{\cdot}3Zn(OH)_2$ or $Zn(OH)_2$ will react with OH^- to form more soluble $Zn(OH)_3^-$ and then $Zn(OH)_4^{2-}$ at pH>12.5 (Eq.(A23)) [73, 74]. $2ZnCO_3{\cdot}3Zn(OH)_2$ is monoclinic, in which Zn has a tetrahedrally and octahedrally combined coordination with a ratio of 2:3 [61]. $2ZnCO_3{\cdot}3Zn(OH)_2$ can be decomposed between 155-340 °C [77, 78].

Hemimorphite ($Zn_4Si_2O_7(OH)_2{\cdot}H_2O$), also called hydrous zinc silicate, is a weathering product, which can occur naturally with γ-$Zn(OH)_2$ and/or Zn_2SiO_4 at a relatively low temperature (Eq.(A24)) [79, 80]. Specifically, zinc silicate (e.g., Zn_2SiO_4) adsorbs onto the precipitated $Zn(OH)_2$, breaking its structure, to form amorphous $Zn_4Si_2O_7(OH)_2{\cdot}H_2O$ which is then transferred to bulk crystal over a long period of 30 days. $Zn_4Si_2O_7(OH)_2{\cdot}H_2O$ is orthorhombic, in which Zn is tetrahedrally coordinated with three oxygen atoms and one OH [47]. It belongings to sorosilicate minerals with two silicate tetrahedra ($Si_2O_7^{2-}$) linked together by sharing one oxygen atom [47]. $Zn_4Si_2O_7(OH)_2{\cdot}2H_2O$ is easily dehydrated over 270°C and decomposed at temperatures over 550 °C [81].

Adamite ($Zn_2As(V)O_4OH$) and legrandite ($Zn_2As(V)O_4OH{\cdot}H_2O$), also called zinc arsenate hydroxide, are also weathering products. It can occur naturally in the oxidized zone of zinc- and arsenic-bearing hydrothermal mineral deposits. It belongings to the olivenite group with general formula of AB(CO4)D, where A refers to Zn^{2+}, Fe^{3+}, Mn^{2+}, Cu^{2+}; B can be Zn^{2+}, Mn^{2+}, Cu^{2+}; C refers to P, As and Sb; D can be OH and O. Both are orthorhombic, in which Zn has a mixed trigonal bipyramid and octahedral coordination.

Zinc sulfate is a family of inorganic compounds with the formula $ZnSO_4(H_2O)_x$, in which goslarite, $ZnSO_4{\cdot}7H_2O$ is the most common form. Zinc sulfates are soluble in water at room temperature [26]. $ZnSO_4 \cdot 7H_2O$ has an orthorhombic crystal system, while gunningite, $ZnSO_4 \cdot H_2O$ has a monoclinic system, in which Zn is octahedrally bonded with six oxygen atoms for both [31].

Zinc and phosphate ions can precipitate as $Zn_3(PO_4)_2$ (Eq.(A25)), even at low pH. $Zn_3(PO_4)_2$ has three common forms, i.e., α, β and γ. All three forms of $Zn_3(PO_4)_2$ have a monoclinic crystal system but β-$Zn_3(PO_4)_2$ consists of ZnO_4 tetrahedron (1/3) and ZnO_4 trigonal bipyramid (1/3) [42], and α and γ-$Zn_3(PO_4)_2$ consists of ZnO_4 tetrahedron (2/3) and $ZnO_2(H_2O)_4$ octahedron (1/3) [48, 67].

The bulk spinels $ZnFe_2O_4$ and $ZnAl_2O_4$ can be formed by Zn oxide in conjunction with a variety of other elements at a high temperature. Gibbs free energies for the formation reaction demonstrate that the ease of formation for Zn spinels follows the order: $ZnAl_2O_4$ (Eq.(A26)) and $ZnFe_2O_4$ (Eq.(A27)) [82]. $ZnFe_2O_4$ and $ZnAl_2O_4$ have a cubic crystal system, in which Zn is tetrahedrally bonded with four oxygen atoms and Fe or Al is octahedrally bonded with six oxygen atoms [35]. Nano spinels can form at a lower temperature and different methods. For example, nano $ZnFe_2O_4$ can be produced at a high temperature (900-1000°C) by sol-gel method [83] with a crystalline size range from 11-20 mm, or at a low temperature by coprecipitation (20-80°C) [84-86] and solvothermal synthesis (160-200°C) [83], with a crystalline size range from 3-19 nm and 5-10 nm. Compared to the bulk $ZnFe_2O_4$, partial tetrahedral Zn would transfer to octahedral Zn and the inversion degree varies due to different methods, negatively related to the crystallite size. The distortion crystal structure was also revealed by the Fourier Transform spectra of Zn K-edge XAS that the second peak was very week and broad, and the peak location moved forward from 3.1 Å to 2.8 Å for coprecipitated nano $ZnFe_2O_4$ [84]. The similar pattern was shown in the co-precipitated nano $ZnFe_2O_4$ prepared using urea as a precursor [85, 86].

Willemite (α-Zn_2SiO_4) can be synthesised by direct reaction of ZnO-SiO_2 between 800-1000 °C [87]. Condition for the hydrothermal formation of Zn_2SiO_4 has been suggested to be 1300°C for 3 hours (Eq.(A28)) [88]. It is less preferably formed than those two spinels, $ZnFe_2O_4$, and $ZnAl_2O_4$, at a high annealing temperature according to the higher Gibb free energy for Zn_2SiO_4 [82]. α-Zn_2SiO_4 is a zinc nesosilicate, belonging to olivine group with a general formula of X_2SiO_4, where X refers to Fe, Mg, Ca, Mn, Ni and Zn, etc. and can substitute for each other. Zn is in two disordered tetrahedral sites, and each is linked to four SiO_4 tetrahedra [89].

Hardystonite ($Ca_2ZnSi_2O_7$) can be synthesized by reaction of CaO-ZnO-SiO_2 at 1175.7 °C for 1h (Eq.(A29)) [90]. Nano $Ca_2Zn(Si_2O_7)$ can form in the $CaCO_3$–ZnO-SiO_2 the system with 20h milling and subsequent sintering at 900°C for 3h but the product is a mix of $Ca_2Zn(Si_2O_7)$ and α-Zn_2SiO_4 [91]. Then nano $Ca_2Zn(Si_2O_7)$ can transfer to bulk $Ca_2Zn(Si_2O_7)$ by milling longer and sintering at a higher temperature of 1100°C [91] or 1200°C [92], in which all α-Zn_2SiO_4 transfers to $Ca_2Zn(Si_2O_7)$ (Eq.(A29)). $Ca_2ZnSi_2O_7$ is a calcium zinc sorosilicate, similar as $Zn_4Si_2O_7(OH)_2{\cdot}H_2O$, in which zinc atoms are tetrahedrally bonded with four oxygen atoms, while the tetrahedral oxygen atoms are shared by adjacent silicon tetrahedra [10].

Equations for formation

$$Zn^{2+} + 2OH^- \rightarrow Zn(OH)_{2(s)} \qquad \text{(A20)}$$

$$Zn(OH)_{2(aq)} + CO_2 \rightarrow ZnCO_{3(s)} + H_2O \qquad \text{(A21)}$$

$$2ZnCO_3 + 3Zn(OH)_2 \rightarrow 2ZnCO_3{\cdot}3Zn(OH)_{2(s)} \qquad \text{(A22)}$$

$$Zn(OH)_2+OH^- \rightarrow Zn(OH)_3^- \qquad \text{(A23)}$$

$$Zn(OH)_2+2OH^- \rightarrow Zn(OH)_4^{2-}$$

$$Zn_2SiO_4 + \gamma\text{-}Zn(OH)_2 \xrightarrow{180℃} Zn_4Si_2O_7(OH)_2{\cdot}H_2O \qquad \text{(A24)}$$

$$3Zn^{2+} + 2PO_4^{3-} \rightarrow Zn_3(PO_4)_{2(s)} \qquad \text{(A25)}$$

$$ZnO + Al_2O_3 \xrightarrow{1000℃\text{ for 3h}} ZnAl_2O_4 \qquad \text{(A26)}$$

$$ZnO + Fe_2O_3 \xrightarrow{1000℃\text{ for 3h}} ZnFe_2O_4 \qquad \text{(A27)}$$

$$2ZnO + SiO_2 \xrightarrow{1300℃\text{ for 3h}} \alpha\text{-}Zn_2SiO_4 \qquad \text{(A28)}$$

$$ZnO + 2CaO + 2SiO_2 \xrightarrow{1100-1200℃} Ca_2Zn[Si_2O_7] \qquad \text{(A29)}$$

$$Zn_2SiO_4 + CaO + SiO_2 \xrightarrow{1100-1200℃} Ca_2Zn[Si_2O_7]$$

A.3 Coordination Information of Minerals of the Elements of Interest

The neighbouring species, coordination numbers and distances of minerals of the elements of interest that were used for curve fitting have been collected from the literature and summarised in Tables A9-A12.

Table A9 The coordination numbers (CN), distances (R), and neighbouring species of Cr minerals from the literatures.

Cr minerals	NS	CN_{ran}	CN_{ave}	R $(Å)_{ran}$	R $(Å)_{ave}$	Ref.
Cr_2O_3	Cr-O	6.0-6.0	6.0	1.980-2.010	1.990	[93, 94]
	Cr-Cr	3.0-4.0	3.7	2.800-2.900	2.800	[93, 94]
	Cr-O	3.0-3.0	3.0	3.350-3.370	3.360	[93, 94]
	Cr-O	4.0-9.0	6.3	3.570-3.660	3.610	[93, 94]
	Cr-Cr	3.0-9.0	6.3	3.550-3.660	3.620	[93, 94]

NS: neighbouring species; CN_{ran}: the range of coordination number; CN_{ave}: the average value of coordination number;
R $(Å)_{ran}$: the range of distance; CN_{ave}: the average value of distance; Ref.: reference.

Table A10 The coordination numbers (CN), distances (R), and neighbouring species of Cu minerals from the literatures.

Cu minerals	NS	CN_{ran}	CN_{ave}	R (Å)$_{ran}$	R (Å)$_{ave}$	Ref.
Cu	Cu-Cu	/	12.0	/	2.548	[95]
	Cu-Cu	/	6.0	/	3.571	[95]
	Cu-Cu	/	24.0	/	4.466	[95]
CuS	Cu-S	3.0-3.5	3.1	2.190-2.280	2.242	[15, 96-98]
	Cu-S	6.0-6.0	6.0	3.199-3.240	3.220	[15, 96]
	Cu-S	6.0-6.0	6.0	3.755-3.800	3.778	[15, 96]
	Cu-Cu	6.0-6.0	6.0	3.794-3.830	3.812	[15, 96]

NS: neighbouring species; CN_{ran}: the range of coordination number; CN_{ave}: the average value of coordination number;
R (Å)$_{ran}$: the range of distance; CN_{ave}: the average value of distance; Ref.: reference.

Table A11 The coordination numbers (CN), distances (R), and neighbouring species of Ni minerals from the literatures.

Ni minerals	NS	CN_{ran}	CN_{ave}	R (Å)$_{ran}$	R (Å)$_{ave}$	Ref.
$Ni(OH)_2$	Ni-O	6.0-6.0	6.0	2.060-2.135	2.094	[99, 100]
	Ni-Ni	6.0-6.0	6.0	3.117-3.120	3.119	[99, 100]
	Ni-Ni	5.5-6.0	5.8	6.210-6.234	6.225	[99, 100]

NS: neighbouring species; CN_{ran}: the range of coordination number; CN_{ave}: the average value of coordination number;
R (Å)$_{ran}$: the range of distance; CN_{ave}: the average value of distance. Ref.: reference;

Table A12 The coordination numbers (CN), distances (R), and neighbouring species of Zn minerals from the literatures.

Zn minerals	NS	CN_{ran}	CN_{ave}	R (Å)$_{ran}$	R (Å)$_{ave}$	Ref.
ZnO	Zn-O	3.3-4.0	3.9	1.950-1.980	1.960	[101-111]
	Zn-Zn	11.7-12.4	12.0	3.190-3.230	3.210	[79, 103, 105, 107-112]
$Zn_5(CO_3)_2(OH)_6$	Zn-O	4.1-5.7	4.8	2.000-2.050	2.020	[104-106, 108-111]
	Zn-O	2.3-7.7	3.8	3.220-3.550	3.400	[105, 108-111]
β-$Zn_3(PO_4)_2$	Zn-O	4.0-5.0	4.7	1.980-2.090	2.050	[104]
	Zn-Zn	/	2.0	/	3.440	[103]
	Zn-Ca	2.0-2.0	2.0	3.780-3.780	3.780	[79, 103]
ZnS	Zn-S	4.0-4.3	4.2	2.330-2.350	2.340	[106, 108]
	Zn-Zn	/	5.4	/	3.800	[108]
	Zn-S	/	7.9	/	4.460	[108]
$ZnFe_2O_4$	Zn-O	3.7-4.0	3.9	1.980-1.990	1.990	[104-111]
	Zn-Fe	12.0-17.3	14.6	3.500-3.500	3.500	[107, 108]
	Zn-Zn	4.0-5.9	4.9	3.700-3.800	3.800	[107, 108]
$Zn_4Si_2O_7(OH)_2 \cdot H_2O$	Zn-O	4.0-4.0	4.0	1.940-1.950	1.95	[79, 105, 106, 108, 113, 114]
	Zn-Si	3.0-3.0	3.0	2.960-3.050	3.01	[79, 108, 113, 114]
	Zn-Zn	4.0-4.4	4.1	3.280-3.330	3.30	[79, 105, 108, 113, 114]

NS: neighbouring species; CN_{ran}: the range of coordination number; CN_{ave}: the average value of coordination number;
R (Å)$_{ran}$: the range of distance; CN_{ave}: the average value of distance. Ref.: reference;
/ refers to not available.

Reference

1. Council, N.R., Arsenic: Medical and Biologic Effects of Environmental Pollutants. 1977.
2. Hill, R., The crystal structure and infrared properties of adamite. *American Mineralogist*, 1976. **61**(9-10): p. 979-986.
3. Aqion. *Solubility product constants Ksp at 25°C*. [cited 2023 01/30]; Available from: https://www.aqion.de/site/16.
4. Huang, L., et al., Trivalent chromium solubility and its influence on quantification of hexavalent chromium in ambient particulate matter using EPA method 6800. *Journal of the Air & Waste Management Association*, 2014. **64**(12): p. 1439-1445. https://doi.org/10.1080/10962247.2014.951745.
5. Barnhart, J., Occurrences, uses, and properties of chromium. *Regulatory toxicology and pharmacology*, 1997. **26**(1): p. S3-S7. https://doi.org/10.1006/rtph.1997.1132.
6. Skinner, B.J., Unit-cell edges of natural and synthetic sphalerites*. *American Mineralogist*, 1961. **46**(11-12): p. 1399-1411.
7. Ito, T., Morimoto, N., and Sadanaga, R., The crystal structure of realgar. *Acta Crystallographica*, 1952. **5**(6): p. 775-782.
8. Jellinek, F., The structures of the chromium sulphides. *Acta Crystallographica*, 1957. **10**(10): p. 620-628. https://doi.org/10.1107/S0365110X57002200.
9. Evans Jr, H.T., The crystal structures of low chalcocite and djurleite. *Zeitschrift für Kristallographie-Crystalline Materials*, 1979. **150**(1-4): p. 299-320. https://doi.org/10.1524/zkri.1979.150.14.299.
10. Boher, P., et al., Monoxyde quadratique PbOα (I): Description de la transition structurale ferroe´ lastique. *Journal of Solid State Chemistry*, 1985. **57**(3): p. 343-350. https://doi.org/10.1016/0022-4596(85)90197-5.
11. Tessier, A., Campbell, P.G., and Bisson, M., Sequential extraction procedure for the speciation of particulate trace metals. *Analytical chemistry*, 1979. **51**(7): p. 844-851.
12. Ure, A., et al., Improvements in the determination of extractable contents of trace metals in soil sediment prior to certification. 1993, Commission of the European Communities—BCR Information.
13. Huang, H.-H., The Eh-pH diagram and its advances. *Metals*, 2016. **6**(1): p. 23. https://doi.org/10.3390/met6010023.
14. Sasaki, S., Fujino, K., and Takéuchi, Y., X-ray determination of electron-density distributions in oxides, MgO, MnO, CoO, and NiO, and atomic scattering factors of their constituent atoms. *Proceedings of the Japan Academy, Series B*, 1979. **55**(2): p. 43-48. https://doi.org/10.2183/pjab.55.43.
15. Lousnathan, S.J., Refinement of the crystal structure of hardystonite, $Ca_2ZnSi_2O_7$. *Zeitschrift für Kristallographie-Crystalline Materials*, 1969. **130**(1-6): p. 427-437. https://doi.org/10.1524/zkri.1969.130.16.427.
16. Stanjek, H. and Häusler, W., Basics of X-ray Diffraction. *Hyperfine Interactions*, 2004. **154**(1): p. 107-119. https://doi.org/10.1023/B:HYPE.0000032028.60546.38.

17. Brandt, I.S., et al., Electrodeposition of Cu_2O: growth, properties, and applications. *Journal of Solid State Electrochemistry*, 2017. **21**: p. 1999-2020. https://doi.org/10.1007/s10008-017-3660-x.
18. Mullen, D. and Nowacki, W., Refinement of the crystal structures of realgar, AsS and orpiment, As_2S_3. *Zeitschrift für Kristallographie-Crystalline Materials*, 1972. **136**(1-6): p. 48-65. https://doi.org/10.1524/zkri.1972.136.16.48.
19. Atkinson, T.D., Fjellvåg, H., and Kjekshus, A., Synthesis, structure, and properties of chromium (III) sulfates. *Journal of Solid State Chemistry*, 2004. **177**(11): p. 4351-4358. https://doi.org/10.1016/j.jssc.2004.03.038.
20. Kisi, E.H. and Elcombe, M.M., u parameters for the wurtzite structure of ZnS and ZnO using powder neutron diffraction. *Acta crystallographica. Section C, Crystal structure communications*, 1989. **45**(12): p. 1867-1870. https://doi.org/10.1107/s0108270189004269.
21. Escobal, J., et al., Neutron diffraction, specific heat and magnetic susceptibility of $Ni_3(PO_4)_2$. *Journal of Solid State Chemistry*, 2005. **178**(9): p. 2626-2634. https://doi.org/10.1016/j.jssc.2005.06.022.
22. Leciejewicz, J., On the crystal structure of tetragonal (red) PbO. *Acta Crystallographica*, 1961. **14**(12): p. 1304-1304. https://doi.org/10.1107/S0365110X61003892.
23. Rissler, J., et al., Identification and quantification of chemical forms of Cu and Zn in MSWI ashes using XANES. *Energy & Fuels*, 2020. **34**(11): p. 14505-14514. https://doi.org/10.1021/acs.energyfuels.0c02226.
24. Evans, H. and Konnert, J., Crystal structure refinement of covellite. *Am. Mineral*, 1976. **61**(9-10): p. 996-1000. https://doi.org/10.2475/ajs.s5-17.102.489
25. Ibrahim, A.H., et al., Cost-effective and high purity valuable metals extraction from water leaching solid residues obtained as a by-product from processing the Egyptian boiler ash. *Minerals*, 2022. **12**(9): p. 1084. https://doi.org/10.3390/min12091084.
26. Schock, M.R., et al. Mode of occurrence, treatment, and monitoring significance of tetravalent lead. in *AWWA Water Quality Technology Conference*. 2005. Quebec City, Quebec.
27. Li, W., Synthesis and solubility of arsenic tri-sulfide and sodium arsenic oxy-sulfide complexes in alkaline sulfide solutions. 2013, University of British Columbia.
28. Clara, M., Magalhães, F., and Williams, P.A., Apatite group minerals: solubility and environmental remediation, in Thermodynamics, solubility and environmental issues. 2007, *Elsevier*. p. 327-340.
29. Alwan, A.K. and Williams, P.A., Mineral formation from aqueous solution. Part I. The deposition of hydrozincite, Zn 5 (OH) 6 (CO 3) 2, from natural waters. *Transition Metal Chemistry*, 1979. **4**(2): p. 128-132.
30. Feitknecht, W. and Schindler, P., Solubility constants of metal oxides, metal hydroxides and metal hydroxide salts in aqueous solution. *Pure and Applied Chemistry*, 1963. **6**(2): p. 125-206.
31. Yousuf, M., et al., The interfacial chemistry of solidification/stabilization of metals in cement and pozzolanic material systems. *Waste Management*, 1995. **15**(2): p. 137-148. https://doi.org/10.1016/0956-053X(95)00013-P.
32. Asbrink, S. and Waskowska, A., CuO: X-ray single-crystal structure determination at 196 K and room temperature. *Journal of Physics:*

Condensed Matter, 1991. **3**(42): p. 8173. https://doi.org/10.1088/0953-8984/3/42/012.

33. Jr, F. and J, A., The crystal structure of claudetite (monoclinic As_2O_3). *American Mineralogist: Journal of Earth and Planetary Materials*, 1951. **36**(11-12): p. 833-850.
34. Lenaz, D., et al., Structural changes and valence states in the MgCr 2 O 4–FeCr 2 O 4 solid solution series. *Physics and Chemistry of Minerals*, 2004. **31**: p. 633-642. https://doi.org/10.1007/s00269-004-0420-0.
35. Wildner, M. and Giester, G., The crystal structures of kieserite-type compounds. I, Crystal structures of Me (II) SO_4.H2O (Me= Mn, Fe, Co, Ni, Zn). *Neues Jahrbuch für Mineralogie Monatshefte*, 1991(7): p. 296-306.
36. Zachara, J., et al., Solubility and surface spectroscopy of zinc precipitates on calcite. *Geochimica et Cosmochimica Acta*, 1989. **53**(1): p. 9-19. https://doi.org/10.1016/0016-7037(89)90268-8.
37. Li, H.-x., Wang, Y., and Cang, D.-q., Zinc leaching from electric arc furnace dust in alkaline medium. *Journal of Central South University of Technology*, 2010. **17**(5): p. 967-971. https://doi.org/10.1007/s11771-010-0585-2.
38. Zemann, J., et al., Neutron single-crystal refinement of cerussite, PbCO3, and comparison with other aragonite-type carbonates. *Zeitschrift für Kristallographie-Crystalline Materials*, 1992. **199**(1-4): p. 67-74. https://doi.org/10.1524/zkri.1992.199.14.67.
39. Mitchell, D., et al., Ab initio electric-field gradients and electron densities at Al 27, Fe 57, and Zn 67 in the spinels ZnAl 2 O 4 and ZnFe 2 O 4. *Physical Review B*, 1996. **53**(12): p. 7684.
40. Gogol, D.B., et al., Evaluation of solubility and thermodynamic properties of synthetic nickel hydroxide carbonate. *Available at SSRN 4616469*, 2023. http://dx.doi.org/10.2139/ssrn.4616469.
41. Dera, P., et al., Structural and electronic evolution of Cr_2O_3 on compression to 55 GPa. *Journal of Solid State Chemistry*, 2011. **184**(11): p. 3040-3049. https://doi.org/10.1016/j.jssc.2011.09.021.
42. Crocket, J.H. and Winchester, J.W., Coprecipitation of zinc with calcium carbonate. *Geochimica et Cosmochimica Acta*, 1966. **30**(10): p. 1093-1109. 10.1016/0016-7037(66)90119-0.
43. Bargouth, M. and Will, G., A neutron diffraction refinement of the crystal structure of tetragonal nickel sulfate hexahydrate. 1981, International Centre for Theoretical Physics.
44. Oswald, H.-R., et al., Structure of copper (II) hydroxide, Cu $(OH)_2$. *Acta Crystallographica Section C: Crystal Structure Communications*, 1990. **46**(12): p. 2279-2284. https://doi.org/10.1107/S0108270190006230.
45. Mathew, M., et al., The crystal structure of α-$Ca_3(PO_4)_2$. *Acta Crystallographica Section B: Structural Crystallography and Crystal Chemistry*, 1977. **33**(5): p. 1325-1333.
46. Iskhakova, L., Dubrovinskii, L., and Charushnikova, I., Crystal structure, calculation of parameters of atomic interaction potential and thermochemical properties of NiSO4· nH2O (n= 7, 6). *Kristallografiya*, 1991. **36**: p. 650-655.
47. Hill, R.J., et al., A neutron-diffraction study of hemimorphite. *Zeitschrift für Kristallographie-Crystalline Materials*, 1977. **146**(4-6): p. 241-259. https://doi.org/10.1524/zkri.1977.146.4-6.241.
48. Stephens, J.S. and Calvo, C., Crystal structure of β-$Zn_3(PO_4)_2$. *Canadian Journal of Chemistry*, 1967. **45**(20): p. 2303-2316. 10.1139/v67-376.

49. Wang, Q., et al., Reaction mechanism and distribution behavior of arsenic in the bottom blown copper smelting process. *Metals*, 2017. **7**(8): p. 302. https://doi.org/10.3390/met7080302.
50. Jacobsen, S.D., et al., Rigid-body character of the SO_4 groups in celestine, anglesite and barite. *Canadian mineralogist*, 1998. **36**: p. 1053-1060.
51. Miller, J., The cystal structure of anhydrous sodium chromate, Na_2CrO_4. *Zeitschrift für Kristallographie-Crystalline Materials*, 1936. **94**(1-6): p. 131-136.
52. Nishimura, T. and Robins, R., A re-evaluation of the solubility and stability regions of calcium arsenites and calcium arsenates in aqueous solution at 25 C. *Mineral Processing and Extractive Metullargy Review*, 1998. **18**(3-4): p. 283-308. https://doi.org/10.1080/08827509808914159.
53. Wells, A., Malachite: re-examination of crystal structure. *Acta Crystallographica*, 1951. **4**(3): p. 200-204. https://doi.org/10.1107/S0365110X51000714.
54. Medas, D., et al., Stability of biological and inorganic hemimorphite: Implications for hemimorphite precipitation in non-sulfide Zn deposits. *Ore Geology Reviews*, 2017. **89**: p. 808-821. https://doi.org/10.1016/j.oregeorev.2017.07.015.
55. Stephens, J.S. and Cruickshank, D.W.J., The crystal structure of (CrO_3)[infinity]. *Acta Crystallographica Section B*, 1970. **26**(3): p. 222-226. https://doi.org/10.1107/S0567740870002182.
56. Calvo, C., The crystal structure and luminescence of γ-zinc orthophosphate. *Journal of Physics and Chemistry of Solids*, 1963. **24**(1): p. 141-149. https://doi.org/10.1016/0022-3697(63)90049-0.
57. Cowley, J., Electron-diffraction study of the structure of basic lead carbonate, $2PbCO_3 \cdot Pb(OH)_2$. *Acta Crystallographica*, 1956. **9**(4): p. 391-396. https://doi.org/10.1107/S0365110X56001133.
58. Shoemaker, G., Anderson, J., and Kostiner, E., Copper (II) phosphate. *Acta Crystallographica Section B: Structural Crystallography and Crystal Chemistry*, 1977. **33**(9): p. 2969-2972. https://doi.org/10.1107/S0567740877010012.
59. Li, Y., et al., Removal of arsenic from arsenate complex contained in secondary zinc oxide. *Hydrometallurgy*, 2011. **109**(3): p. 237-244. https://doi.org/10.1016/j.hydromet.2011.07.007.
60. Jansen, M., Kristallstruktur von As_2O_5. *Angewandte Chemie*, 1977. **89**(5): p. 326-327. https://doi.org/10.1002/ange.19770890511
61. Dupuis, V., et al., Solubility and disintegration of zinc phosphate cement. *Biomaterials*, 1992. **13**(7): p. 467-470. https://doi.org/10.1016/0142-9612(92)90168-N.
62. Ghose, S., The crystal structure of hydrozincite, $Zn_5(OH)_6(CO_3)_2$. *Acta Crystallographica*, 1964. **17**(8): p. 1051-1057. https://doi.org/10.1107/S0365110X64002651.
63. Parise, J. and Hyde, B., The structure of atacamite and its relationship to spinel. *Acta Crystallographica Section C: Crystal Structure Communications*, 1986. **42**(10): p. 1277-1280. https://doi.org/10.1107/S0108270186092570.
64. Rai, D., Eary, L., and Zachara, J.M., Environmental chemistry of chromium. *Science of the total environment*, 1989. **86**(1-2): p. 15-23. https://doi.org/10.1016/0048-9697(89)90189-7.
65. Andersson, D.A. and Stanek, C.R., Mixing and non-stoichiometry in Fe–Ni–Cr–Zn–O spinel compounds: density functional theory calculations. *Physical*

Chemistry Chemical Physics, 2013. **15**(37): p. 15550-15564. https://doi.org/10.1039/C3CP50312G.

66. Iskhakova, L.D., et al., Crystal structure of chalcanthite $CuSO_4{\cdot}5H_2O$ grown under microgravity. *Kristallografiya*, 1991.
67. Tang, Y., et al., Structural properties of the Cr (III)− Fe (III)(Oxy) hydroxide compositional series: insights for a nanomaterial “solid solution”. *Chemistry of Materials*, 2010. **22**(12): p. 3589-3598. https://doi.org/10.1021/cm1000472.
68. Gomes, A.F.S., Lopez, D.L., and Ladeira, A.C.Q., Characterization and assessment of chemical modifications of metal-bearing sludges arising from unsuitable disposal. *Journal of Hazardous Materials*, 2012. **199-200**: p. 418-425. https://doi.org/10.1016/j.jhazmat.2011.11.039.
69. Calvo, C., The crystal structure of α-$Zn_3(PO_4)_2$. *Canadian Journal of Chemistry*, 1965. **43**(2): p. 436-445. https://doi.org/10.1139/v65-058.
70. *Spinel & inverse spinel crystal structures*. [cited 2021 7th March]; Available from: https://www.adichemistry.com/inorganic/cochem/spinels/spinel-structures.html.
71. Biagioni, C. and Pasero, M., The systematics of the spinel-type minerals: An overview. *American Mineralogist*, 2014. **99**(7): p. 1254-1264. https://doi.org/10.2138/am.2014.4816.
72. Cameron, E.M., Leybourne, M.I., and Palacios, C., Atacamite in the oxide zone of copper deposits in northern Chile: involvement of deep formation waters? *Mineralium Deposita*, 2007. **42**: p. 205-218. https://doi.org/10.1007/s00126-006-0108-0.
73. Noda, Y., et al., Charge distribution and atomic thermal vibration in lead chalcogenide crystals. *Acta Crystallographica Section B: Structural Science*, 1983. **39**(3): p. 312-317. https://doi.org/10.1107/S0108768183002463.
74. El-eswed, B.I., Chemical evaluation of immobilization of wastes containing Pb, Cd, Cu and Zn in alkali-activated materials: A critical review. *Journal of Environmental Chemical Engineering*, 2020. **8**(5): p. 104194. https://doi.org/10.1016/j.jece.2020.104194.
75. Reichle, R.A., McCurdy, K.G., and Hepler, L.G., Zinc hydroxide: solubility product and hydroxy-complex stability constants from 12.5–75 C. *Canadian Journal of Chemistry*, 1975. **53**(24): p. 3841-3845.
76. Shi, Q., et al., Effect of solution chemistry on the flotation system of smithsonite and calcite. *International Journal of Mineral Processing*, 2013. **119**: p. 34-39. https://doi.org/10.1016/j.minpro.2012.12.011.
77. Patterson, J.W., Allen, H.E., and Scala, J.J., Carbonate precipitation for heavy metals pollutants. *Journal (Water Pollution Control Federation)*, 1977: p. 2397-2410.
78. Hales, M.C. and Frost, R.L., Thermal analysis of smithsonite and hydrozincite. *Journal of thermal analysis calorimetry*, 2008. **91**(3): p. 855-860.
79. Vágvölgyi, V., et al., Dynamic and controlled rate thermal analysis of hydrozincite and smithsonite. *Journal of thermal analysis calorimetry*, 2008. **92**(3): p. 911-916.
80. Ziegler, F., et al., Sorption mechanisms of zinc to calcium silicate hydrate: X-ray absorption fine structure (XAFS) investigation. *Environmental Science & Technology*, 2001. **35**(7): p. 1550-1555. https://doi.org/10.1021/es001437+.

81. Yang, J., et al., Hydrothermal synthesis and optical properties of zinc silicate hierarchical superstructures. *Materials Letters*, 2011. **65**(19-20): p. 3030-3033. https://doi.org/10.1016/j.matlet.2011.06.068.
82. Nagata, H., Matsunaga, M., and Hosokawa, K., Analytical study of the formation process of hemimorphite-Part II. *Zairyo-to-Kankyo*, 1993. **42**(6): p. 377-383. https://doi.org/10.3323/jcorr1991.42.377.
83. Bisengalieva, M.R., et al., A thermal and thermochemical study of natural hemimorphite. *Russian Journal of Physical Chemistry A*, 2010. **84**(9): p. 1481-1484. https://doi.org/10.1134/S0036024410090050.
84. Li, M.-J., et al., Effects of SiO_2, Al_2O_3 and Fe_2O_3 on leachability of Zn, Cu and Cr in ceramics incorporated with electroplating sludge. *Journal of Environmental Chemical Engineering*, 2017. **5**(4): p. 3143-3150. https://doi.org/10.1016/j.jece.2017.06.019.
85. Blanco-Gutiérrez, V., et al., X-ray absorption spectroscopy and Mössbauer spectroscopy studies of superparamagnetic $ZnFe_2O_4$ nanoparticles. *The Journal of Physical Chemistry C*, 2011. **115**(5): p. 1627-1634. https://doi.org/10.1021/jp109368z.
86. Jeyadevan, B., Tohji, K., and Nakatsuka, K., Structure analysis of coprecipitated $ZnFe_2O_4$ by extended x-ray-absorption fine structure. *Journal of Applied Physics*, 1994. **76**(10): p. 6325-6327. https://doi.org/10.1063/1.358255.
87. Akhtar, M.J. and Nadeem, M., Structural studies of $ZnFe_2O_4$ nanoparticles by synchrotron X-ray absorption spectroscopy. *Thai Journal of Physics*, 2008.
88. Raeisi Shahraki, R., et al., Structural characterization and magnetic properties of superparamagnetic zinc ferrite nanoparticles synthesized by the coprecipitation method. *Journal of Magnetism and Magnetic Materials*, 2012. **324**(22): p. 3762-3765. https://doi.org/10.1016/j.jmmm.2012.06.020.
89. Babu, K.S., et al., High thermal annealing effect on structural and optical properties of ZnO–SiO2 nanocomposite. *Materials science in semiconductor processing*, 2014. **27**: p. 643-648. https://doi.org/10.1016/j.mssp.2014.07.055.
90. Nguyen, N.H., et al., Effect of Zn/Si ratio on the microstructural and microwave dielectric properties of Zn2SiO4 ceramics. *Journal of the American Ceramic Society*, 2007. **90**(10): p. 3127-3130. 10.1111/j.1551-2916.2007.01891.x.
91. Britannica, T. *Sorosilicate*. [cited 2021 9th March]; Available from: https://www.britannica.com/science/sorosilicate.
92. Gasek, K., et al., Characteristic of synthesis and transformations of hardystonite in willemite glass-crystalline glaze based on thermal analysis. *Journal of Thermal Analysis and Calorimetry*, 2016. **125**: p. 1135-1142. https://doi.org/10.1007/s10973-016-5429-3.
93. Sadeghzade, S., Emadi, R., and Labbaf, S., Formation mechanism of nano-hardystonite powder prepared by mechanochemical synthesis. *Advanced Powder Technology*, 2016. **27**(5): p. 2238-2244. https://doi.org/10.1016/j.apt.2016.08.010.
94. Wu, C.T., Chang, J., and Zhai, W.Y., A novel hardystonite bioceramic: preparation and characteristics. *Ceramics International*, 2005. **31**(1): p. 27-31. https://doi.org/10.1016/j.ceramint.2004.02.008.

95. Ahamad Mohiddon, M., et al., Chromium oxide as a metal diffusion barrier layer: An x-ray absorption fine structure spectroscopy study. *Journal of Applied Physics*, 2014. **115**(4). https://doi.org/10.1063/1.4863309.
96. Blacklocks, A.N., et al., An XAS study of the defect structure of Ti-doped α-Cr_2O_3. *Solid State Ionics*, 2006. **177**(33-34): p. 2939-2944. https://doi.org/10.1016/j.ssi.2006.08.028.
97. Kane, S., et al., Extended X-ray absorption fine structure (EXAFS) measurement of Cu metal foil using thermal wave detector: A comparative study. *Nuclear Instruments and Methods in Physics Research Section A: Accelerators, Spectrometers, Detectors and Associated Equipment*, 2024. **1060**: p. 169066. https://doi.org/10.1016/j.nima.2023.169066.
98. Tagirov, B.R., et al., Covellite CuS as a matrix for “invisible” gold: X-ray spectroscopic study of the chemical state of Cu and Au in synthetic minerals. *Geochimica et Cosmochimica Acta*, 2016. **191**: p. 58-69. https://doi.org/10.1016/j.gca.2016.07.015.
99. Pattrick, R., et al., The structure of amorphous copper sulfide precipitates: An X-ray absorption study. *Geochimica et Cosmochimica Acta*, 1997. **61**(10): p. 2023-2036. https://doi.org/10.1016/S0016-7037(97)00061-6.
100. Helz, G.R., Vaughan, D.J., and Garner, C.D., Multinuclearity of aqueous copper and zinc bisulfide complexes: An EXAFS investigation. *Geochimica et Cosmochimica Acta*, 1993. **57**(1): p. 15-25. https://doi.org/10.1016/0016-7037(93)90464-8.
101. Ichiyanagi, Y., et al., X-ray absorption fine-structure study on the $Ni(OH)_2$ monolayer nanoclusters. *Chemical physics letters*, 2003. **379**(3-4): p. 345-350. https://doi.org/10.1016/j.cplett.2003.08.051.
102. Pandya, K., et al., Extended X-ray absorption fine structure investigations of nickel hydroxides. *Journal of physical chemistry*, 1990. **94**(1): p. 21-26. https://pubs.acs.org/doi/pdf/10.1021/j100364a005.
103. Trivedi, P., Axe, L., and Tyson, T.A., An Analysis of Zinc Sorption to Amorphous versus Crystalline Iron Oxides Using XAS. *Journal of Colloid and Interface Science*, 2001. **244**(2): p. 230-238. https://doi.org/10.1006/jcis.2001.7971.
104. Albertsson, J., Abrahams, S., and Kvick, Å., Atomic displacement, anharmonic thermal vibration, expansivity and pyroelectric coefficient thermal dependences in ZnO. *Acta Crystallographica Section B: Structural Science*, 1989. **45**(1): p. 34-40. https://doi.org/10.1107/S0108768188010109.
105. Rose, J., et al., X-ray absorption spectroscopy study of immobilization processes for heavy metals in calcium silicate hydrates. 2. Zinc. *Langmuir*, 2001. **17**(12): p. 3658-3665. https://doi.org/10.1021/la001302h.
106. Waychunas, G.A., Fuller, C.C., and Davis, J.A., Surface complexation and precipitate geometry for aqueous Zn(II) sorption on ferrihydrite I: X-ray absorption extended fine structure spectroscopy analysis. *Geochimica et Cosmochimica Acta*, 2002. **66**(7): p. 1119-1137. https://doi.org/10.1016/S0016-7037(01)00853-5.
107. Roberts, D.R., Ford, R.G., and Sparks, D.L., Kinetics and mechanisms of Zn complexation on metal oxides using EXAFS spectroscopy. *Journal of Colloid and Interface Science*, 2003. **263**(2): p. 364-376. https://doi.org/10.1016/S0021-9797(03)00281-9.
108. Struis, R.P.W.J., et al., Speciation of zinc in municipal solid waste incineration fly ash after heat treatment: an X-ray absorption spectroscopy

study. *Environmental Science & Technology*, 2004. **38**(13): p. 3760. https://doi.org/10.1021/es0346126.

109. Steenari, B.-M. and Noren, K., Speciation of Zinc in ash investigated by X-ray absorption spectroscopy. 2008: Sweden.
110. Ndiba, P.K., Phosphate and thermal stabilization of heavy metals in dredged sediments. 2009.
111. Tang, Y.Z., et al., Zinc incorporation into hydroxylapatite. *Biomaterials*, 2009. **30**(15): p. 2864-2872. https://doi.org/10.1016/j.biomaterials.2009.01.043.
112. Cai, X., et al., Characterization of zinc vapor condensation in fly ash particles using synchrotron X-ray absorption spectroscopy. *Journal of Zhejiang University-Science A*, 2015. **16**(1): p. 70-80. https://doi.org/10.1631/jzus.A1400178.
113. Tiberg, C., Sjöstedt, C., and Karlfeldt Fedje, K., Speciation of Cu and Zn in bottom ash from solid waste incineration studied by XAS, XRD, and geochemical modelling. *Waste Management*, 2021. **119**: p. 389-398. https://doi.org/10.1016/j.wasman.2020.10.023.
114. Ziegler, F., Heavy metal binding in cement-based waste materials: an investigation of the mechanism of zinc sorption to calcium silicate hydrate. 2000, ETH Zurich.
115. Libowitzky, E., et al., Proton disorder in dehydrated hemimorphite-IR spectroscopy and X-ray structure refinement at low and ambient temperatures. *European Journal of Mineralogy*, 1997. **9**(4): p. 803-810.
116. Cassingham, N.J., et al., The structural role of Zn in nuclear waste glasses. *International Journal of Applied Glass Science*, 2011. **2**(4): p. 343-353. https://doi.org/10.1111/j.2041-1294.2011.00067.x.

Appendix B Techniques for Waste Characterisation

B.1 Techniques for Elemental Analysis

B.1.1 Atomic Absorption Spectrometry

The basic principle of AAS is to vaporise ground-state analyte atoms into gas and the free atoms in the gas state absorb light at a specific, unique wavelength, in which the light intensity before and after passing through the sample is measured by a detector. F-AAS and GF-AAS are the two main types of atomisers. GF-AAS, which operates at higher temperature with a longer residence time of the atomised analyte, has several orders of magnitude higher sensitivity than F-AAS [115].

AAS requires liquid samples; therefore, solid samples must undergo a wet chemical preparation procedure to dissolve analytes. Total acid digestion (TAD) procedures involve heating samples with mixtures of HNO_3, H_2O_2, $HClO_4$, HF and HCl [116]. The type of digestion should be chosen depending on the sample matrix. Aqua regia [117], a mixture of HNO_3 and HCl, is often used because of laboratory safety concern with use of HF, but cannot digest some aluminosilicate minerals, so elements present in these minerals will not be included in the measurement.

B.1.2 Inductively Coupled Plasma

The basic principle of ICP is to ionise the sample by an extremely hot plasma, usually made from argon (Ar) gas. The ICP can be combined with an OES for major and minor element analysis, or with MS for trace element analysis. The main difference between ICP-OES and ICP-MS is how the ions are generated and detected. When ICP is combined with an optical emission spectrometer, the ionised elements emit electromagnetic radiation at characteristic wavelengths, which are measured by a detector. When ICP is combined with a mass spectrometer, the ionised elements are separated based on their mass-to-charge ratio, and converted into an electrical signal by an ion detector, which is multiplied and read by computer software [118]. ICP also requires liquid samples; therefore, solid samples must also undergo TAD or aqua regia (B.1.1). The advanced LA-ICP-MS begins with a laser beam focused on the sample surface to generate fine particles-a process known as Laser Ablation. The ablated particles are then transported to the secondary excitation source of the ICP-MS instrument for digestion and ionisation of the sampled mass. The excited ions in the plasma torch are subsequently introduced to a mass spectrometer detector for both elemental and isotopic analysis [119].

B.1.3 X-ray Fluorescence Spectroscopy

XRF measures emission of characteristic fluorescent light by analytes in response to bombardment by X-rays (Figure B1). When X-rays pass through an atom, an electron can be ejected from its atomic orbital (Figure B1b) at a lower level after the atom absorbs a certain amount of X-ray wave (photon) (Figure B1a). The electron from a higher-energy-level orbital can be transferred to the lower-energy-level orbital. A photon (fluorescent light) may be emitted during the transition (Figure B1c), which equals to the energy difference between the two orbitals. XRF is suitable for solids, liquids and powders. By convention, element concentrations are reported as oxides, though they usually have a more complex speciation.

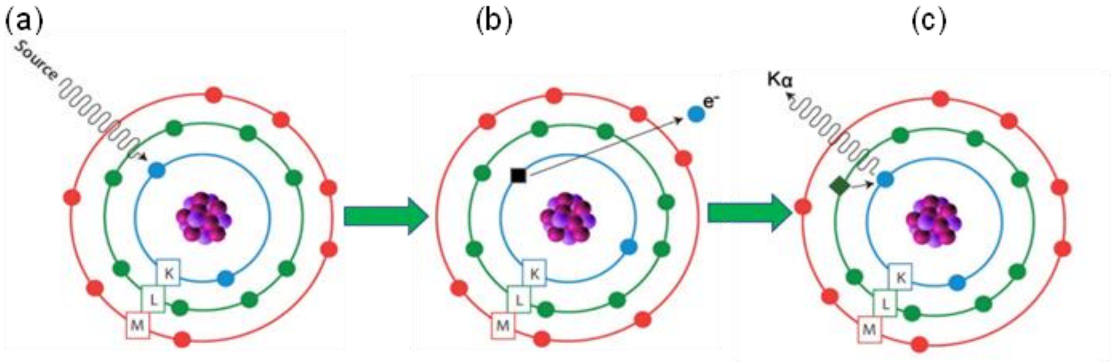

Figure B1 Schematic diagram of X-ray fluorescence.

B.2 Techniques for Phase Identification and Quantification

B.2.1 Sequential Chemical Extraction

Sequential chemical extraction uses progressively more aggressive reagents to digest the solid phases in a sample. The results of spectrometric analysis, such as AAS, of the digestates are used to speculate about the ‘operational speciation’ of elements based on their partitioning in the different fractions. The Tessier and Community Bureau of Reference (BCR) schemes are the most widely applied [120-122]. The basic method has been adapted by many different authors, but the fractions are generally, in order of decreasing mobility: water soluble, ion-exchangeable, carbonates, associated with Fe-Mn oxides, bound to organic matter, and residuals. Apart from the difficulty of assigning element speciation on the basis of such broad reactivity bands, the technique has also been shown to have poor reproducibility [123].

B.2.2 X-ray Diffraction

XRD is based on the constructive interference of monochromatic X-rays and a crystalline sample [124]. When an incident X-ray beam pass through a sample, the X-rays get diffracted. Most of the diffracted X-rays destructively interfere with each other and cancel each other out. The diffracted X-ray beams interfere constructively and reinforced one another, shown in

Figure B2, when the wavelength of X-rays is similar to the inter-atomic spacing in the crystals of the sample. The conditions for constructive diffraction should satisfy the Bragg's equation (Eq.(B1)). Those reinforced diffracted X-rays produce the diffraction pattern that is compared with reference patterns to identify the crystal structure.

$$\mathrm{N}\lambda\ = 2\mathrm{d}\ \sin\theta \tag{B1}$$

Where N is an integer number, λ is the wavelength of the radiation, d is the distance of the lattice planes for which the peak occurs, and θ is the angle between the lattice planes and the incident beam.

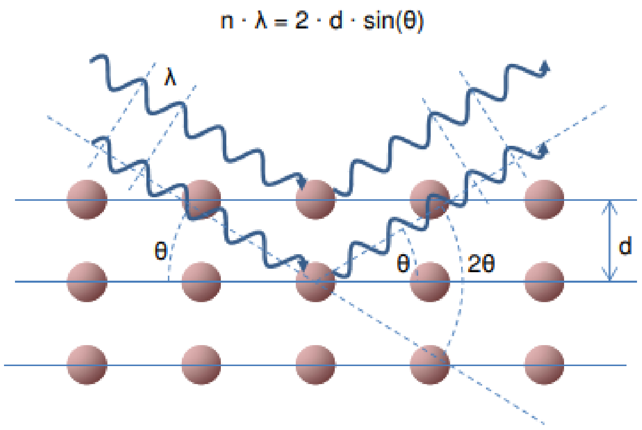

Figure B2 Schematic diagram of constructive interference in X-ray diffraction [124].

Rietveld refinement, as the most common XRD refinement, uses a least square approach to refine a theoretical diffraction pattern to a measured diffraction pattern of a sample [125]. This refinement method is used to semi-quantify the crystal phases. The least square differences between the simulated diffraction pattern and the experimental one is expressed as Bragg's R_{wp}.

B.2.3 Optical Microscopy

OM uses visible light and a system of lenses to enable magnified observation of small samples. Light may be reflected from the surface of a sample, or transmitted through a thin-section. Images of magnified samples can be captured by normal light-sensitive cameras. This technique is appliable for solids, and non-destructive. However, the resolution of the optical microscope is limited to 0.2 micrometers with a practical magnification limit of 1000x. Also, it requires considerable experience and expertise to identify crystalline and amorphous features [126].

B.2.4 Scanning Electron Microscopy

SEM can produce highly magnified images by using electrons instead of light to form an image. SEM can be used to identify the physical form (morphology of crystalline and amorphous phases), size and distribution of phases. EDS is used to identify elements; it has a similar basis as XRF, but is not usually quantitative, since it is not calibrated against a standard. Together, information about morphology and elemental composition may be used to postulate phases. Automated image analysis of SEM photomicrographs informed by EDS, can then be used to quantify the postulated phases (i.e., automated mineralogy, e.g., QEMSCAN). However, they cannot discriminate between minerals with similar EDS spectra (e.g., hemimorphite/willemite) [127] and the detection limit for bulk mineralogy is about 3% [128]. Since the areas examined are very small, numerous analyses are necessary to ensure that they are representative of the whole material.

B.2.5 Mössbauer Spectroscopy

Mössbauer spectroscopy is a spectroscopic technique based on the Mössbauer effect, namely, it probes the recoilless emission and resonant absorption of gamma rays by nuclei [129]. The energy levels of the nuclei are sensitive to the electrostatic and magnetic fields present at the nuclei and thus to changes in chemical bonding, valence (i.e., the oxidation state of an atom), and magnetic ordering. Therefore, Mössbauer spectroscopy is used to detect oxidation state and the magnetic state of the sample. Basically, a beam of gamma radiation goes through the solid sample, and a detector measures the intensity of the beam transmitted through the sample. The atoms in the source emitting the gamma rays must be of the same isotope as the atoms in the sample absorbing them. However, only a few nuclei exhibit the Mössbauer effect, e.g., ^{57}Fe, ^{119}Sn, ^{121}Sb, ^{153}Eu, and ^{197}Au , and the great majority of applications in Earth science (and in general) are with ^{57}Fe [130].

B.2.6 X-ray Photoelectron Spectroscopy

XPS is the simultaneous measurement of kinetic energy and number of electrons escaping when the sample is irradiated with a beam of X-ray radiation under high vacuum. It is a spectroscopic method capable of examining the surface (5 nm) of a material with detection limits of 0.1-1.0% [131]. It quantifies elemental compositions and identifies their oxidation state, nearest neighbour chemical bonding, density of the electronic state, and the overall electronic structure.

B.2.7 Fourier-transform Infrared Spectroscopy

Fourier-transform infrared spectroscopy (FTIR) uses infrared light to measure the chemical bonds in a molecule by producing an infrared absorption spectrum. This technique is applicable for a solid, liquid or gas, and used to identify organic, polymeric, and, in some cases, inorganic materials, and. Only specific inorganic species exhibit an FTIR spectrum, e.g., silicates, carbonates, nitrates and sulfate [132].

Reference

1. Smith, D.R. and Nordberg, M., Chapter 2 - General Chemistry, Sampling, Analytical Methods, and Speciation∗. Handbook on the Toxicology of Metals (Fourth Edition), ed. G.F. Nordberg, B.A. Fowler, and M. Nordberg. 2015, *San Diego*: *Academic Press*. 15-44.
2. Arsenic, A.M., et al., Method 3050B acid digestion of sediments, sludges, and soils 1.0 scope and application. *Washington, DC, USA*, 1996.
3. Technical Committee ISO/TC 190, S.q., Soil quality: Extraction of trace elements soluble in aqua regia. 1995: *International Organization for Standardization*.
4. Thomas, R., Practical guide to ICP-MS: a tutorial for beginners. 2008: *CRC press*.
5. Tessier, A., Campbell, P.G., and Bisson, M., Sequential extraction procedure for the speciation of particulate trace metals. *Analytical chemistry*, 1979. **51**(7): p. 844-851.
6. Ure, A., et al., Improvements in the determination of extractable contents of trace metals in soil sediment prior to certification. 1993, Commission of the European Communities—BCR Information.
7. Bacon, J.R. and Davidson, C.M., Is there a future for sequential chemical extraction? *Analyst*, 2008. **133**(1): p. 25-46. https://doi.org/10.1039/B711896A.
8. Stegemann, J.A. and Cote, P.L., Summary of an investigation of test methods for solidified waste evaluation. *Waste management*, 1990. **10**(1): p. 41-52.
9. Stanjek, H. and Häusler, W., Basics of X-ray Diffraction. *Hyperfine Interactions*, 2004. **154**(1): p. 107-119. https://doi.org/10.1023/B:HYPE.0000032028.60546.38.
10. Rietveld, H.M., A profile refinement method for nuclear and magnetic structures. *Journal of applied Crystallography*, 1969. **2**(2): p. 65-71.
11. Ager III, J.W. Overview of optical microscopy and optical microspectroscopy. in *AIP Conference Proceedings*. 1998. American Institute of Physics.
12. Santoro, L., et al., Mineralogical characterization of the Hakkari nonsulfide Zn(Pb) deposit (Turkey): The benefits of QEMSCAN®. *Minerals Engineering*, 2014. **69**: p. 29-39. https://doi.org/10.1016/j.mineng.2014.07.002.
13. Rollinson, G.K., et al., Characterisation of non-sulphide zinc deposits using QEMSCAN®. *Minerals Engineering*, 2011. **24**(8): p. 778-787. https://doi.org/doi.org/10.1016/j.mineng.2011.02.004.
14. Mössbauer, R.L., Kernresonanzfluoreszenz von gammastrahlung in Ir 191. *Zeitschrift für Physik*, 1958. **151**: p. 124-143.
15. Gütlich, P., Schröder, C., and Schünemann, V., Mössbauer spectroscopy—an indispensable tool in solid state research. *Spectroscopy Europe*, 2012. **24**(4): p. 21.

Appendix C Data Reduction for X-ray Absorption Spectroscopy

C.1 Calibration/Alignment/Merging/Choosing E_0

Data reduction is applied before fitting. The standard processes mainly compose of alignment, merging, calibration, normalisation, background removal, converting E to k, and Fourier transform.

Data calibration is to choose the first peak of the first derivative spectra of references as the edge energy E_0 and then assign it to a tabulated value, e.g., 9659.0 eV for Zn. After calibration, scans on a sample measured under identical conditions are merged. This reduces the systematic errors, including sample inhomogeneity, beam damage, thickness and particle size effects, harmonics, nonlinear detectors, glitches, sample alignment issues, and errors in normalisation. The edge energy E_0 of each sample spectrum is selected as the first peak of its first derivative spectrum in this study.

C.2 Data Normalisation and Background Removal

(1) Normalisation process enables the data to be independent from sample thickness, sample preparation, absorber concentration, detector, and amplifier settings. Normalisation of a ZnO standard sample is shown in Figure C1. An edge step normalised spectrum: normalised by dividing all the y-values by the edge step ($\Delta\mu_0$) to get the absorption from 1 X-ray and then subtracting a regressed line determined by the pre-edge region. The $\Delta\mu_0$ is the change in the spectrum without fine structures at the edge energy E_0. Therefore, it is decided by designing a pre-edge (green line in Figure C1), a post-edge range (purple line Figure C1), and edge energy (E_0) [133].

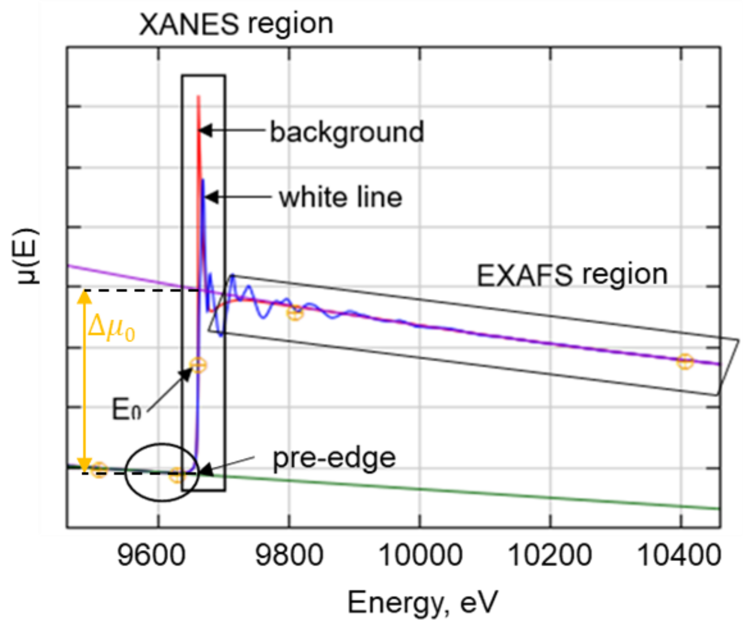

Figure C1 Zn K-edge X-ray absorption spectrum of ZnO with X-ray Absorption Near Edge Structure region and Extended X-ray Absorption Fine Structure region.

(2) Removing a smooth post-edge background to approximate $\mu_0(E)$ to isolate the XAFS (χ(E)) by designing R_{bkg} and spline range in E.

$$\chi(E) = \frac{\mu(E) - \mu_0(E)}{\Delta\mu(E)} \tag{A1}$$

Where $\mu_0(E)$ refers to absorption from an isolated atom of interest. It is approximated with a smooth spline, representing only very-low-frequency components.

C.3 Converting from E to k

(1) Then use wavevector $k = \frac{\sqrt{2m(E-E_0)}}{\hbar}$ to convert χ(E) to χ(k),

$$\chi(k) = \sum_j \frac{N_j S_0^2 f_j(k) \cdot e^{-2R_j/\lambda(k)} e^{-2k^2\sigma_j^2}}{kR_j^2} \sin\left[2kR_j + \delta_j(k)\right] \tag{A2}$$

Where scattering amplitude f(k) and phase-shift δ(k) means photo-electron scattering properties of the neighbour atom, depending on atomic number Z of the scattering atom; $\delta(k)$ is an element-specific phase shift that causes the Fourier Transform distance to be smaller by 0.2-0.5 Å from the true value. R is the distance to neighboring atom; N is the coordination number of a neighbour atom; σ^2 refers to mean-square disorders of neighbour distance; λ is mean-free-path, depending on k (λ <25 Å for EXAFS k-range).

(2) Since EXAFS is decaying quickly with k, χ(k) is multiplied by a power of k, such as k^2 or k^3, to emphasise the oscillation. The phenomenon of decay is attributed to the collision of the wave path with an intermediate atom, or even more, losing energy, before the wave is reverted to the absorbing atoms. An example of EXAFS (k-space) of ZnO is shown with k^2 weight in top right of Figure C2.

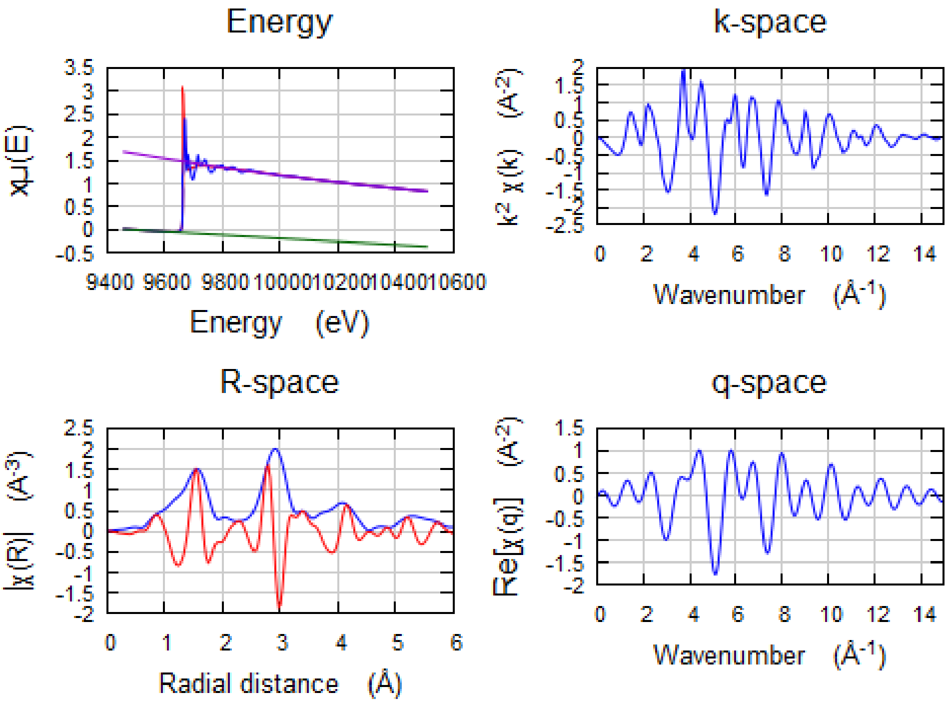

Figure C2 XAS spectrum of ZnO. (top left) Normalised XAS spectrum; (top right) EXAFS spectrum; (bottom left) Fourier Transform; (bottom right) Back Fourier Transform.

C.4 Fourier Transform Spectra

Different near-neighbour coordination spheres lead to various frequencies in the oscillation. The χ(k) functions are Fourier transformed to Fourier transform spectrum which reflects the different oscillation patterns in χ(k) via selecting k-range and R_{bkg}. An example of Fourier Transform of ZnO is shown in bottom left of Figure C2. R_{bkg} should be about half the R value for the first peak. Data in Fourier Transform should be smooth, not pinched. If not, R_{bkg} may be too large. Small values for R_{bkg} result in significant signals at low R values, where no neighboring atoms are present. Large values cause the removal of signals from the first shell signal. The choice of k range can be modified by this criterion. That is, small changes in R_{bkg} can be used to determine the minimum k-value (k_{min}) to use in the Fourier transform since EXAFS signal should not depend on R_{bkg}.

As the scattering atom becomes heavier, scattering amplitude increases, and scattering envelope peaks at higher k. Thus, heavy atoms are easier to observe, especially at longer distances (top left of Figure C3). As the number of scattering atoms increases, scattering amplitude increases, but frequency is unchanged, and so is Fourier transform (top right of Figure C3). For the same scattering atom, scattering amplitude decreases and frequency increases when the scattering atom moves farther away from the absorber (bottom left of Figure C3). As temperature increases, the Debye-Waller factor (σ_j^2) goes up, leading to the decrease of EXAFS intensity and Fourier transform intensity (bottom right of Figure C3).

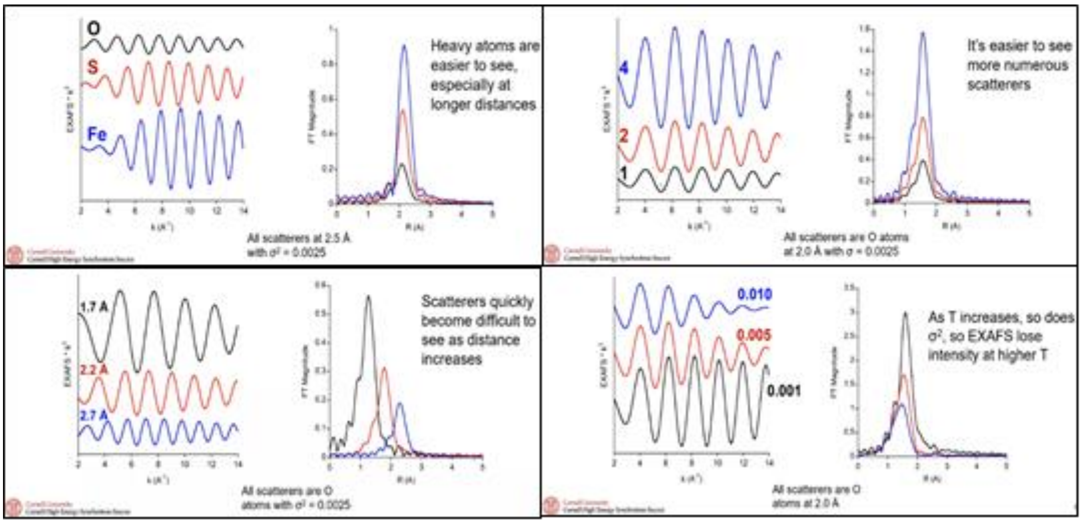

Figure C3 Relationship of fitting parameters and EXAFS and Fourier transform [134].

Reference

1. Calvin, S., XAFS for Everyone. 2013: *CRC press*.
2. Pollock, C. *Introduction to Extended X-Ray Absorption Fina Structure (EXAFS)*. [Youtube] 2020 27 05 2020 [cited 2020 25 12]; Available from: https://www.youtube.com/watch?v=gh_1vGVluLA.

Appendix C

Appendix D Chemical Compositions in the Three Wastes from Literature

See excel document for Appendix D.

Appendix D

Appendix E Methods and Results of Standard Characterisation for the Three Wastes

E.1 Methods of Standard Characterisation for the Three Wastes

E.1.1 Elemental Concentrations of the Waste by X-ray Fluorescence

The subsamples were ground for analysis using a micronizing mill. Total element compositions of the waste was determined by powder X-ray fluorescence (XRF) spectrometry using the Spectro X-LAB Pro 2000. Loose powder method was undertaken because of limited sample and being recoverable [135]. A small portion of sample was pulverized by grinding it in a mortar agate with a mortar pestle using to reduce voids and increase the homogeneity, before passing through a 63μm sieve. The prepared sample was then collected in the sample cell (Figure E1a) where the loose powder sample is above the sample film attached to the bottom of the sample cell. The sample should be adequate to reach the infinite thickness that allows all primary X-ray beam emitted from an XRF instrument. After the sample was loaded in the sample cell, a lid (Figure E1b) was used to cover the sample to prevent contamination of sample chamber by the sample. Great attention should also be paid not to break the film during transferring and measurement to prevent contamination. The prepared sample was set up in XRF spectrometer, and ran for the tests. Each of sample took approximately 30 minutes. Compared to pressed powder method, two major disadvantages are present in loose powder method. One is the lower reproducibility of sample preparation. Another is the poor sensitivities for light elements (e.g., B-F) due to the decrease of the X-ray intensity caused by the sample film covering analysis surface. The XRF is a reliable analysis for bulk elements, but less reliable for trace elements. The result should be treated as semi-quantitative.

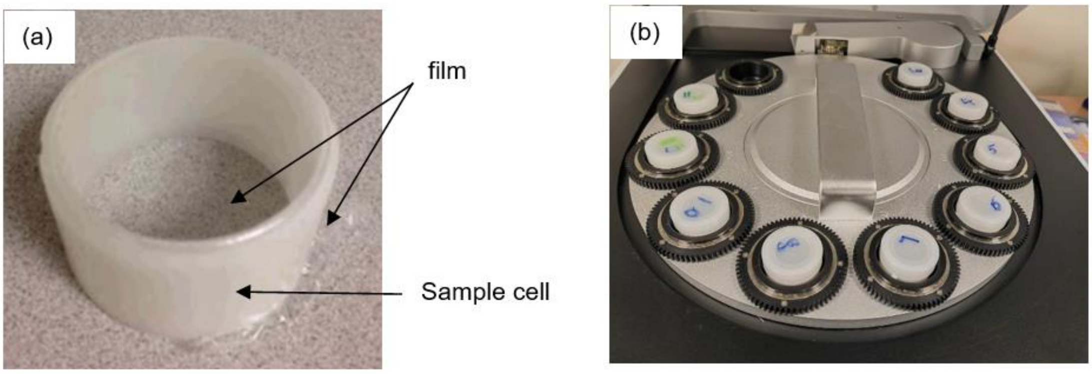

Figure E1 Sample preparation for X-ray Fluorescence using loose powder method.

E.1.2 Mineralogy of the Three Wastes by X-ray Powder Diffraction

X-ray powder diffraction (XRD) analysis was used to characterize the crystalline phases present in the waste. Powdered XRD samples were prepared by grinding using a mortar agate and mortar pestle, before passing a 63μm sieve. The sample ideally should be between 1-44μm [136]. Undergrinding sample could cause a decrease in intensity of peaks, while overgrinding may result in misidentified phases and/or inaccurate crystallite size [136].

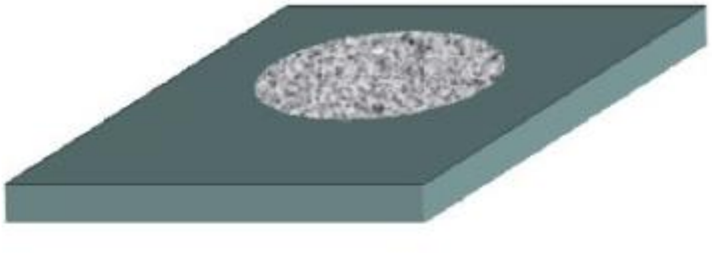

Figure E2 Sample preparation for X-ray Diffraction [137].

Each sample was side-loaded against a ground-glass surface into a glass-backed aluminium-framed sample holder (Figure E2). Diffraction patterns were measured in Bragg–Brentano reflection geometry using a Bruker D8 advance. This diffractometer is equipped with a Cu anode X-ray tube (run at 40 kV, 250 mA) and an incident beam Ni monochromator, which produces a single CuKa1 line, leading to very sharp diffraction maxima. All patterns were scanned with step length 0.02° and scan speed 8°/min. Phase identification was made by search matching to the International Centre for Diffraction Data (ICDD) database using the PAN analytical proprietary software (‘‘X’Pert HighScore Plus’’). Phases were identified on the basis of a minimum of 3 diffraction lines. However, the sample is not recoverable.

E.1.3 Morphology of the Three Wastes by Scanning Electron Microscopy

The morphology of the particles from the waste was investigated by scanning electron microscopy (SEM) at different magnifications on a JEOL JSM-6480LV high-performance, variable pressure analytical scanning electron microscope with secondary electron imaging (SEI) and backscattered electron imaging (BEI) detectors, and energy dispersive x-ray spectroscopy (EDS) with an accelerating voltage of 20 keV. Individual particles from the waste, compacted and polished samples were mounted rigidly on a specimen stub and coated with an ultrathin layer of carbon (graphite). The size of areas and their relevant spot numbers are shown in Table E1,

Table E2 and Figure E3. Certified standards were used for calibration. Element detection limits were reduced to about 0.1-0.05 mass % by using long counting times. Element peaks were automatically identified in the EDS spectrum using AutoID, which also provided tools for manual validation of the elements detected. Summation of the determined elemental compositions to 100% was verified. The EDS analysis should be considered to be semi-quantitative.

Table E1 Summarised size of images and spots for each image for scanning electron microscopy - energy dispersive spectroscopy of filter cakes TX and ST

Number	Size of area	spots	Number	Size of area	spots
TX1	900um	6	ST1	2mm	5
TX2	60um	5	ST2	900um	10
TX3	10um	9	ST3	300um	8
TX4	2mm	4	ST4	40um	9
TX5	300um	6	ST5	300mm	3
TX6	10um	6	ST6	60um	10
			ST7	60um	10
			ST8	400um	5

Table E2 Summarised size of images and spots for each image for scanning electron microscopy - energy dispersive spectroscopy of the Pb/Zn smelter slag

Number	Size of area	spots
SS1	2mm	8
SS2	100um	3
SS3	20um	5
SS4	10um	5
SS5	2mm	14
SS6	40um	8
SS7	80um	10
SS8	2mm	8
SS9	30um	9
SS10	2mm	18
SS11	100um	18

Table E3 Summarised size of images and spots for each image for scanning electron microscopy - energy dispersive spectroscopy of the APCR

Number	Size of area	spots
APCR1	60um	9
APCR2	100um	10
APCR3	40um	5
APCR4	40um	9
APCR5	80um	17
APCR6	10um	6
APCR7	40um	11
APCR8	30um	3
APCR9	60um	8
APCR10	80um	10
APCR11	100um	16
APCR12	30um	6
APCR13	40um	3

E.2 Results of Standard Characterisation for the Three Wastes

E.2.1 Elemental Concentrations of the Three Wastes by X-ray Fluorescence

Elemental concentrations of the three wastes, i.e., metal treatment filter cake, Pb/Zn smelter slag, raw and washed air pollution control residue (APCR and WAPCR), were measured previously by XRF, and are presented in Table E4.

Table E4 Total element composition of wastes using X-ray fluorescence (mg/kg dry mass)

Element	TX	ST	SS	APCR	WAPCR
Al, %	0.469	2.42	3.09	2.18	2.66
Ag	64.1	1190	43.1	<1.3	13.6
As	1.7	<8.9	4500	5.5	11
Ba	170	1880	8830	448	830
Br	6.1	5.8	<4.1	532	90.2
Ca, %	34.1	4.2	10.1	33.6	32.8
Cd	2550	84.6	12.9	29.7	44.1
Ce	11	<8.1	11.8	10.9	12.7
Cl, %	0.049	0.335	<0.00087	6.69	0.514
Co	39,7	1770	163	15.8	43.8
Cr, %	1.43	12.6	0.068	0.037	0.045
Cu	1950	13100 .	4770	261	392
Fe, %	2.44	5.43	30.6	0.757	1.19
K, %	<0.0041	0.043	0.307	1.04	0.370
Mg, %	0.609	1.14	1.50	0.784	1.01
Mn, %	0.041	0.68	1.18	0.060	0.086
Mo	20	350	223	<4.0	21
Na, %	<0.037	<0.069	<0.078	<0.13	<0.048
Ni	26600	48100	123	36.4	54.2
P, %	0.296	2.96	0.127	0.366	0340
Pb	128	2070	16200	545	692
S, %	0.416	0.994	1.56	1.20	2.28
513	14.3	13.2	543	198	306
Se	4.8	3.0	8.4	1.9	3.5
Si, %	1.01	0.926	8.83	3.68	5.01
Sn	111	6200	391	163	251
Sr	1640	228	313	477	455
Ti, %	0.086	0.042	0.185	0.673	0.99
Zn	1810	33400	83900	2920	3790
Zr	44.6	108	194	114	173

NA indicates that a parameter was not available.
ST: Filter Cake (Metal treatment sludge from Robert Stuart Ltd, Harlow Essex)
TX: Filter Cake (Metal treatment sludge from South West Metal Finishing, Exeter)
SS — Pb/Zn Smelter slag (St. Modwen Properties PLC, Avonmouth, Bristol)
APCR: Air Pollution Control Residue (SELCHIP, 09/2011)
WAPCR: washed Air Pollution Control Residue (SELCHIP, 09/2011)

Table E5 Concentration of target elements in glasses used in current study and its measurement mode.

	IR-Xglass	Corning glass B	Corning glass C	Darwin glass	GGBFS
Reference	[138]	[139]	[139]	[140]	[141]
Cu		2.13 T			
Fe				1.7 F	
Pb		0.57 F	34.1 T		
S					1.4 F
Zn	0.63 F				

F: refers to flousecence mode; T refers to transmission mode

E.2.2 Mineralogical Compositions of the Three Wastes by X-ray Diffraction

(a) Metal Treatment Filter Cakes

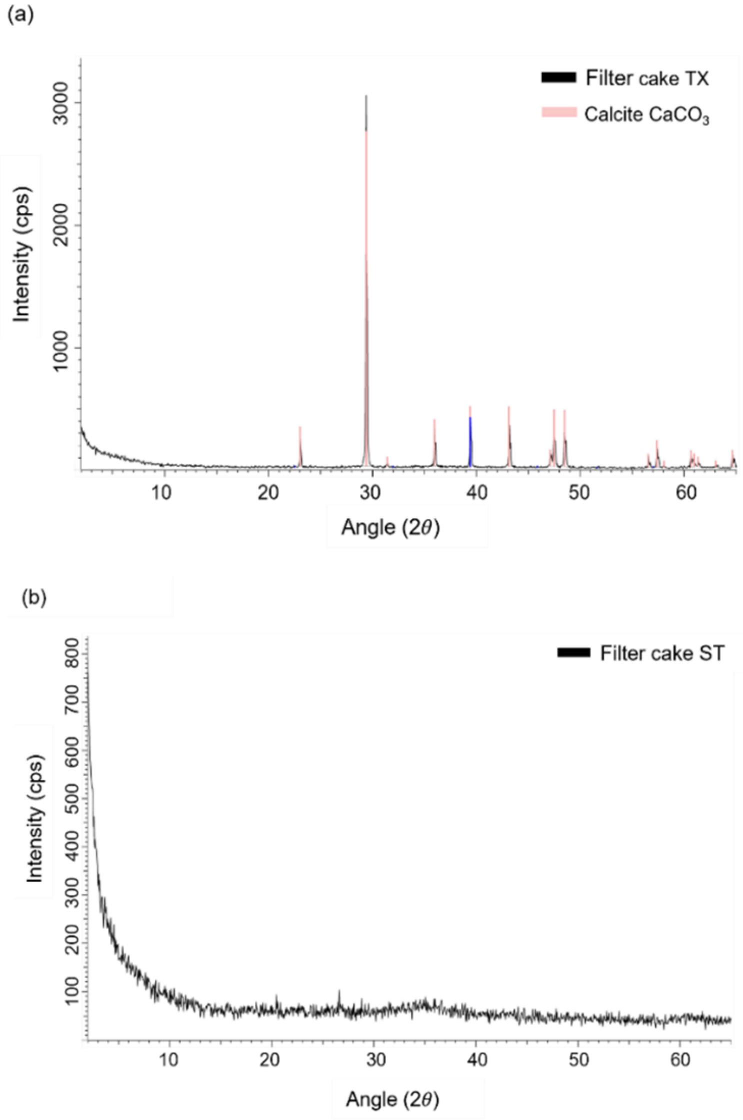

Figure E3 X-ray diffraction (XRD) of the filter cakes TX (a) and ST (b) [142].

In Figure E3, the powder XRD analysis showed that the filter cake ST is complete amorphous material. TX is mainly amorphous material and only calcite ($CaCO_3$) was identified as crystalline phase. The dominant calcite corresponds well to the high content of Ca in filter cake TX. No Cr, Zn, Cu or Pb-bearing compounds were detected by XRD because of the relatively low element concentrations and/or the low crystallinity of both filter cakes [142].

(b) Pb/Zn Smelter Slag

The mineralogical composition of our smelter slag sample determined by XRD is shown in Figure E4. The XRD pattern of the smelter slag shows one major crystalline phase: wüstite ($Fe_{0.925}O$, Crystallographic Open Database 96-900-9772). The peaks are broad and of low intensities, with an average crystallite size for wüstite of 250 Å. A broad hump is observed in the pattern centred at 31.4° 2θ due to the glassy matrix [143]. A few unidentified peaks remain. No Ca or Si-bearing compounds were identified by XRD, indicating that those elements are more likely present in the amorphous matrix of this slag.

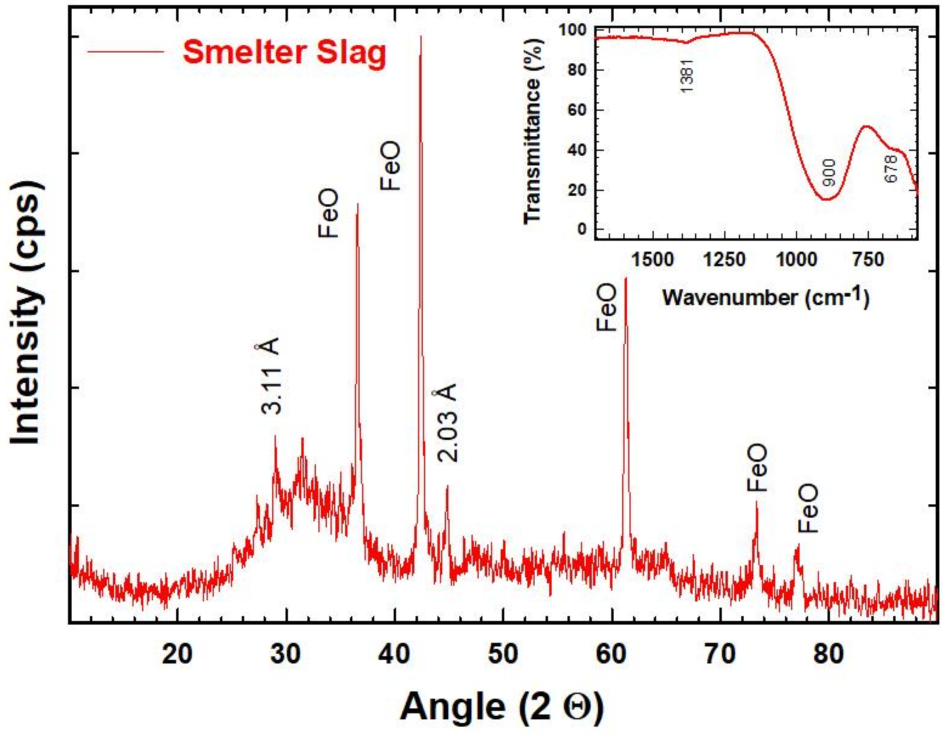

Figure E4 The powder X-ray diffraction (XRD) of the Pb/Zn smelter slag sample with inset Fourier-transform infrared spectroscopy (FTIR) spectrum [144].

(c) Air Pollution Control Residues

The APCR and w-APCR were previously characterised in detail [145, 146]. The main phases identified in the APCR were Ca-bearing phases (i.e., CaClOH, $CaCO_3$, CaO, and $CaSO_4$), SiO_2, Al_2O_3, and soluble salts (i.e., NaCl and KCl). Ca-bearing phases ($CaCO_3$, $CaSO_4{\cdot}2H_2O$, $Ca(OH)_2$), SiO_2, Al-bearing phases (Al_2O_3 and $Al(OH)_3$), and ettringite were identified in w-APCR (Figure E5).

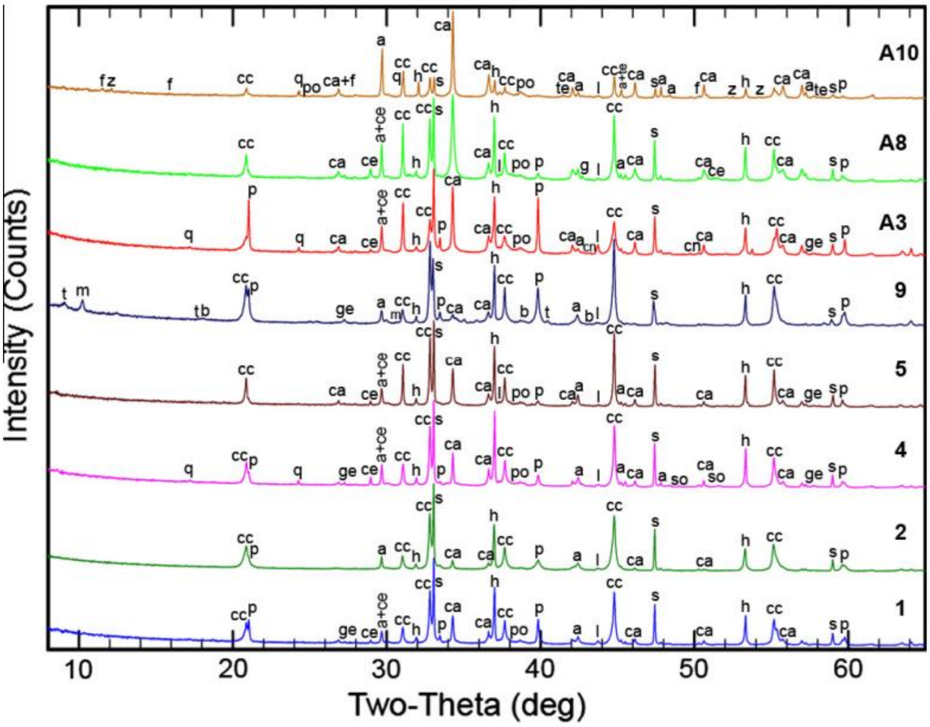

Figure E5 The powder X-ray diffraction (XRD) spectrum of the APCR sample (see A10 for current APCR sample) [145].

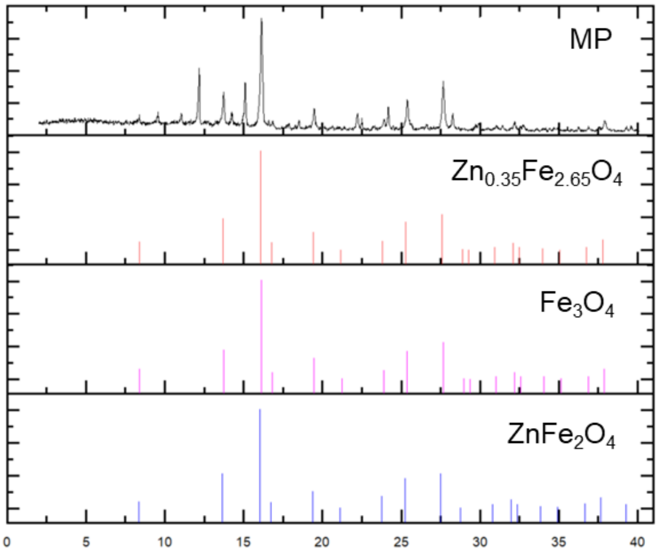

Figure E6 The powder X-ray diffraction (XRD) spectrum of the magnetic fraction sample, compared with $Zn_{0.35}Fe_{2.65}O_4$, Fe_3O_4 and $ZnFe_2O_4$.

E.2.3 Morphology of the Three Wastes by Scanning Electron Microscopy and Energy Dispersive Spectroscopy

(a) Metal Treatment Filter Cakes

The local composition and micromorphology of the investigated filter cakes are quite complex. The dried filter cake easily disintegrated into irregular-shaped agglomerates. For TX, an abundance of calcite crystals (Spectra 1-3) cemented by fine particles that consist of Cr, Fe, Ni, Zn, Cu, Ca, Si, Al, P, S, and Cl (Spectra 4-6) were observed (Figure E7a and b) by SEM-EDS. Mainly irregular-shaped particles containing Cr, Fe, Zn, Cu, Ca, and P with impurities of Mg, Na, Al, Si, S, and Cl (Spectra 7-8 and 10-12), and some Ca carbonate with impurities of some elements, e.g., Zn

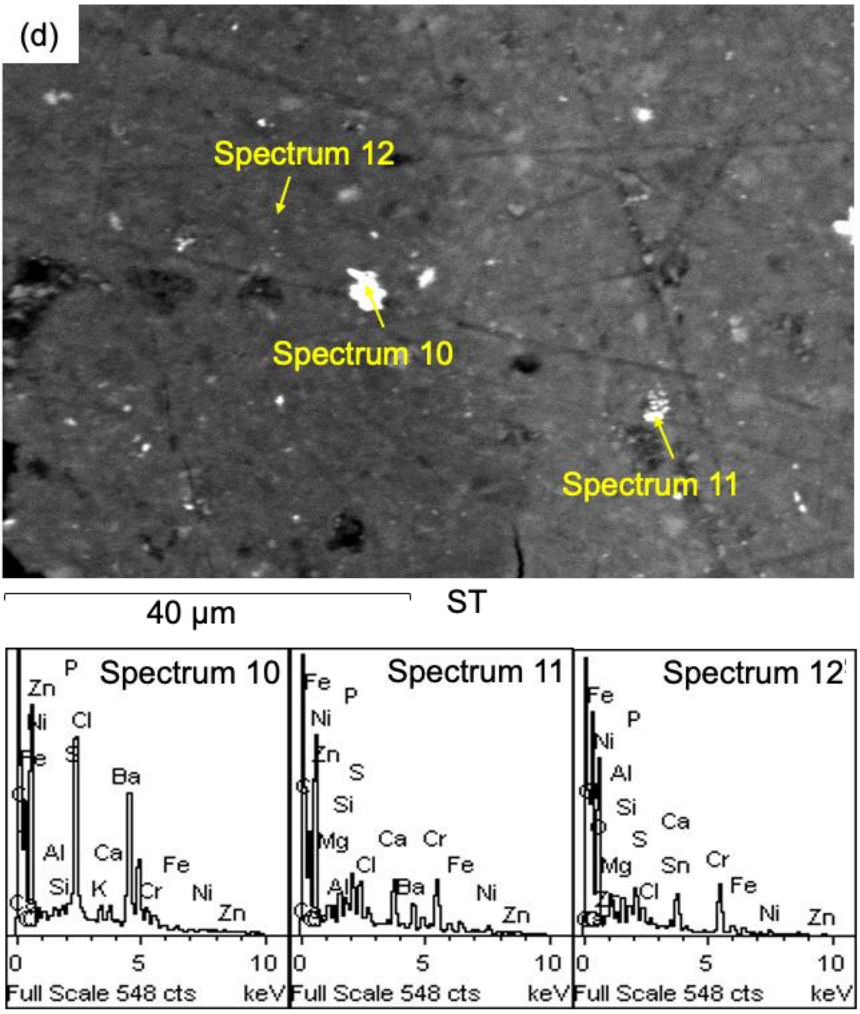

(spectrum 9), were observed in ST (Figure E7c and d).

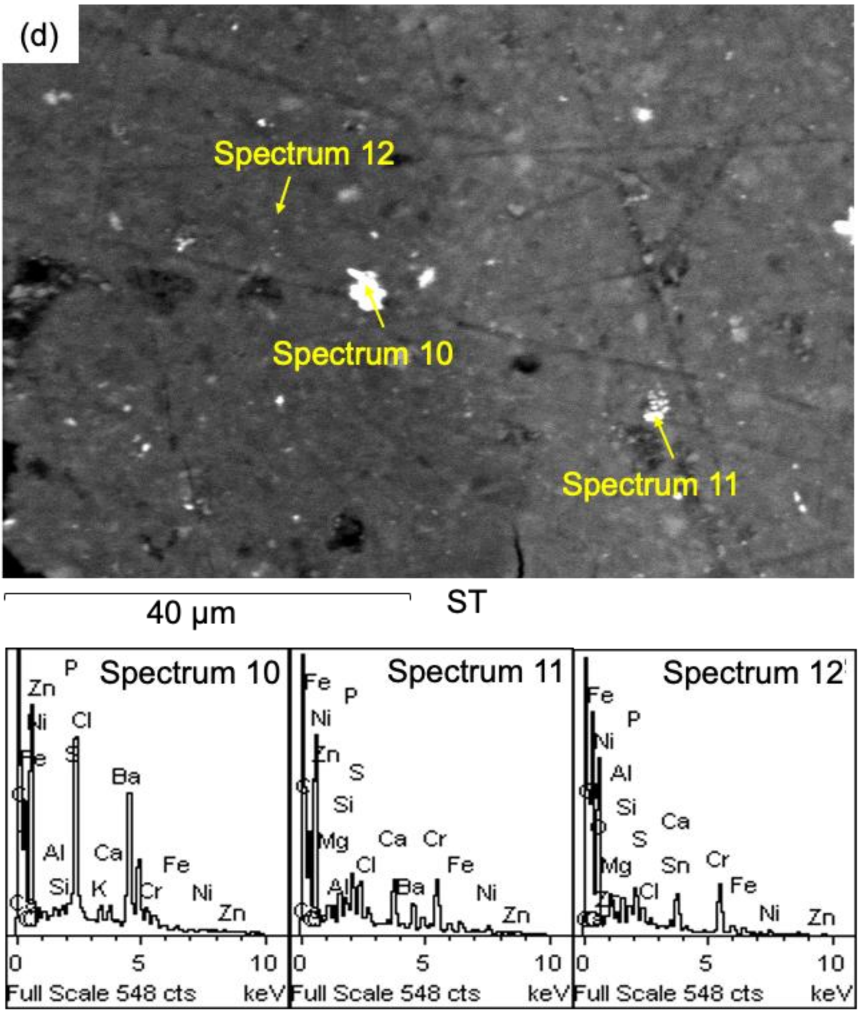

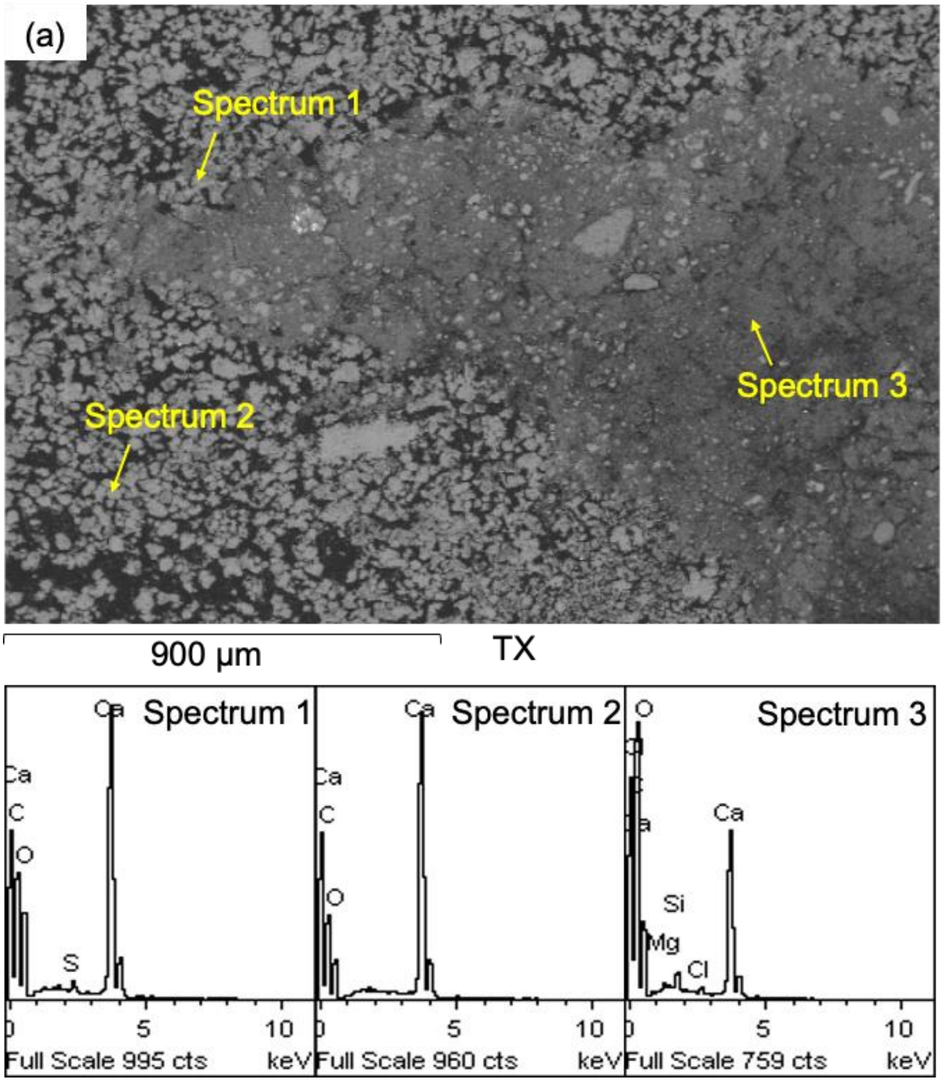

See next page

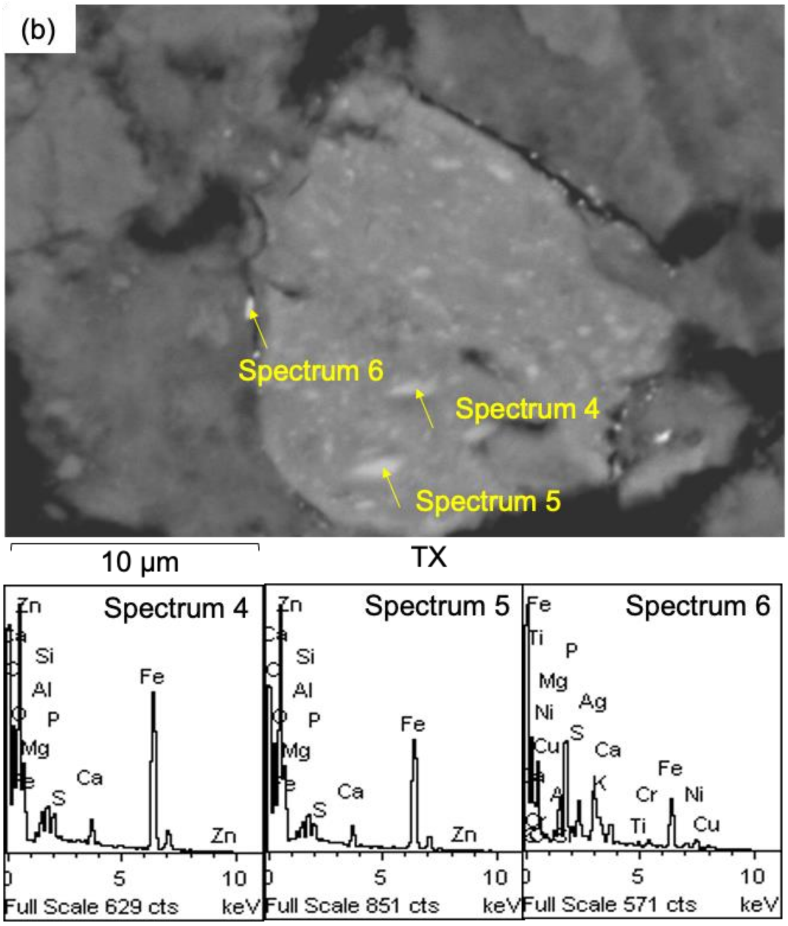
(b)
Spectrum 6
Spectrum 4
Spectrum 5
10 µm
TX
Spectrum 4
Zn
Ca
Si
Al
P
Mg
Fe
Ca
S
Zn
0
5
10
Full Scale 629 cts
keV
Spectrum 5
Zn
Ca
Si
Al
P
Mg
Fe
Ca
S
Zn
0
5
10
Full Scale 851 cts
keV
Spectrum 6
Fe
Ti
P
Mg
Ni
Ag
Cu
S
Ca
Fe
K
Cr
Ni
Ti
Cu
0
5
10
Full Scale 571 cts
keV

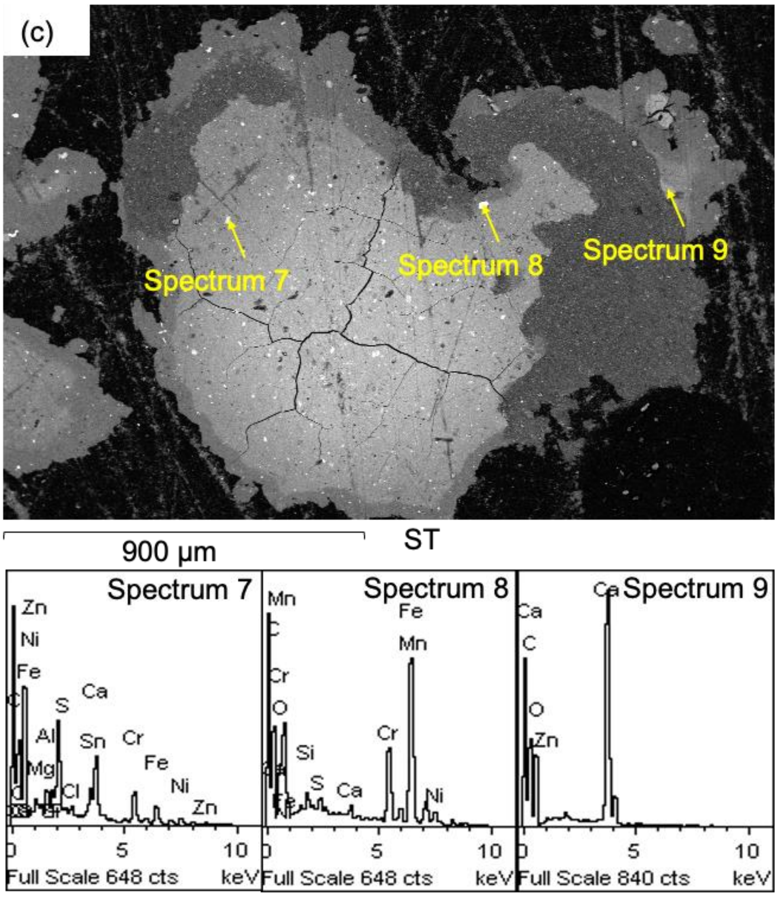
(c)
Spectrum 7
Spectrum 8
Spectrum 9
900 µm
ST
Spectrum 7
Zn
Ni
Fe
C
S
Ca
Al
Sn
Cr
Mg
Fe
Cl
Ni
Zn
0
5
10
Full Scale 648 cts
keV
Spectrum 8
Mn
C
Fe
Mn
Cr
O
Cr
Si
S
Ca
Ni
Fe
0
5
10
Full Scale 648 cts
keV
Spectrum 9
Ca
Ca
C
O
Zn
0
5
10
Full Scale 840 cts
keV

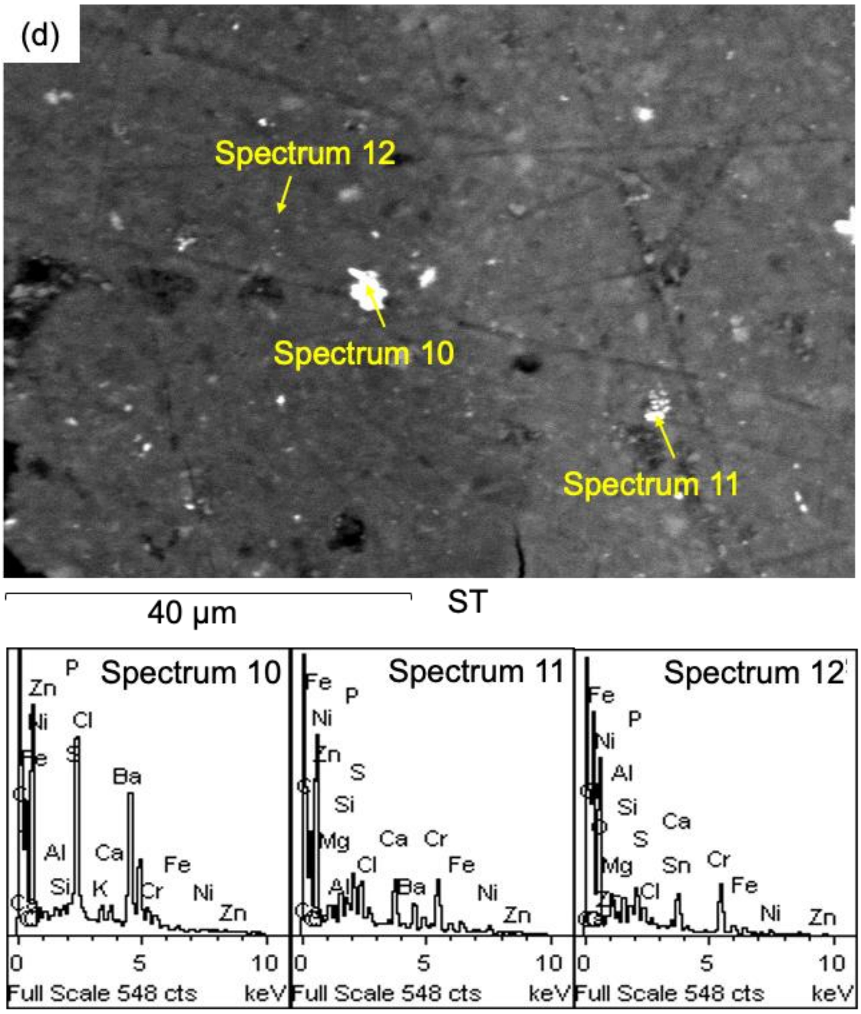

Figure E7 Representative examples of Scanning Electron Microscopy images with Energy Dispersive Spectroscopy analysis of the polished TX (a and b) and ST (c and d)

(b) Pb/Zn Smelter Slag

The SEM/EDS results indicated that our smelter slag sample mainly contains glassy particles consisting of Ca, Fe, Zn, Si, Al, and O with impurities of other elements (e.g., Mg and S) (Spectra 1-4 and 7-10), and inclusions of Pb oxide, carbon, Pb (Spectra 6), Cu oxide with impurities of sulfides with impurities of As, Cu and Sb (Spectra 11-12) (Figure E8). Tiny crystals (about 1µm) of mainly Fe and Zn were also observed in the glassy particles (Spectrum 5).

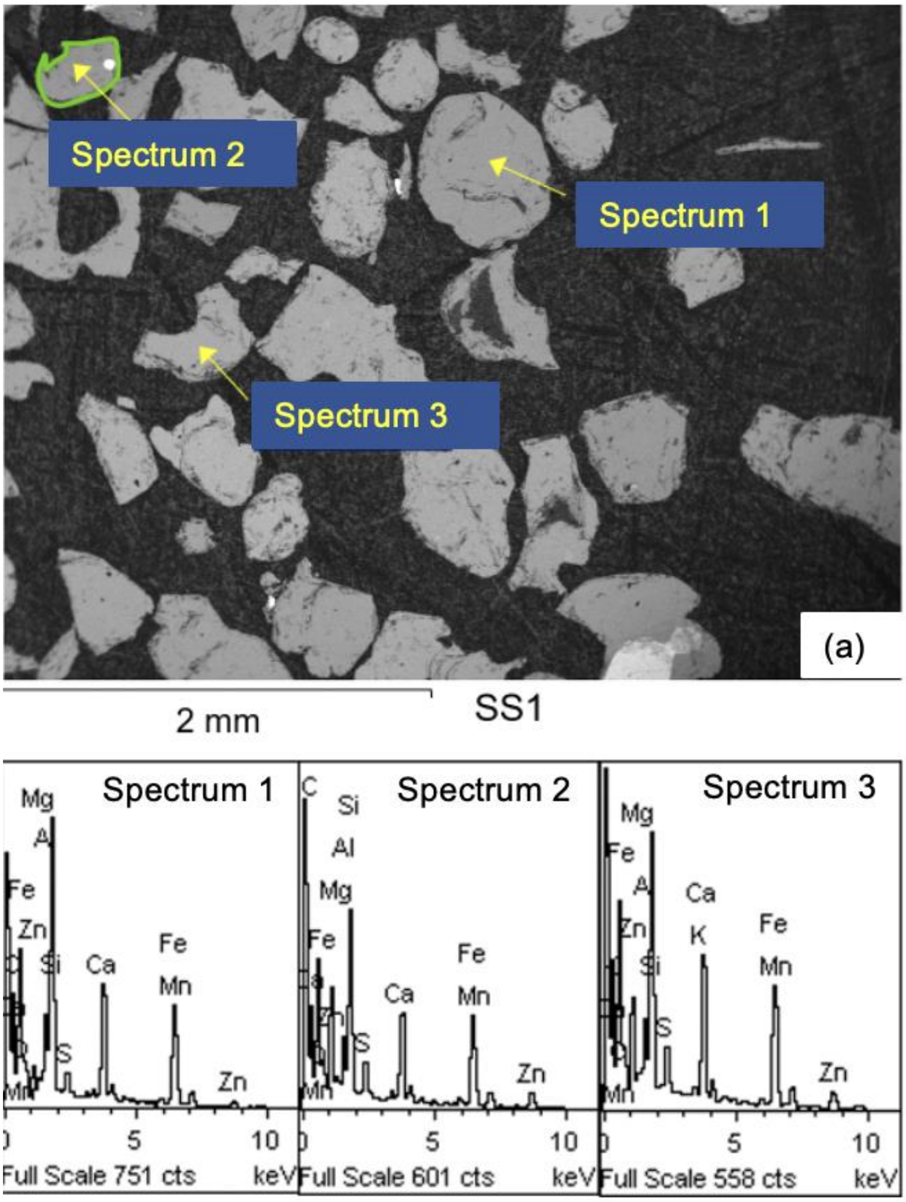

See next page

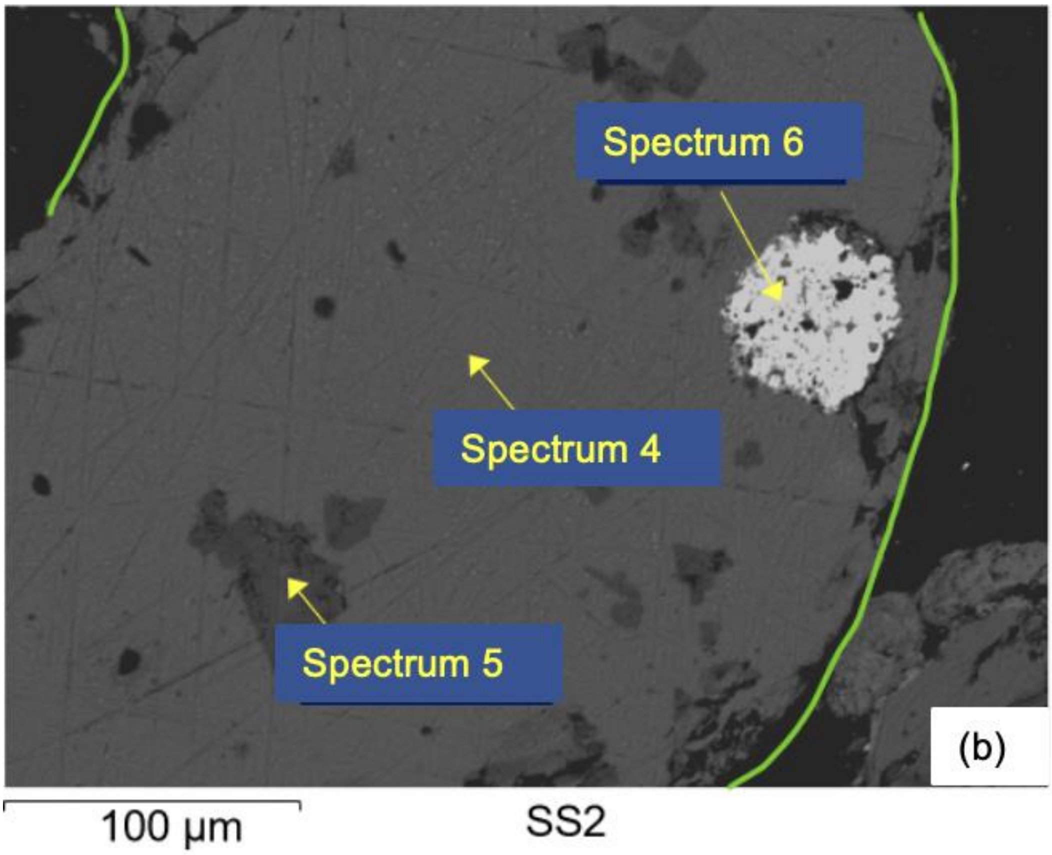

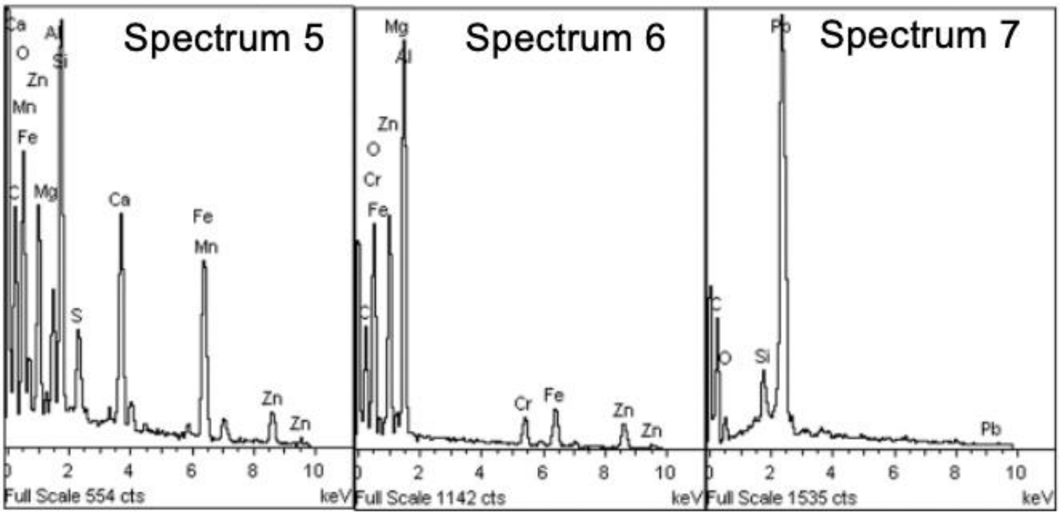

See next page

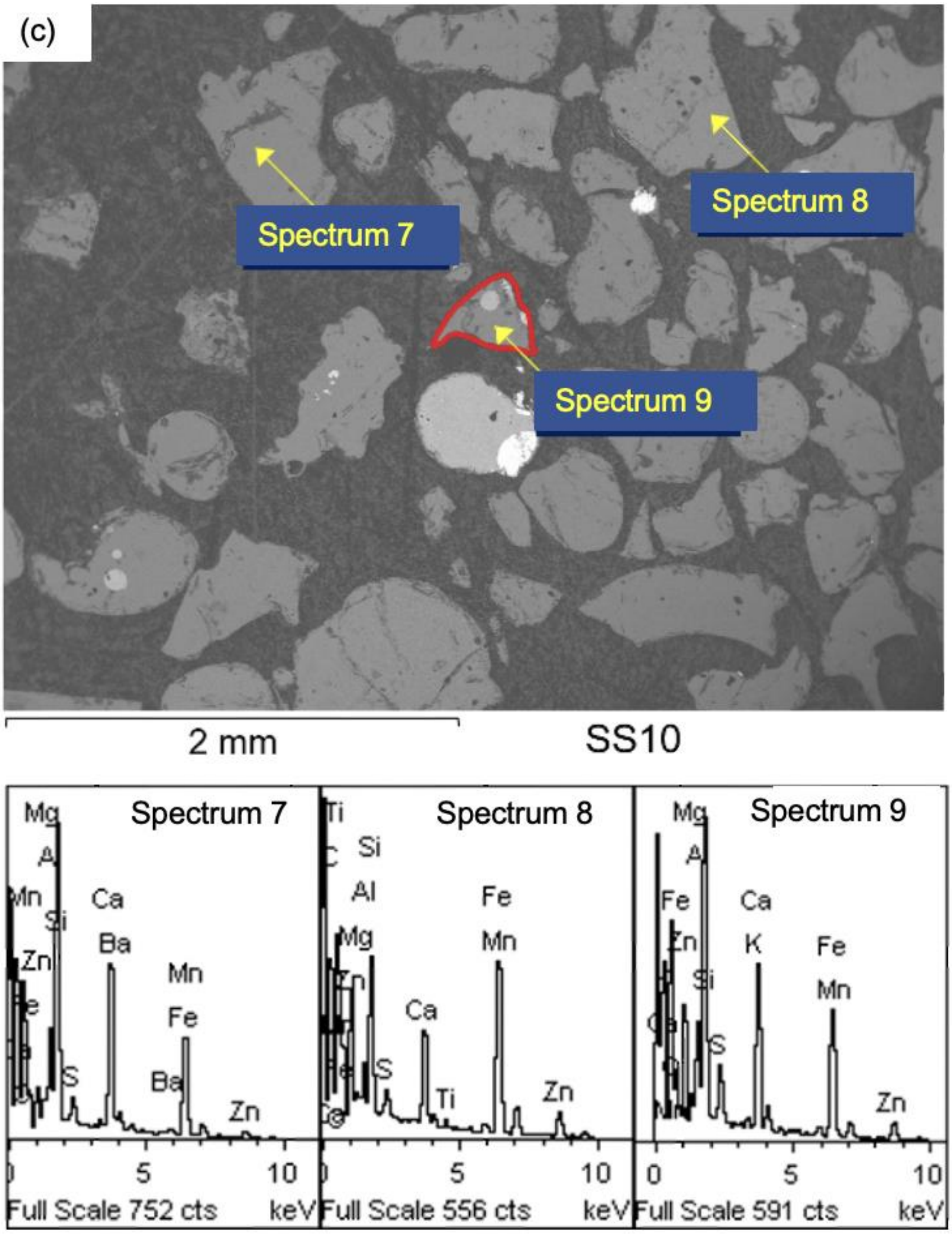

See next page

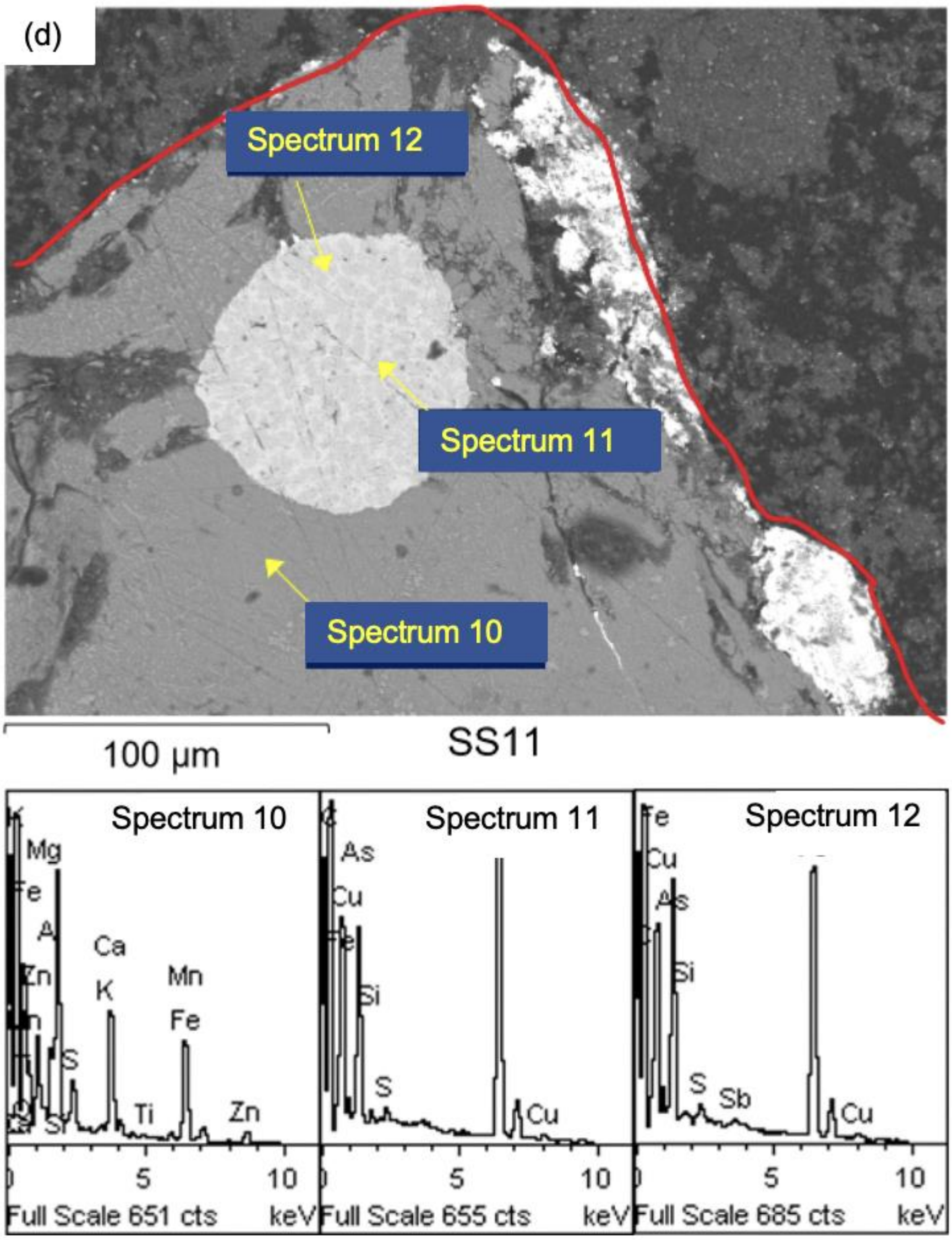

Figure E8 Scanning Electron Microscopy with Energy Dispersive Spectroscopy (SEM-EDS) of the Pb/Zn smelter slag sample.

(c) Air Pollution Control Residues

Both raw and washed APCRs contain aggregates, spherical particles, glassy and fine phases. These samples have plenty of spherical particles of different sizes (10–150 µm). The spherical particles are aluminosilicates with impurities of some elements. A calcium aluminosilicate spherical particle contains impurities of Cl, Fe, Mg, Na, S, Ti, and Zn (spectra 1-3 in Figure E9a), while a spherical particle of calcium silicate containing K, Na and Zn (spectra 4 in Figure E9b). In Figure E9c, cenosphere particles contains high Ca carbonates with impurities of some elements (e.g., Cl, Cu and Zn), with a small portion of aluminosilicates with impurities of some elements (e.g., Cl, Cu and Zn) (see spectra 7-9). The area of APCR, highlighted by green curve in Figure E9c, is zooming in and further investigated in Figure E9d. In Figure E9d, APCR sample also contains unshaped particles, mainly consists of Ca silicates glass and Ca carbonates with impurities of Cl, K, Na, P, S, and Zn (spectra 10-12).

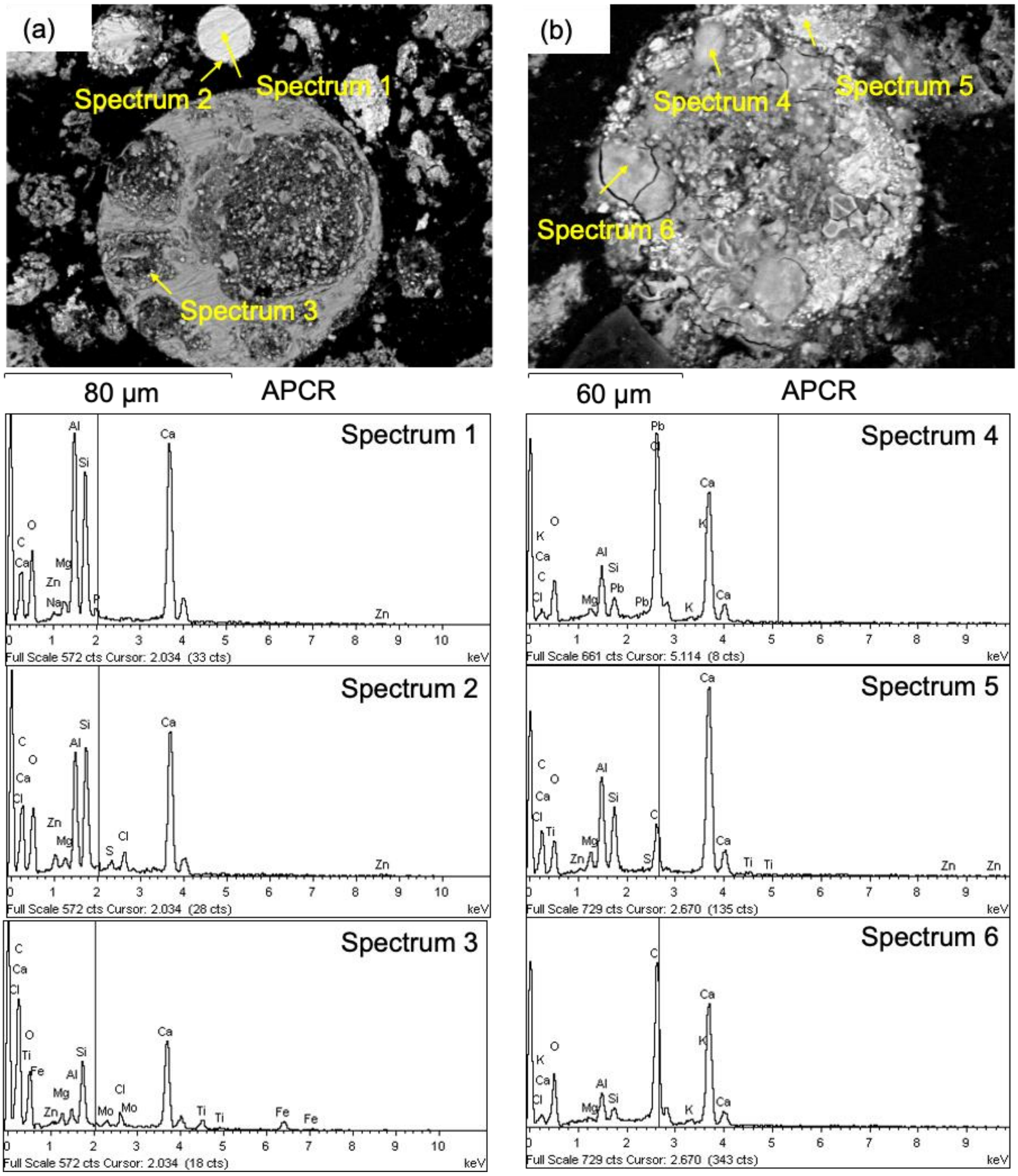
(a)
Spectrum 2
Spectrum 1
Spectrum 3
80 µm
APCR
(b)
Spectrum 4
Spectrum 5
Spectrum 6
60 µm
APCR
Spectrum 1
Full Scale 572 cts Cursor: 2.034 (33 cts)
Spectrum 2
Full Scale 572 cts Cursor: 2.034 (28 cts)
Spectrum 3
Full Scale 572 cts Cursor: 2.034 (18 cts)
Spectrum 4
Full Scale 661 cts Cursor: 5.114 (8 cts)
Spectrum 5
Full Scale 729 cts Cursor: 2.670 (135 cts)
Spectrum 6
Full Scale 729 cts Cursor: 2.670 (343 cts)
keV

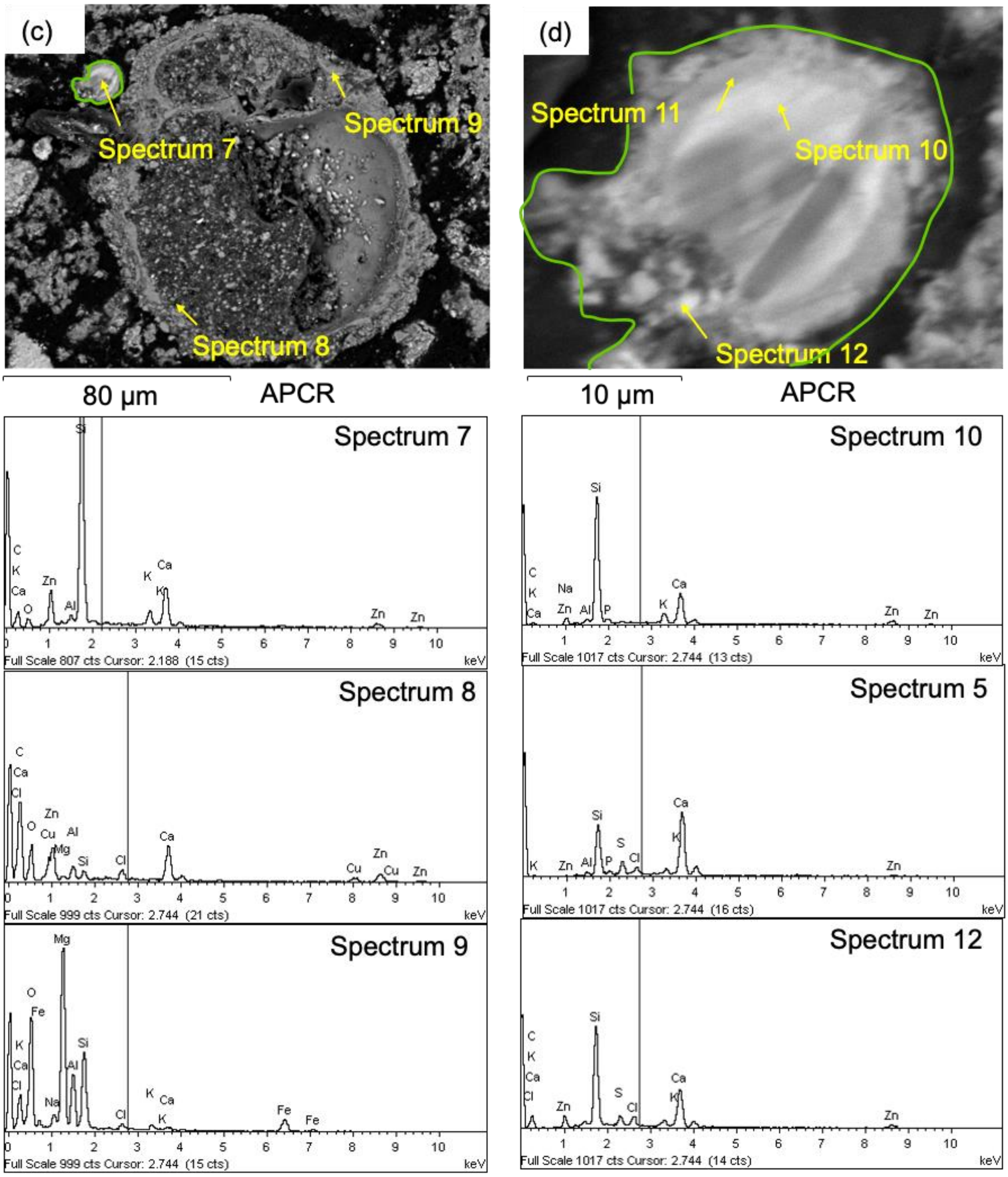

Figure E9 Scanning Electron Microscopy with Energy Dispersive Spectroscopy (SEM-EDS) of the APCR sample (a-d).

Reference

1. Hill, R., The crystal structure and infrared properties of adamite. *American Mineralogist*, 1976. **61**(9-10): p. 979-986.
2. Rajamani, V.t. and Prewitt, C., The crystal structure of millerite. *The Canadian Mineralogist*, 1974. **12**(4): p. 253-257.
3. Skinner, B.J., Unit-cell edges of natural and synthetic sphalerites*. *American Mineralogist*, 1961. **46**(11-12): p. 1399-1411.
4. Ito, T., Morimoto, N., and Sadanaga, R., The crystal structure of realgar. *Acta Crystallographica*, 1952. **5**(6): p. 775-782.
5. Jellinek, F., The structures of the chromium sulphides. *Acta Crystallographica*, 1957. **10**(10): p. 620-628. https://doi.org/10.1107/S0365110X57002200.
6. Evans Jr, H.T., The crystal structures of low chalcocite and djurleite. *Zeitschrift für Kristallographie-Crystalline Materials*, 1979. **150**(1-4): p. 299-320. https://doi.org/10.1524/zkri.1979.150.14.299.
7. Boher, P., et al., Monoxyde quadratique PbOα (I): Description de la transition structurale ferroe´ lastique. *Journal of Solid State Chemistry*, 1985. **57**(3): p. 343-350. https://doi.org/10.1016/0022-4596(85)90197-5.
8. Aqion. *Solubility product constants Ksp at 25°C*. [cited 2023 01/30]; Available from: https://www.aqion.de/site/16.
9. Sasaki, S., Fujino, K., and Takéuchi, Y., X-ray determination of electron-density distributions in oxides, MgO, MnO, CoO, and NiO, and atomic scattering factors of their constituent atoms. *Proceedings of the Japan Academy, Series B*, 1979. **55**(2): p. 43-48. https://doi.org/10.2183/pjab.55.43.
10. Lousnathan, S.J., Refinement of the crystal structure of hardystonite, $Ca_2ZnSi_2O_7$. *Zeitschrift für Kristallographie-Crystalline Materials*, 1969. **130**(1-6): p. 427-437. https://doi.org/10.1524/zkri.1969.130.16.427.
11. Mullen, D. and Nowacki, W., Refinement of the crystal structures of realgar, AsS and orpiment, As_2S_3. *Zeitschrift für Kristallographie-Crystalline Materials*, 1972. **136**(1-6): p. 48-65. https://doi.org/10.1524/zkri.1972.136.16.48.
12. Atkinson, T.D., Fjellvåg, H., and Kjekshus, A., Synthesis, structure, and properties of chromium (III) sulfates. *Journal of Solid State Chemistry*, 2004. **177**(11): p. 4351-4358. https://doi.org/10.1016/j.jssc.2004.03.038.
13. Kisi, E.H. and Elcombe, M.M., u parameters for the wurtzite structure of ZnS and ZnO using powder neutron diffraction. *Acta crystallographica. Section C, Crystal structure communications*, 1989. **45**(12): p. 1867-1870. https://doi.org/10.1107/s0108270189004269.
14. Leciejewicz, J., On the crystal structure of tetragonal (red) PbO. *Acta Crystallographica*, 1961. **14**(12): p. 1304-1304. https://doi.org/10.1107/S0365110X61003892.
15. Evans, H. and Konnert, J., Crystal structure refinement of covellite. *Am. Mineral*, 1976. **61**(9-10): p. 996-1000. https://doi.org/10.2475/ajs.s5-17.102.489
16. Council, N.R., Arsenic: Medical and Biologic Effects of Environmental Pollutants. 1977.
17. Huang, L., et al., Trivalent chromium solubility and its influence on quantification of hexavalent chromium in ambient particulate matter using EPA method 6800. *Journal of the Air & Waste Management Association*, 2014. **64**(12): p. 1439-1445. https://doi.org/10.1080/10962247.2014.951745.
18. Barnhart, J., Occurrences, uses, and properties of chromium. *Regulatory toxicology and pharmacology*, 1997. **26**(1): p. S3-S7. https://doi.org/10.1006/rtph.1997.1132.
19. Rissler, J., et al., Identification and quantification of chemical forms of Cu and Zn in MSWI ashes using XANES. *Energy & Fuels*, 2020. **34**(11): p. 14505-14514. https://doi.org/10.1021/acs.energyfuels.0c02226.
20. Escobal, J., et al., Neutron diffraction, specific heat and magnetic susceptibility of $Ni_3(PO_4)_2$. *Journal of Solid State Chemistry*, 2005. **178**(9): p. 2626-2634. https://doi.org/10.1016/j.jssc.2005.06.022.
21. Huang, H.-H., The Eh-pH diagram and its advances. *Metals*, 2016. **6**(1): p. 23. https://doi.org/10.3390/met6010023.
22. Li, W., Synthesis and solubility of arsenic tri-sulfide and sodium arsenic oxy-sulfide complexes in alkaline sulfide solutions. 2013, University of British Columbia.

23. Clara, M., Magalhães, F., and Williams, P.A., Apatite group minerals: solubility and environmental remediation, in Thermodynamics, solubility and environmental issues. 2007, *Elsevier*. p. 327-340.
24. Feitknecht, W. and Schindler, P., Solubility constants of metal oxides, metal hydroxides and metal hydroxide salts in aqueous solution. *Pure and Applied Chemistry*, 1963. **6**(2): p. 125-206.
25. Brandt, I.S., et al., Electrodeposition of Cu_2O: growth, properties, and applications. *Journal of Solid State Electrochemistry*, 2017. **21**: p. 1999-2020. https://doi.org/10.1007/s10008-017-3660-x.
26. Alwan, A.K. and Williams, P.A., Mineral formation from aqueous solution. Part I. The deposition of hydrozincite, Zn 5 (OH) 6 (CO 3) 2, from natural waters. *Transition Metal Chemistry*, 1979. **4**(2): p. 128-132.
27. Asbrink, S. and Waskowska, A., CuO: X-ray single-crystal structure determination at 196 K and room temperature. *Journal of Physics: Condensed Matter*, 1991. **3**(42): p. 8173. https://doi.org/10.1088/0953-8984/3/42/012.
28. Jr, F. and J, A., The crystal structure of claudetite (monoclinic As_2O_3). *American Mineralogist: Journal of Earth and Planetary Materials*, 1951. **36**(11-12): p. 833-850.
29. Lenaz, D., et al., Structural changes and valence states in the MgCr 2 O 4–FeCr 2 O 4 solid solution series. *Physics and Chemistry of Minerals*, 2004. **31**: p. 633-642. https://doi.org/10.1007/s00269-004-0420-0.
30. Ibrahim, A.H., et al., Cost-effective and high purity valuable metals extraction from water leaching solid residues obtained as a by-product from processing the Egyptian boiler ash. *Minerals*, 2022. **12**(9): p. 1084. https://doi.org/10.3390/min12091084.
31. Wildner, M. and Giester, G., The crystal structures of kieserite-type compounds. I, Crystal structures of Me (II) SO_4.H2O (Me= Mn, Fe, Co, Ni, Zn). *Neues Jahrbuch für Mineralogie Monatshefte*, 1991(7): p. 296-306.
32. Zachara, J., et al., Solubility and surface spectroscopy of zinc precipitates on calcite. *Geochimica et Cosmochimica Acta*, 1989. **53**(1): p. 9-19. https://doi.org/10.1016/0016-7037(89)90268-8.
33. Zemann, J., et al., Neutron single-crystal refinement of cerussite, PbCO3, and comparison with other aragonite-type carbonates. *Zeitschrift für Kristallographie-Crystalline Materials*, 1992. **199**(1-4): p. 67-74. https://doi.org/10.1524/zkri.1992.199.14.67.
34. Schock, M.R., et al. Mode of occurrence, treatment, and monitoring significance of tetravalent lead. in *AWWA Water Quality Technology Conference*. 2005. Quebec City, Quebec.
35. Mitchell, D., et al., Ab initio electric-field gradients and electron densities at Al 27, Fe 57, and Zn 67 in the spinels ZnAl 2 O 4 and ZnFe 2 O 4. *Physical Review B*, 1996. **53**(12): p. 7684.
36. Dera, P., et al., Structural and electronic evolution of Cr_2O_3 on compression to 55 GPa. *Journal of Solid State Chemistry*, 2011. **184**(11): p. 3040-3049. https://doi.org/10.1016/j.jssc.2011.09.021.
37. Oswald, H.-R., et al., Structure of copper (II) hydroxide, $Cu\ (OH)_2$. *Acta Crystallographica Section C: Crystal Structure Communications*, 1990. **46**(12): p. 2279-2284. https://doi.org/10.1107/S0108270190006230.
38. Yousuf, M., et al., The interfacial chemistry of solidification/stabilization of metals in cement and pozzolanic material systems. *Waste Management*, 1995. **15**(2): p. 137-148. https://doi.org/10.1016/0956-053X(95)00013-P.
39. Gogol, D.B., et al., Evaluation of solubility and thermodynamic properties of synthetic nickel hydroxide carbonate. *Available at SSRN 4616469*, 2023. http://dx.doi.org/10.2139/ssrn.4616469.
40. Mathew, M., et al., The crystal structure of α-$Ca_3(PO_4)_2$. *Acta Crystallographica Section B: Structural Crystallography and Crystal Chemistry*, 1977. **33**(5): p. 1325-1333.
41. Crocket, J.H. and Winchester, J.W., Coprecipitation of zinc with calcium carbonate. *Geochimica et Cosmochimica Acta*, 1966. **30**(10): p. 1093-1109. 10.1016/0016-7037(66)90119-0.
42. Stephens, J.S. and Calvo, C., Crystal structure of β-$Zn_3(PO_4)_2$. *Canadian Journal of Chemistry*, 1967. **45**(20): p. 2303-2316. 10.1139/v67-376.
43. Bargouth, M. and Will, G., A neutron diffraction refinement of the crystal structure of tetragonal nickel sulfate hexahydrate. 1981, International Centre for Theoretical Physics.

44. Li, H.-x., Wang, Y., and Cang, D.-q., Zinc leaching from electric arc furnace dust in alkaline medium. *Journal of Central South University of Technology*, 2010. **17**(5): p. 967-971. https://doi.org/10.1007/s11771-010-0585-2.
45. Iskhakova, L., Dubrovinskii, L., and Charushnikova, I., Crystal structure, calculation of parameters of atomic interaction potential and thermochemical properties of NiSO4· nH2O (n= 7, 6). *Kristallografiya*, 1991. **36**: p. 650-655.
46. Jacobsen, S.D., et al., Rigid-body character of the SO_4 groups in celestine, anglesite and barite. *Canadian mineralogist*, 1998. **36**: p. 1053-1060.
47. Hill, R.J., et al., A neutron-diffraction study of hemimorphite. *Zeitschrift für Kristallographie-Crystalline Materials*, 1977. **146**(4-6): p. 241-259. https://doi.org/10.1524/zkri.1977.146.4-6.241.
48. Calvo, C., The crystal structure and luminescence of γ-zinc orthophosphate. *Journal of Physics and Chemistry of Solids*, 1963. **24**(1): p. 141-149. https://doi.org/10.1016/0022-3697(63)90049-0.
49. Miller, J., The cystal structure of anhydrous sodium chromate, Na_2CrO_4. *Zeitschrift für Kristallographie-Crystalline Materials*, 1936. **94**(1-6): p. 131-136.
50. Nishimura, T. and Robins, R., A re-evaluation of the solubility and stability regions of calcium arsenites and calcium arsenates in aqueous solution at 25 C. *Mineral Processing and Extractive Metullargy Review*, 1998. **18**(3-4): p. 283-308. https://doi.org/10.1080/08827509808914159.
51. Wells, A., Malachite: re-examination of crystal structure. *Acta Crystallographica*, 1951. **4**(3): p. 200-204. https://doi.org/10.1107/S0365110X51000714.
52. Gokul, B., et al., Polymorphism induced magnetic transitions in Ni (OH) 2 nanostructures. *Journal of Magnetism and Magnetic Materials*, 2021. **539**: p. 168364. https://doi.org/10.1016/j.jmmm.2021.168364.
53. Medas, D., et al., Stability of biological and inorganic hemimorphite: Implications for hemimorphite precipitation in non-sulfide Zn deposits. *Ore Geology Reviews*, 2017. **89**: p. 808-821. https://doi.org/10.1016/j.oregeorev.2017.07.015.
54. Dupuis, V., et al., Solubility and disintegration of zinc phosphate cement. *Biomaterials*, 1992. **13**(7): p. 467-470. https://doi.org/10.1016/0142-9612(92)90168-N.
55. Cowley, J., Electron-diffraction study of the structure of basic lead carbonate, $2PbCO_3{\cdot}Pb(OH)_2$. *Acta Crystallographica*, 1956. **9**(4): p. 391-396. https://doi.org/10.1107/S0365110X56001133.
56. Wang, Q., et al., Reaction mechanism and distribution behavior of arsenic in the bottom blown copper smelting process. *Metals*, 2017. **7**(8): p. 302. https://doi.org/10.3390/met7080302.
57. Stephens, J.S. and Cruickshank, D.W.J., The crystal structure of (CrO_3)[infinity]. *Acta Crystallographica Section B*, 1970. **26**(3): p. 222-226. https://doi.org/10.1107/S0567740870002182.
58. Shoemaker, G., Anderson, J., and Kostiner, E., Copper (II) phosphate. *Acta Crystallographica Section B: Structural Crystallography and Crystal Chemistry*, 1977. **33**(9): p. 2969-2972. https://doi.org/10.1107/S0567740877010012.
59. Li, Y., et al., Removal of arsenic from arsenate complex contained in secondary zinc oxide. *Hydrometallurgy*, 2011. **109**(3): p. 237-244. https://doi.org/10.1016/j.hydromet.2011.07.007.
60. Jansen, M., Kristallstruktur von As_2O_5. *Angewandte Chemie*, 1977. **89**(5): p. 326-327. https://doi.org/10.1002/ange.19770890511
61. Ghose, S., The crystal structure of hydrozincite, $Zn_5(OH)_6(CO_3)_2$. *Acta Crystallographica*, 1964. **17**(8): p. 1051-1057. https://doi.org/10.1107/S0365110X64002651.
62. Parise, J. and Hyde, B., The structure of atacamite and its relationship to spinel. *Acta Crystallographica Section C: Crystal Structure Communications*, 1986. **42**(10): p. 1277-1280. https://doi.org/10.1107/S0108270186092570.
63. Andersson, D.A. and Stanek, C.R., Mixing and non-stoichiometry in Fe–Ni–Cr–Zn–O spinel compounds: density functional theory calculations. *Physical Chemistry Chemical Physics*, 2013. **15**(37): p. 15550-15564. https://doi.org/10.1039/C3CP50312G.
64. Iskhakova, L.D., et al., Crystal structure of chalcanthite $CuSO_4{\cdot}5H_2O$ grown under microgravity. *Kristallografiya*, 1991.
65. Gomes, A.F.S., Lopez, D.L., and Ladeira, A.C.Q., Characterization and assessment of chemical modifications of metal-bearing sludges arising from unsuitable disposal. *Journal*

of Hazardous Materials, 2012. **199-200**: p. 418-425. https://doi.org/10.1016/j.jhazmat.2011.11.039.

66. Rai, D., Eary, L., and Zachara, J.M., Environmental chemistry of chromium. *Science of the total environment*, 1989. **86**(1-2): p. 15-23. https://doi.org/10.1016/0048-9697(89)90189-7.
67. Calvo, C., The crystal structure of α-$Zn_3(PO_4)_2$. *Canadian Journal of Chemistry*, 1965. **43**(2): p. 436-445. https://doi.org/10.1139/v65-058.
68. Tang, Y., et al., Structural properties of the Cr (III)− Fe (III)(Oxy) hydroxide compositional series: insights for a nanomaterial "solid solution". *Chemistry of Materials*, 2010. **22**(12): p. 3589-3598. https://doi.org/10.1021/cm1000472.
69. *Spinel & inverse spinel crystal structures*. [cited 2021 7th March]; Available from: https://www.adichemistry.com/inorganic/cochem/spinels/spinel-structures.html.
70. Biagioni, C. and Pasero, M., The systematics of the spinel-type minerals: An overview. *American Mineralogist*, 2014. **99**(7): p. 1254-1264. https://doi.org/10.2138/am.2014.4816.
71. Cameron, E.M., Leybourne, M.I., and Palacios, C., Atacamite in the oxide zone of copper deposits in northern Chile: involvement of deep formation waters? *Mineralium Deposita*, 2007. **42**: p. 205-218. https://doi.org/10.1007/s00126-006-0108-0.
72. Noda, Y., et al., Charge distribution and atomic thermal vibration in lead chalcogenide crystals. *Acta Crystallographica Section B: Structural Science*, 1983. **39**(3): p. 312-317. https://doi.org/10.1107/S0108768183002463.
73. El-eswed, B.I., Chemical evaluation of immobilization of wastes containing Pb, Cd, Cu and Zn in alkali-activated materials: A critical review. *Journal of Environmental Chemical Engineering*, 2020. **8**(5): p. 104194. https://doi.org/10.1016/j.jece.2020.104194.
74. Reichle, R.A., McCurdy, K.G., and Hepler, L.G., Zinc hydroxide: solubility product and hydroxy-complex stability constants from 12.5–75 C. *Canadian Journal of Chemistry*, 1975. **53**(24): p. 3841-3845.
75. Shi, Q., et al., Effect of solution chemistry on the flotation system of smithsonite and calcite. *International Journal of Mineral Processing*, 2013. **119**: p. 34-39. https://doi.org/10.1016/j.minpro.2012.12.011.
76. Patterson, J.W., Allen, H.E., and Scala, J.J., Carbonate precipitation for heavy metals pollutants. *Journal (Water Pollution Control Federation)*, 1977: p. 2397-2410.
77. Hales, M.C. and Frost, R.L., Thermal analysis of smithsonite and hydrozincite. *Journal of thermal analysis calorimetry*, 2008. **91**(3): p. 855-860.
78. Vágvölgyi, V., et al., Dynamic and controlled rate thermal analysis of hydrozincite and smithsonite. *Journal of thermal analysis calorimetry*, 2008. **92**(3): p. 911-916.
79. Ziegler, F., et al., Sorption mechanisms of zinc to calcium silicate hydrate: X-ray absorption fine structure (XAFS) investigation. *Environmental Science & Technology*, 2001. **35**(7): p. 1550-1555. https://doi.org/10.1021/es001437+.
80. Yang, J., et al., Hydrothermal synthesis and optical properties of zinc silicate hierarchical superstructures. *Materials Letters*, 2011. **65**(19-20): p. 3030-3033. https://doi.org/10.1016/j.matlet.2011.06.068.
81. Bisengalieva, M.R., et al., A thermal and thermochemical study of natural hemimorphite. *Russian Journal of Physical Chemistry A*, 2010. **84**(9): p. 1481-1484. https://doi.org/10.1134/S0036024410090050.
82. Li, M.-J., et al., Effects of SiO_2, Al_2O_3 and Fe_2O_3 on leachability of Zn, Cu and Cr in ceramics incorporated with electroplating sludge. *Journal of Environmental Chemical Engineering*, 2017. **5**(4): p. 3143-3150. https://doi.org/10.1016/j.jece.2017.06.019.
83. Blanco-Gutiérrez, V., et al., X-ray absorption spectroscopy and Mössbauer spectroscopy studies of superparamagnetic $ZnFe_2O_4$ nanoparticles. *The Journal of Physical Chemistry C*, 2011. **115**(5): p. 1627-1634. https://doi.org/10.1021/jp109368z.
84. Jeyadevan, B., Tohji, K., and Nakatsuka, K., Structure analysis of coprecipitated $ZnFe_2O_4$ by extended x-ray-absorption fine structure. *Journal of Applied Physics*, 1994. **76**(10): p. 6325-6327. https://doi.org/10.1063/1.358255.
85. Akhtar, M.J. and Nadeem, M., Structural studies of $ZnFe_2O_4$ nanoparticles by synchrotron X-ray absorption spectroscopy. *Thai Journal of Physics*, 2008.
86. Raeisi Shahraki, R., et al., Structural characterization and magnetic properties of superparamagnetic zinc ferrite nanoparticles synthesized by the coprecipitation method. *Journal of Magnetism and Magnetic Materials*, 2012. **324**(22): p. 3762-3765. https://doi.org/10.1016/j.jmmm.2012.06.020.

87. Babu, K.S., et al., High thermal annealing effect on structural and optical properties of ZnO–SiO2 nanocomposite. *Materials science in semiconductor processing*, 2014. **27**: p. 643-648. https://doi.org/10.1016/j.mssp.2014.07.055.

88. Nguyen, N.H., et al., Effect of Zn/Si ratio on the microstructural and microwave dielectric properties of Zn2SiO4 ceramics. *Journal of the American Ceramic Society*, 2007. **90**(10): p. 3127-3130. 10.1111/j.1551-2916.2007.01891.x.

89. Britannica, T. *Sorosilicate*. [cited 2021 9th March]; Available from: https://www.britannica.com/science/sorosilicate.

90. Gasek, K., et al., Characteristic of synthesis and transformations of hardystonite in willemite glass-crystalline glaze based on thermal analysis. *Journal of Thermal Analysis and Calorimetry*, 2016. **125**: p. 1135-1142. https://doi.org/10.1007/s10973-016-5429-3.

91. Sadeghzade, S., Emadi, R., and Labbaf, S., Formation mechanism of nano-hardystonite powder prepared by mechanochemical synthesis. *Advanced Powder Technology*, 2016. **27**(5): p. 2238-2244. https://doi.org/10.1016/j.apt.2016.08.010.

92. Wu, C.T., Chang, J., and Zhai, W.Y., A novel hardystonite bioceramic: preparation and characteristics. *Ceramics International*, 2005. **31**(1): p. 27-31. https://doi.org/10.1016/j.ceramint.2004.02.008.

93. Ahamad Mohiddon, M., et al., Chromium oxide as a metal diffusion barrier layer: An x-ray absorption fine structure spectroscopy study. *Journal of Applied Physics*, 2014. **115**(4). https://doi.org/10.1063/1.4863309.

94. Blacklocks, A.N., et al., An XAS study of the defect structure of Ti-doped α-Cr_2O_3. *Solid State Ionics*, 2006. **177**(33-34): p. 2939-2944. https://doi.org/10.1016/j.ssi.2006.08.028.

95. Kane, S., et al., Extended X-ray absorption fine structure (EXAFS) measurement of Cu metal foil using thermal wave detector: A comparative study. *Nuclear Instruments and Methods in Physics Research Section A: Accelerators, Spectrometers, Detectors and Associated Equipment*, 2024. **1060**: p. 169066. https://doi.org/10.1016/j.nima.2023.169066.

96. Tagirov, B.R., et al., Covellite CuS as a matrix for “invisible” gold: X-ray spectroscopic study of the chemical state of Cu and Au in synthetic minerals. *Geochimica et Cosmochimica Acta*, 2016. **191**: p. 58-69. https://doi.org/10.1016/j.gca.2016.07.015.

97. Pattrick, R., et al., The structure of amorphous copper sulfide precipitates: An X-ray absorption study. *Geochimica et Cosmochimica Acta*, 1997. **61**(10): p. 2023-2036. https://doi.org/10.1016/S0016-7037(97)00061-6.

98. Helz, G.R., Vaughan, D.J., and Garner, C.D., Multinuclearity of aqueous copper and zinc bisulfide complexes: An EXAFS investigation. *Geochimica et Cosmochimica Acta*, 1993. **57**(1): p. 15-25. https://doi.org/10.1016/0016-7037(93)90464-8.

99. Ichiyanagi, Y., et al., X-ray absorption fine-structure study on the $Ni(OH)_2$ monolayer nanoclusters. *Chemical physics letters*, 2003. **379**(3-4): p. 345-350. https://doi.org/10.1016/j.cplett.2003.08.051.

100. Pandya, K., et al., Extended X-ray absorption fine structure investigations of nickel hydroxides. *Journal of physical chemistry*, 1990. **94**(1): p. 21-26. https://pubs.acs.org/doi/pdf/10.1021/j100364a005.

101. Trivedi, P., Axe, L., and Tyson, T.A., An Analysis of Zinc Sorption to Amorphous versus Crystalline Iron Oxides Using XAS. *Journal of Colloid and Interface Science*, 2001. **244**(2): p. 230-238. https://doi.org/10.1006/jcis.2001.7971.

102. Albertsson, J., Abrahams, S., and Kvick, Å., Atomic displacement, anharmonic thermal vibration, expansivity and pyroelectric coefficient thermal dependences in ZnO. *Acta Crystallographica Section B: Structural Science*, 1989. **45**(1): p. 34-40. https://doi.org/10.1107/S0108768188010109.

103. Rose, J., et al., X-ray absorption spectroscopy study of immobilization processes for heavy metals in calcium silicate hydrates. 2. Zinc. *Langmuir*, 2001. **17**(12): p. 3658-3665. https://doi.org/10.1021/la001302h.

104. Waychunas, G.A., Fuller, C.C., and Davis, J.A., Surface complexation and precipitate geometry for aqueous Zn(II) sorption on ferrihydrite I: X-ray absorption extended fine structure spectroscopy analysis. *Geochimica et Cosmochimica Acta*, 2002. **66**(7): p. 1119-1137. https://doi.org/10.1016/S0016-7037(01)00853-5.

105. Roberts, D.R., Ford, R.G., and Sparks, D.L., Kinetics and mechanisms of Zn complexation on metal oxides using EXAFS spectroscopy. *Journal of Colloid and Interface Science*, 2003. **263**(2): p. 364-376. https://doi.org/10.1016/S0021-9797(03)00281-9.

106. Struis, R.P.W.J., et al., Speciation of zinc in municipal solid waste incineration fly ash after heat treatment: an X-ray absorption spectroscopy study. *Environmental Science & Technology*, 2004. **38**(13): p. 3760. https://doi.org/10.1021/es0346126.
107. Steenari, B.-M. and Noren, K., Speciation of Zinc in ash investigated by X-ray absorption spectroscopy. 2008: Sweden.
108. Ndiba, P.K., Phosphate and thermal stabilization of heavy metals in dredged sediments. 2009.
109. Tang, Y.Z., et al., Zinc incorporation into hydroxylapatite. *Biomaterials*, 2009. **30**(15): p. 2864-2872. https://doi.org/10.1016/j.biomaterials.2009.01.043.
110. Cai, X., et al., Characterization of zinc vapor condensation in fly ash particles using synchrotron X-ray absorption spectroscopy. *Journal of Zhejiang University-Science A*, 2015. **16**(1): p. 70-80. https://doi.org/10.1631/jzus.A1400178.
111. Tiberg, C., Sjöstedt, C., and Karlfeldt Fedje, K., Speciation of Cu and Zn in bottom ash from solid waste incineration studied by XAS, XRD, and geochemical modelling. *Waste Management*, 2021. **119**: p. 389-398. https://doi.org/10.1016/j.wasman.2020.10.023.
112. Ziegler, F., Heavy metal binding in cement-based waste materials: an investigation of the mechanism of zinc sorption to calcium silicate hydrate. 2000, ETH Zurich.
113. Libowitzky, E., et al., Proton disorder in dehydrated hemimorphite-IR spectroscopy and X-ray structure refinement at low and ambient temperatures. *European Journal of Mineralogy*, 1997. **9**(4): p. 803-810.
114. Cassingham, N.J., et al., The structural role of Zn in nuclear waste glasses. *International Journal of Applied Glass Science*, 2011. **2**(4): p. 343-353. https://doi.org/10.1111/j.2041-1294.2011.00067.x.
115. Smith, D.R. and Nordberg, M., Chapter 2 - General Chemistry, Sampling, Analytical Methods, and Speciation∗. Handbook on the Toxicology of Metals (Fourth Edition), ed. G.F. Nordberg, B.A. Fowler, and M. Nordberg. 2015, *San Diego*: *Academic Press*. 15-44.
116. Arsenic, A.M., et al., Method 3050B acid digestion of sediments, sludges, and soils 1.0 scope and application. *Washington, DC, USA*, 1996.
117. Technical Committee ISO/TC 190, S.q., Soil quality: Extraction of trace elements soluble in aqua regia. 1995: *International Organization for Standardization*.
118. Thomas, R., Practical guide to ICP-MS: a tutorial for beginners. 2008: *CRC press*.
119. Russo, R., et al., Time-resolved plasma diagnostics and mass removal during single-pulse laser ablation. *Applied Physics A*, 1999. **69**: p. S887-S894.
120. Tessier, A., Campbell, P.G., and Bisson, M., Sequential extraction procedure for the speciation of particulate trace metals. *Analytical chemistry*, 1979. **51**(7): p. 844-851.
121. Ure, A., et al., Improvements in the determination of extractable contents of trace metals in soil sediment prior to certification. 1993, Commission of the European Communities—BCR Information.
122. Bacon, J.R. and Davidson, C.M., Is there a future for sequential chemical extraction? *Analyst*, 2008. **133**(1): p. 25-46. https://doi.org/10.1039/B711896A.
123. Stegemann, J.A. and Cote, P.L., Summary of an investigation of test methods for solidified waste evaluation. *Waste management*, 1990. **10**(1): p. 41-52.
124. Stanjek, H. and Häusler, W., Basics of X-ray Diffraction. *Hyperfine Interactions*, 2004. **154**(1): p. 107-119. https://doi.org/10.1023/B:HYPE.0000032028.60546.38.
125. Rietveld, H.M., A profile refinement method for nuclear and magnetic structures. *Journal of applied Crystallography*, 1969. **2**(2): p. 65-71.
126. Ager III, J.W. Overview of optical microscopy and optical microspectroscopy. in *AIP Conference Proceedings*. 1998. American Institute of Physics.
127. Santoro, L., et al., Mineralogical characterization of the Hakkari nonsulfide Zn(Pb) deposit (Turkey): The benefits of QEMSCAN®. *Minerals Engineering*, 2014. **69**: p. 29-39. https://doi.org/10.1016/j.mineng.2014.07.002.
128. Rollinson, G.K., et al., Characterisation of non-sulphide zinc deposits using QEMSCAN®. *Minerals Engineering*, 2011. **24**(8): p. 778-787. https://doi.org/doi.org/10.1016/j.mineng.2011.02.004.
129. Mössbauer, R.L., Kernresonanzfluoreszenz von gammastrahlung in Ir 191. *Zeitschrift für Physik*, 1958. **151**: p. 124-143.
130. Gütlich, P., Schröder, C., and Schünemann, V., Mössbauer spectroscopy—an indispensable tool in solid state research. *Spectroscopy Europe*, 2012. **24**(4): p. 21.

131. Seah, M., The quantitative analysis of surfaces by XPS: A review. *Surface and Interface Analysis*, 1980. **2**(6): p. 222-239. https://doi.org/10.1002/sia.740020607.
132. Berthomieu, C. and Hienerwadel, R., Fourier transform infrared (FTIR) spectroscopy. *Photosynthesis research*, 2009. **101**: p. 157-170. https://doi.org/10.1007/s11120-009-9439-x.
133. Calvin, S., XAFS for Everyone. 2013: *CRC press*.
134. Pollock, C. *Introduction to Extended X-Ray Absorption Fina Structure (EXAFS)*. [Youtube] 2020 27 05 2020 [cited 2020 25 12]; Available from: https://www.youtube.com/watch?v=gh_1vGVluLA.
135. Takahashi, G., Sample preparation for X-ray fluorescence analysis. *Rigaku J*, 2015. **31**(1): p. 26-30.
136. Bish, D.L. and Reynolds, R.C., 4. SAMPLE PREPARATION FOR X-RAY DIFFRACTION, in Modern Powder Diffraction, L.B. David and E.P. Jeffrey, Editors. 1989, *De Gruyter*: *Berlin, Boston*. p. 73-100.
137. Masciocchi, N. *Data collection: Experimental set-ups and Sample Preparation*. 2008; Available from: https://www2.arnes.si/~sgszmera1/html/xrd/preparation2.html.
138. Carpenter, P., et al., Characterization of Corning EPMA standard glasses 95IRV, 95IRW, and 95IRX. *Journal of research of the National Institute of Standards and Technology*, 2002. **107**(6): p. 703.
139. Vicenzi, E.P., et al., Microbeam characterization of corning archeological reference glasses: new additions to the smithsonian microbeam standard collection. *Journal of Research of the National Institute of Standards and technology*, 2002. **107**(6): p. 719. https://doi.org/10.6028/jres.107.058.
140. Giuli, G., et al., Iron local structure in tektites and impact glasses by extended X-ray absorption fine structure and high-resolution X-ray absorption near-edge structure spectroscopy. *Geochimica et Cosmochimica Acta*, 2002. **66**(24): p. 4347-4353. https://doi.org/10.1016/S0016-7037(02)01030-X.
141. Roy, A., Sulfur speciation in granulated blast furnace slag: An X-ray absorption spectroscopic investigation. *Cement and Concrete Research*, 2009. **39**(8): p. 659-663. https://doi.org/10.1016/j.cemconres.2009.05.007.
142. Roy, A. and Stegemann, J.A., Nickel speciation in cement-stabilized/solidified metal treatment filtercakes. *Journal of Hazardous Materials*, 2017. **321**: p. 353-361. https://doi.org/10.1016/j.jhazmat.2016.09.027.
143. Ettler, V., et al., Vanadium in slags from smelting of African Pb-Zn vanadate ores: mineralogy, extractability and potential recovery. *Journal of Geochemical Exploration*, 2020. **218**: p. 106631. https://doi.org/10.1016/j.gexplo.2020.106631.
144. Chen, D.T., et al., Speciation of toxic pollutants in Pb/Zn smelter slags by X-ray Absorption Spectroscopy in the context of the literature. *Journal of Hazardous Materials*, 2023. **460**: p. 132373. https://doi.org/10.1016/j.jhazmat.2023.132373.
145. Bogush, A.A., et al., Element composition and mineralogical characterisation of air pollution control residue from UK energy-from-waste facilities. *Waste Management*, 2015. **36**: p. 119-129. https://doi.org/10.1016/j.wasman.2014.11.017.
146. Bogush, A.A., Stegemann, J.A., and Roy, A., Changes in composition and lead speciation due to water washing of air pollution control residue from municipal waste incineration. *Journal of Hazardous Materials*, 2019. **361**: p. 187-199. https://doi.org/10.1016/j.jhazmat.2018.08.051.

Appendix F Curve Fitting to Theoretical Standards

F.1 Curve Fitting of Cr Reference Materials to Theoretical Standards

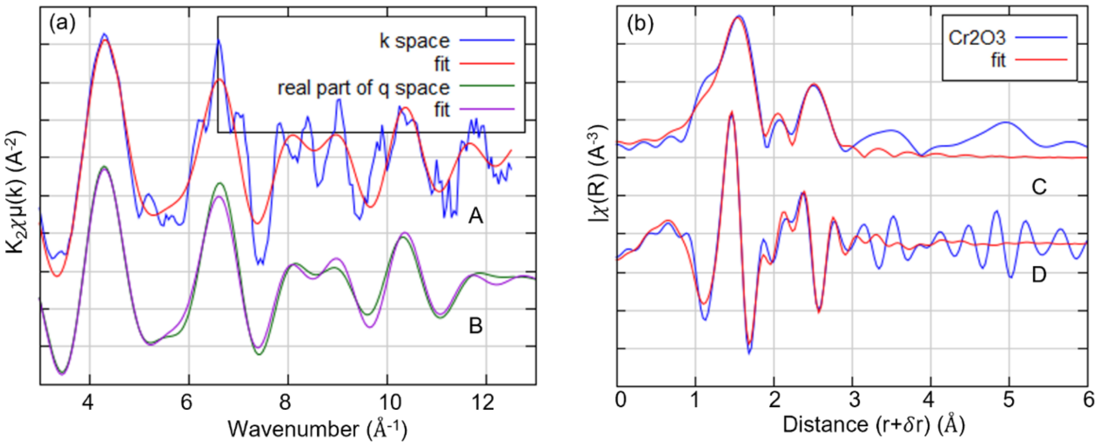

Figure F1 The χ(k) spectra of Cr_2O_3 as measured (A) and fitted and filtered from the corresponding Fourier Transform spectrum (FT) by back Fourier Transformation(B) (a). Spectrum B has been filtered from the 1.0-3.0 Å region; FT spectra of Cr_2O_3 as measured and fitted in magnitude (C) and in real part (D) (b). FT spectrum is uncorrected for phase shift. k-range is 3-11.5 Å^{-1}.

Table F1 Structural parameters derived from curve fitting to theoretical standards for Cr reference materials.

Cr reference materials	Filter (Å)	shell	CN	CN_{ref}	R (Å)	R_{ref}	ΔR	σ^2(Å)	ΔE_0(eV)	R-factor
Cr_2O_3	1.0-2.0	Cr-O	3.0*	6.0	1.953	1.989	-0.013	0.003	1.19	0.026
		Cr-O	3.0*		1.999		-0.013	0.003		
	2.0-3.0	Cr-Cr	1.0*	3.7	2.673	2.849	0.023	0.003		
		Cr-Cr	3.0*		2.912		0.023	0.003		

Amplitude reduction factor SO^2 is set as 0.70 by fitting Cr_2O_3 standard;
* fixed value;
The reference for CN_{ref} and R_{ref} are summarised in Table A7, Appendix A.

F.2 Curve Fitting of Cu Reference Materials to Theoretical Standards

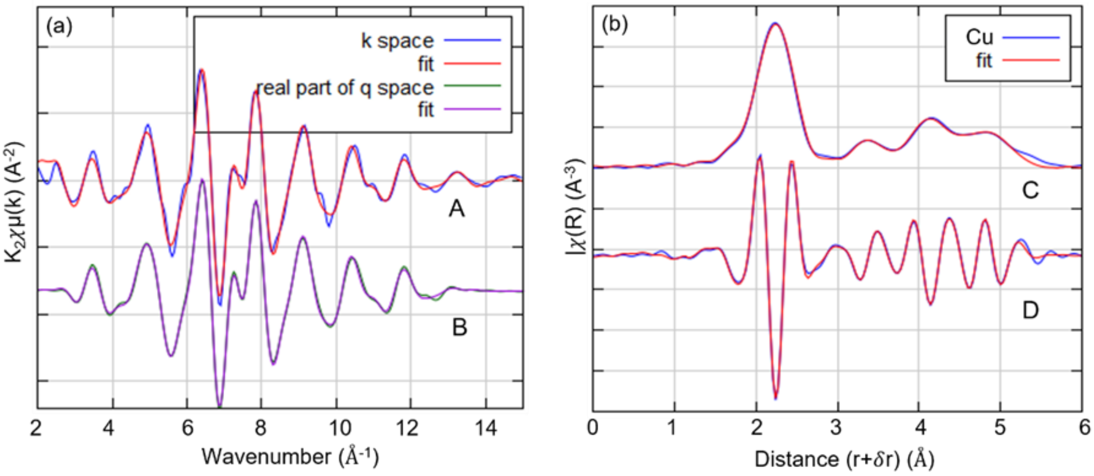

Figure F2 The χ(k) spectra of Cu as measured and fitted (A) and filtered from the corresponding Fourier Transformation (FT) spectrum by back Fourier Transformation(B) (a). Spectrum B has been filtered from the 1.0-5.7 Å region; FT spectrum for Cu as measured and fitted in magnitude (C) and in real part (D) (b). FT spectrum is uncorrected for phase shift. k-range is 3.0-13.0 Å^{-1}.

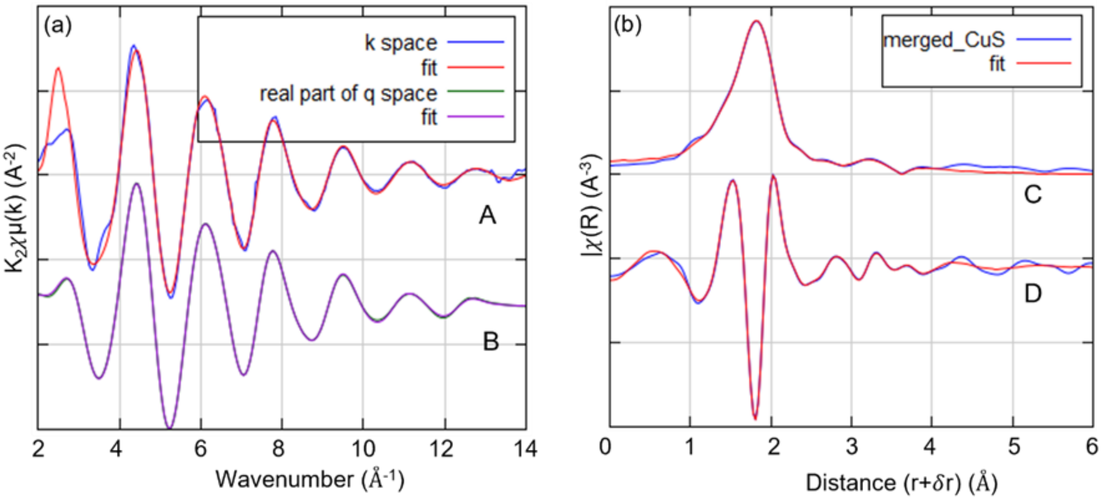

Figure F3 The χ(k) spectra of CuS as measured and fitted (A) and filtered from the corresponding Fourier Transformation (FT) spectrum by back Fourier Transformation(B) (a). Spectrum B has been filtered from the 1.0-4.0 Å region; FT spectrum for CuS as measured and fitted in magnitude (C) and in real part (D) (b). FT spectrum is uncorrected for phase shift. k-range is 3.0-13.0 Å^{-1}.

Table F2 Structural parameters derived from curve fitting to theoretical standard for Cu reference materials

Cu reference materials	Filter (Å)	shell	CN	CN_{ref}	R (Å)	R_{ref}	ΔR	σ^2(Å)	ΔE_0 (eV)	R-factor
Cu	1.0-2.8	Cu-Cu1.1	12.0*	12	2.546	2.548	0.005	0.009	5.21	0.0039
	2.8-5.7	Cu-Cu1.2	6.0*	6	3.609	3.571	0.015	0.013		
		Cu-Cu1.1 Cu1.1	48.0*	/	3.820	/	0.007	0.014		
		Cu-Cu1.1 Cu1.2	48.0*	/	4.351	/	0.013	0.016		
		Cu-Cu1.3	24.0*	24	4.435	4.466	0.033	0.011		
CuS	1.0-2.8	Cu-S1.1	3.0*	3.1	2.234	2.242	0.044	0.006	4.65	0.0007
	2.8-4.0	Cu-S2.1	6.0*	6.0	3.469	3.220	0.004	0.010		
		Cu-S2.1	6.0*	6.0	3.505	3.778	-0.250	0.039		
		Cu-Cu1.1	6.0*	6.0	3.747	3.812	-0.047	0.028		

Amplitude reduction factor SO^2 is set as 0.93 by fitting Cu standard;
* fixed value;
The reference for CN_{ref} and R_{ref} are summarised in Table A8, Appendix A.

F.3 Curve Fitting of Ni Reference Materials to Theoretical Standards

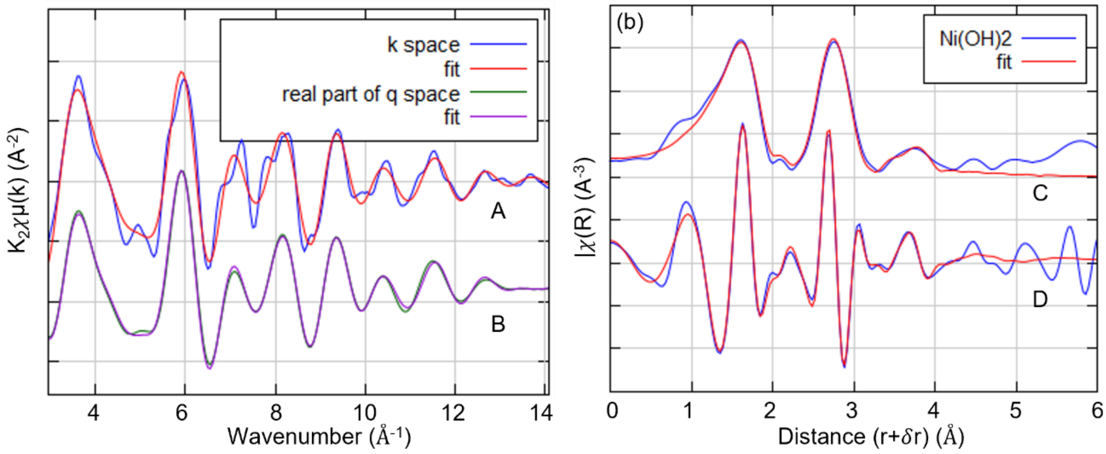

Figure F4 The χ(k) spectra of β-$Ni(OH)_2$ as measured (A) and fitted and filtered from the corresponding Fourier Transform spectrum (FT) by back Fourier Transformation(B) (a). Spectrum B has been filtered from the 1.0-3.3 Å region; FT spectra of $Ni(OH)_2$ as measured and fitted in magnitude (C) and in real part (D) (b). FT spectrum is uncorrected for phase shift. k-range is 3-13.0 Å^{-1}

Table F3 Structural parameters derived from curve fitting to theoretical standards for Ni reference materials

Ni reference materials	Filter (Å)	shell	CN	CN_{ref}	R (Å)	R_{ref}	ΔR	σ^2(Å)	ΔE_0(eV)	R-factor
β-$Ni(OH)_2$	1.0-2.0	Ni-O	6.0*	6.0	2.064	2.094	-0.004	0.007	-5.362	0.007
	2.0-3.3	Ni-O	6.0*	6.0	3.124	3.119	-0.026	0.007	-5.362	
	3.3-4.2	Ni-O	5.9	/	4.178	/	0.060	0.007	7.218	
		Ni-O	0.8	/	3.759	/	-0.009	0.007	7.218	

Amplitude reduction factor SO^2 is set as 0.96 by fitting $Ni(OH)_2$ standard;
* fixed value;
/ unknown;
The reference for CN_{ref} and R_{ref} are summarised in Table A9, Appendix A.

F.4 Curve fitting of Zn Reference Materials to Theoretical Standards

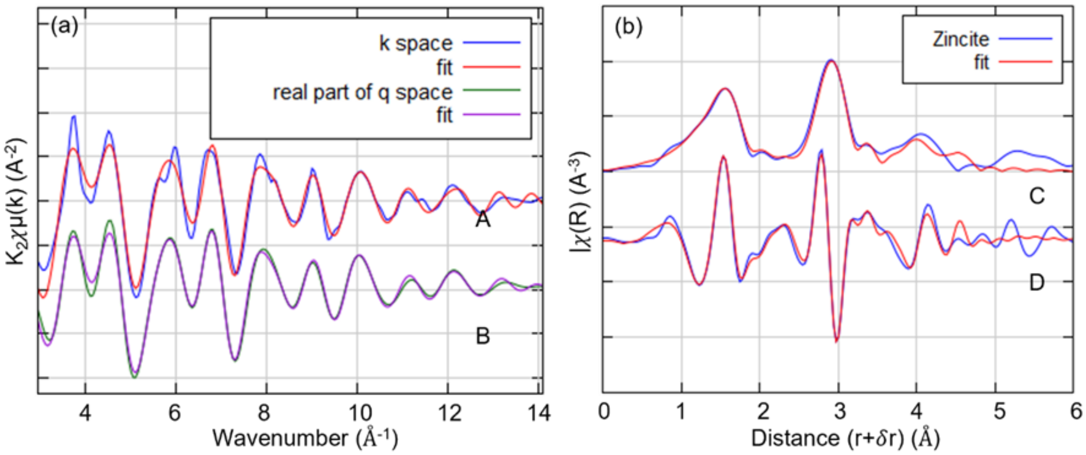

Figure F5 The χ(k) spectra of zincite (ZnO) as measured (A) and fitted and filtered from the corresponding Fourier Transform spectrum (FT) by back Fourier Transformation(B) (a). Spectrum B has been filtered from the 1.0-3.5 Å region; FT spectra of zincite as measured and fitted in magnitude (C) and in real part (D) (b). FT spectrum is uncorrected for phase shift. k-range is 3-13.5 Å^{-1}.

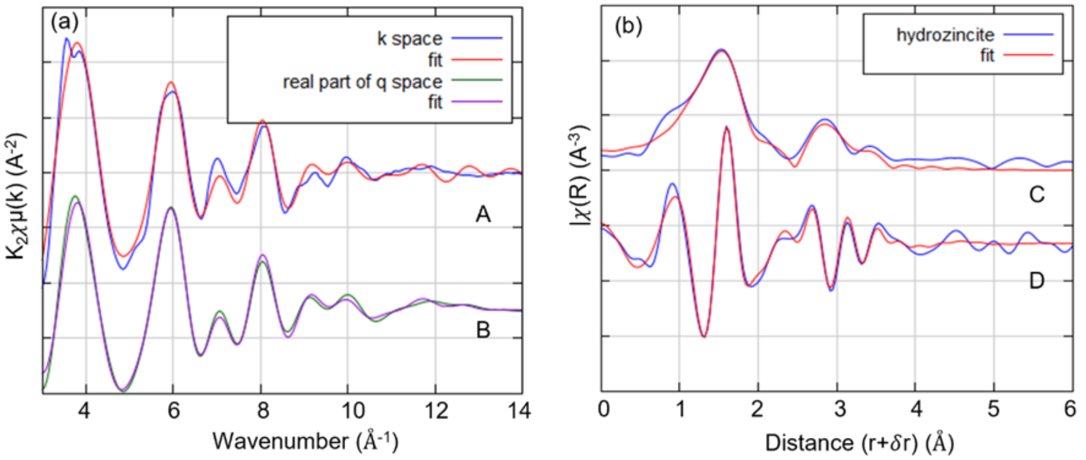

Figure F6 The χ(k) spectra of hydrozincite ($2ZnCO_3 \cdot 3Zn(OH)_2$) as measured (A) and fitted and filtered from the corresponding Fourier Transform spectrum (FT) by back Fourier Transformation(B) (a). Spectrum B has been filtered from the 1.0-3.8 Å region; FT spectra of hydrozincite as measured and fitted in magnitude (C) and in real part (D) (b). FT spectrum is uncorrected for phase shift. k-range is 3-12.0 Å^{-1}.

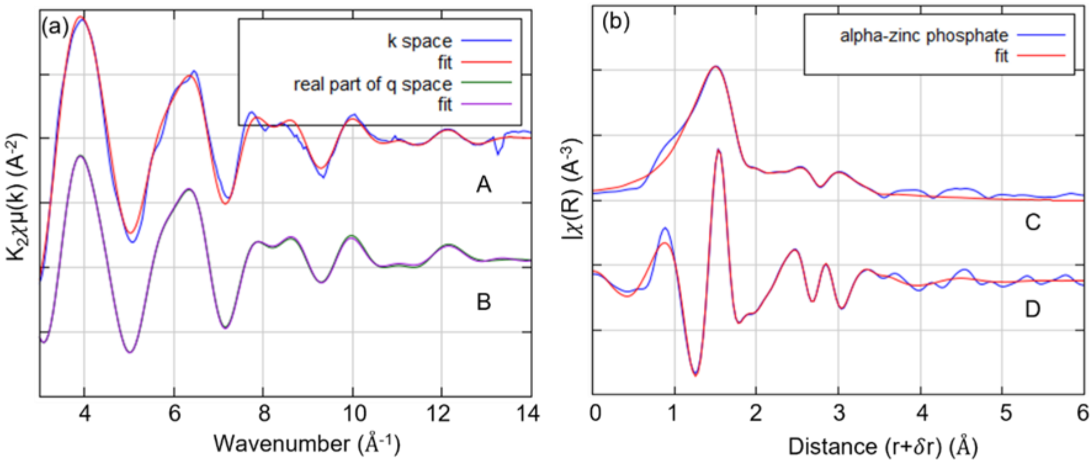

Figure F7 The χ(k) spectra of alpha-zinc phosphate ($Zn_3(PO_4)_2$) as measured (A) and fitted and filtered from the corresponding Fourier Transform spectrum (FT) by back Fourier Transformation(B) (a). Spectrum B has been filtered from the 1.0-3.6 Å region; FT spectra of alpha-zinc phosphate as measured and fitted in magnitude (C) and in real part (D) (b). FT spectrum is uncorrected for phase shift. k-range is 3-13.5 Å-1.

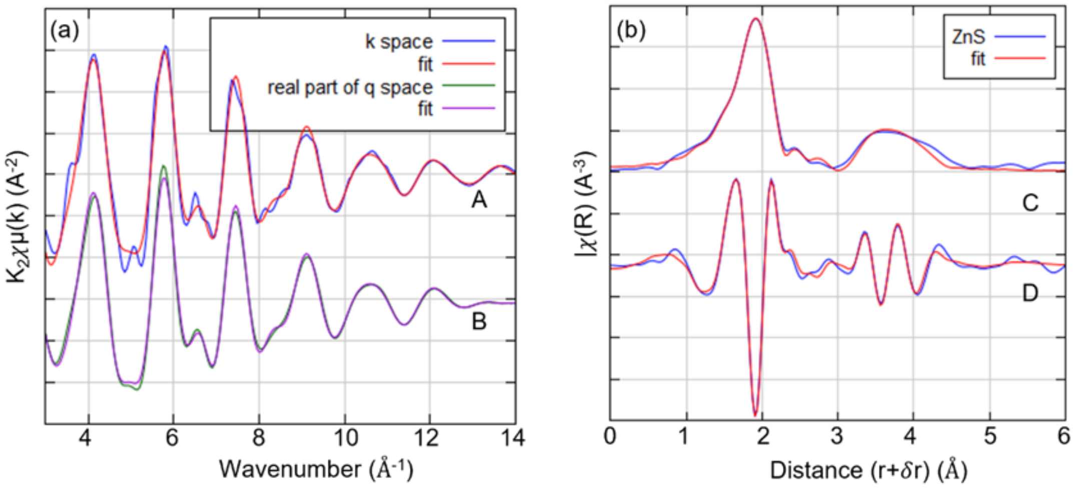

Figure F8 The χ(k) spectra of zinc sulfide (ZnS) as measured (A) and fitted and filtered from the corresponding Fourier Transform spectrum (FT) by back Fourier Transformation (B) (a). Spectrum B has been filtered from the 1.0-4.8 Å region; FT spectra of zinc sulfide as measured and fitted in magnitude (C) and in real part (D) (b). FT spectrum is uncorrected for phase shift. k-range is 3-12.9 Å^{-1}.

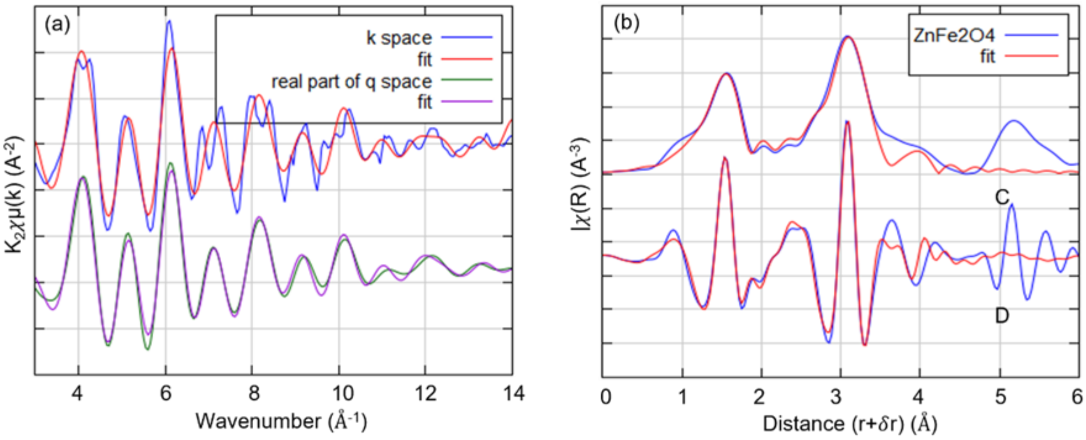

Figure F9 The χ(k) spectra of zinc ferrite ($ZnFe_2O_4$) as measured (A) and fitted and filtered from the corresponding Fourier Transform spectrum (FT) by back Fourier Transformation (B) (a). Spectrum B has been filtered from the 1.0-4 Å region; FT spectra of zinc ferrite as measured and fitted in magnitude (C) and in real part (D) (b). FT spectrum is uncorrected for phase shift. k-range is 3-13.5 Å-1

Table F4 Structural parameters derived from curve fitting to theoretical standards for Zn reference materials.

Zn reference materials	Filter (Å)	shell	CN	CN_{ref}	R (Å)	R_{ref}	ΔR	σ^2(Å)	ΔE_0(eV)	R-factor
ZnO	1.0-2.0	Zn-O	4*	4	1.965	1.81-1.98	0.011	0.006	4.584	0.025
	2.0-3.4	Zn-Zn	12*	11.7-12.4	3.208	3.21-3.23	0.028	0.010		
		Zn-O	12*	/	3.569	/	0.017	0.009		
		Zn-O/Zn	24*	/	3.569	/	0.025	0.020		
		Zn-O	9*	/	3.768	/	0.001	0.006		
	3.4-4.5 Å	Zn-O	36*	/	4.471	/	0.017	0.009		
		Zn-Zn	36*	/	4.471	/	0.033	0.015		
		Zn-Zn	6*	/	4.537	/	0.091	0.005		
		Zn-O	6*	/	4.575	/	-0.100	-0.001		
$2ZnCO_3 \cdot 3Zn(OH)_2$	1.0-2.0	Zn-O	4*	4	1.980	1.95	-0.069	0.007	-1.13	0.015
		Zn-O	6*	6	2.040	2.05-2.10	-0.069	0.007	-1.13	
	2.0-3.8	Zn-Zn	1.2	1.7-6.3	3.110	3.14-3.22	-0.066	0.007	-1.13	
		Zn-O	1.8	2.3-7.7	3.550	3.22-3.55	-0.053	0.007	-1.13	

Continued to previous page

α-$Zn_3(PO_4)_2$	1.0-2.0	Zn-O	4*	4.0	1.959	1.95-1.98	0.029	0.008	0.769	0.0022
	2.0-3.6	Zn-P	4*	1.1-4.0	3.058	3.03-3.10	-0.015	0.019		
		Zn-O	2*	/	2.943	/	-0.151	0.005		
		Zn-Zn	2*	0.9-3.0	3.251	3.3-3.4	-0.132	0.014		
		Zn-O	2*	/	3.687	/	0.183	0.012		
		Zn-O	6*	/	3.677	/	-0.103	0.051		
ZnS	1.0-3.0	Zn-S	4*	4.0-4.3	2.340	2.33-2.35	-0.0019	0.0058	3.804	0.0087
	3.0-4.8	Zn-Zn	12*	/	3.840	/	0.015	0.015	3.804	
		Zn- S /Zn	24*	/	4.260	/	0.005	0.014	3.804	
		Zn-S	12*	/	4.252	/	-0.003	0.009	3.804	
		Zn-S	12*	7.91	4.456	4.46	-0.029	0.016	3.804	

Continued to previous page

$ZnFe_2O_4$	1.0-2.0	Zn-O	4*	3.7-4.0	1.808	1.98-1.99	0.147	0.004	-0.085	0.039
	2.0-4.0	Zn-O	12*	/	3.610	/	0.149	0.007	9.973	
		Zn-Fe	12*	12-17.3	3.547	3.5	0.085	0.007	7.688	
		Zn-Zn	4*	4.0-5.9	3.705	3.7-3.8	0.089	0.007	7.688	
		Zn-O	48*	/	4.287	/	0.176	-0.005	9.973	
		Zn-O	24*	/	3.978	/	0.299	0.007	-0.085	

Amplitude reduction factor SO^2 is set as 0.93 by fitting ZnO standard;
* fixed value;
The fixed ratio for ZnO_4 and ZnO_6 in $2ZnCO_3{\cdot}3Zn(OH)_2$ is 2:3.
/ unknown;
The reference for CN_{ref} and R_{ref} are summarised in Table A10, Appendix A.